Dark Matter Detection Phenomenology

by

Ahmet Coşkuner

A dissertation submitted in partial satisfaction of the

requirements for the degree of

Doctor of Philosophy

in

Physics

in the

Graduate Division

of the

University of California, Berkeley

Committee in charge:

Professor Kathryn M. Zurek, Co-chair
Professor Lawrence J. Hall, Co-chair
Professor Karl Van Bibber
Professor Yasunori Nomura

Summer 2021

Dark Matter Detection Phenomenology

Abstract

Dark Matter Detection Phenomenology

by

Ahmet Coşkuner

Doctor of Philosophy in Physics

University of California, Berkeley

Professor Kathryn M. Zurek, Co-chair

Professor Lawrence J. Hall, Co-chair

In the last century, cosmological and astrophysical observations indicated that $\sim 85\%$ of the matter in the universe is inert, non-baryonic and non-luminous dark matter. The existence of particle dark matter is well motivated, however, all that is known about its nature is indirect information coming from large-scale astrophysical/cosmological observations or laboratory bounds. The nature of this elusive yet abundant dark matter naturally became one of the greatest conundrums in modern science. A tremendous effort was spent on exploring the theory space and building detection experiments. Still, the dark matter remained elusive. This elusiveness emphasized the importance of a more comprehensive approach to the dark matter hunt: The standard minimalist scenarios may not be sufficient; wider mass ranges and richer "dark sectors" may need to be considered. The dark sector theories' potential to address the dark matter problem along with other problems in the Standard Model, and the independent motivation for them coming from various top-down models, caused them to get significant traction. In addition to exploring a broad range of theoretical possibilities, another important aspect of dark matter detection is background reduction. Since the dark matter particles are competing with the Standard Model particles for interacting with the experiments, the methods distinguishing the dark matter events are crucial to improve the signal-to-noise ratio. In this dissertation, we have embraced a comprehensive approach to dark matter detection by considering a wide range of dark matter candidates (with large freedom in mass, and considering nonminimal dark sectors), interactions (including nuclear recoils, collective excitations, electron excitations), and targets (including superfluids, superconductors, Dirac materials, polar crystals.) In addition to overall reach constraints, we also focused on the anisotropies and the daily modulation prospects to explore the potential to distinguish dark matter signals from the background noise effectively.

Contents

Contents **i**

1 Introduction **1**

2 Fundamentals of the Hunt for Dark Matter **4**
2.1 Dark Matter: Statement of the Problem, and the Evidence 4
2.2 Thermally Produced Dark Matter: The WIMP Example 14
2.3 Direct Detection of Dark Matter 18
2.4 A Glimpse Into the Hidden Sector: Asymmetric Dark Matter Nuggets 32

3 Direct Detection of Bound States of Asymmetric Dark Matter **40**
3.1 Introduction 40
3.2 Composite Asymmetric Dark Matter 42
3.3 Nucleon couplings 51
3.4 Electron couplings 62
3.5 Conclusions 72

4 Directional Dark Matter Detection in Anisotropic Dirac Materials **74**
4.1 Introduction 74
4.2 Dark Matter Interactions with In-Medium Effects 76
4.3 Preliminaries: Dark Matter Wind 78
4.4 Absorption in Anisotropic Dirac Materials 80
4.5 Scattering in Anisotropic Dirac Materials 82
4.6 Conclusions 88

5 Directional Detectability of Dark Matter With Single Phonon Excitations: Target Comparison **89**
5.1 Introduction 89
5.2 Directional Detection With Single Phonon Excitations 91
5.3 Target Comparison 100
5.4 Conclusions 104

A Asymmetric Dark Matter Nuggets: Material Overburden **105**

B Zero Temperature Limit for Superconductors **107**

C In Medium Polarization Tensor **108**

D Dielectric Tensor **109**
D.1 Comparison with previous results 110

E Daily Modulation Amplitudes for Additional Materials **112**
E.1 Calculation of the Modulation Reach 112

Bibliography **115**

Acknowledgments

I occasionally receive emails from prospective graduate students, asking about my experience with the University of California (UC), Berkeley and my advisor. Let me summarize my answer here: UC Berkeley is one of the best places on the planet to study particle physics, and Kathryn Zurek is one of the best people on the planet to study particle physics with. Over the years, I witnessed firsthand how she helps everyone around her to achieve their potential. I thank Kathryn for the great impact she has had and is still having on my physics journey. I am incredibly grateful.

I thank the members of my dissertation committee: Karl Van Bibber, Lawrence J. Hall, and Yasunori Nomura; as well as Daniel McKinsey who served on my qualifying exam committee. In addition to my dissertation work, I took courses from them, and attended their meetings/talks on and off campus. The physics (and, at times, philosophy) I learned from them was exciting. However, what impressed me the most was how humble and approachable these leading figures in their respective fields were. That is a lesson I will carry with me for the rest of my life.

I enjoyed working with and learned so much from my collaborators: Dorota M. Grabowska, Simon Knapen, Andrea Mitridate, Andres Olivares, Tanner Trickle, and Zhengkang Zhang. I have yet to discover how it feels to collaborate with someone I do not like because it never happened. I thank them for being great people while also doing great physics. Many of my collaborators have also been inspiring role models.

The Berkeley Center for Theoretical Physics (CTP) has provided an invaluable academic environment, and the list of people there I would like to thank is longer than I can state here.

One obvious prerequisite for graduate studies is admission, which strongly depends on undergraduate research experience. Özhan Özatay, Aisha Özbay and Erkcan Özcan created a small research heaven for their undergraduates, despite all the financial, cultural, and geographical challenges. The great graduate school experience I described above would not have been possible without the research opportunities and mentorship they provided at Bogazici University. I am immensely thankful.

Can Kılıç has been generously sharing advice with me ever since a year before I started my graduate studies. As a prominent particle physicist coming from a background similar to mine, he provided personalized information that I could not have gotten anywhere else. I thank him for guiding me at the most critical points in my physics journey.

I thank the Institute of International Education, the Fulbright Program, and the Berkeley CTP (both the campus and Lawrence Berkeley National Laboratory branches) for their generous financial support in the form of various fellowships and assistantships.

My mother, Ayşe, has made great sacrifices so that my siblings and I could get a proper education and pursue our dreams. It is a privilege to have her as my mother—a privilege for which I will always be grateful.

Finally, I thank my wife, Çiğdem, for her endless love and support. I could not have asked for a better partner to share this journey with.

Chapter 1

Introduction

Discoveries in Cosmology in the last century have shown that the vast majority of the energy content in the Universe is unfamiliar: Only the $\sim 5\%$ of energy is the "familiar" baryonic matter, whereas the remaining $\sim 95\%$ consists of dark energy and dark matter (DM) (which compose $\sim 70\%$ and $\sim 25\%$ of the Universe's energy, respectively). Dark energy is an unknown type of energy that affects the Universe at the largest scales and is responsible for its accelerated expansion [1], and DM is a non-baryonic, non-luminous type of matter (hence the name "dark"), which has become an integral part of the ΛCDM (Lambda cold dark matter) cosmology [2, 3].

The success of the ΛCDM cosmology has established the existence of DM with a high degree of confidence, and astrophysical observations provided further evidence for it. Even though the Universe at large scales gives us hints about the features of DM, our knowledge about its particle physics properties is limited (since the DM has never been observed to interact with other particles through an interaction other than gravity). In that sense, our understanding of what DM is (and what it is not) is based almost solely on our "macro" observations on large-scale properties of the Universe and astronomical objects.

Unsurprisingly, understanding the nature of this mysterious DM has become one of the main goals in physics. This new type of matter has to be compatible with our current understanding of particle physics and conserve the successes of ΛCDM cosmology. Accordingly, the possibilities being explored in the hunt for DM are expansions to our Standard Model (SM) of particle physics, and ΛCDM cosmology.

The DM challenge is unique. Historically, there have been other challenging particle hunts too. After estimating the neutrino cross section to be less than 10^{-44}cm^2, Bethe and Peierls famously predicted that "It is therefore absolutely impossible to observe processes of this kind with the neutrinos created in nuclear transformations." [4] Still, the ingenuity of experimentalists proved the existence of these ultra-weakly interacting particles less than two decades later. What makes this challenge different than the DM challenge is, even though the cross section was small, the nature of the interaction was not unknown. There have been well motivated predictions for the way neutrinos interact with other particles, and those predictions guided the experimental discovery efforts. However, for the case of DM,

how it interacts with the SM particles is not known. It is fair to say that we are looking for a particle that we do not know about (All we know is indirect information coming from cosmological/astrophysical observations and laboratory bounds.) This makes the theory space wide: There are minimal DM models and more complicated dark sectors, bottom-up and top-down approaches, huge freedom in the allowed mass range, and interaction cross sections.

This freedom in theory space and the elusiveness of the DM so far provides motivation for a comprehensive approach to the hunt for DM: A broad range of possibilities for the nature of DM are worthy of consideration.

- DM mass can range from ultra-light to ultra-heavy, with a freedom around 90 orders of magnitude.
- DM can have a nonminimal dark sector with its "hidden" dynamics. It can be interacting with the SM particles through various mediators/portals.
- DM can be interacting with the SM particles by depositing lower energies than the thresholds of the current experiments.

Even if we optimistically assume that we make accurate predictions about the nature of DM and its interactions, the challenge is not over. Other particles compete with DM interactions in the experiments, causing background noise. Therefore another crucial aspect of DM detection is improving the signal-to-noise ratio [5].

In this thesis we aimed to embrace a comprehensive approach and considered a diverse range of possibilities for the nature of DM. In addition, we focused on the anisotropic materials and the daily modulation of the scattering rate to distinguish the DM events from the background events more effectively. To summarize:

- Ch. 2 introduces the fundamentals of the hunt for DM. It is an introductory chapter explaining the basics and the motivation for the chapters to follow.
- Ch. 3 (Ref. [6]) considers a hidden sector scenario: Asymmetric Dark Matter (ADM). There we discuss how ultra-heavy composite ADM nuggets can form and how they may interact with the SM particles by considering nuclear recoils, collective excitations and electronic excitations. We compare low threshold low exposure experiments to higher threshold higher exposure experiments to observe the effect of coherent enhancement. We also discuss indirect constraints on composite Asymmetric Dark Matter.
- Ch. 4 (Ref. [7]) analyzes the small $\mathcal{O}$(meV) band gap Dirac Materials for dark-photon mediated scattering and absorption of light DM events. The daily modulation prospects of the anisotropic Dirac materials were studied and the factors affecting the daily modulation amplitude were discussed.

- Ch. 5 (Ref. [8]) evaluates 26 materials for single phonon excitation events. There we study the reaches and the daily modulation amplitudes of a wide variety of targets and discuss the factors affecting the modulation amplitudes.

A more detailed explanation of chapters 3, 4, and 5 can be found below:

Chapter 3: We study the reach of direct detection experiments for large bound states (containing 10^4 or more dark nucleons) of Asymmetric Dark Matter. We consider ordinary nuclear recoils, excitation of collective modes (phonons), and electronic excitations, paying careful attention to the impact of the energy threshold of the experiment. Large exposure experiments with keV energy thresholds provide the best (future) limits when the Dark Matter is small enough to be treated as a point particle, but rapidly lose sensitivity for more extended dark bound states, or when the mediator is light. In those cases, low threshold, low exposure experiments (such as with a superfluid helium, polar material or superconducting target) are often more sensitive due to coherent enhancement over the dark nucleons. We also discuss indirect constraints on composite Asymmetric Dark Matter arising from self-interaction, formation history and the properties of the composite states themselves.

Chapter 4: Dirac materials, because of their small $O(\text{meV})$ band gap, are a promising target for dark photon-mediated scattering and absorption of light dark matter. In this chapter, we characterize the daily modulation rate of dark matter interacting with a Dirac material due to anisotropies in their crystal structure. We show that daily modulation is an $O(1)$ fraction of the total rate for dark matter scattering in the Dirac material $ZrTe_5$. When present, the modulation is dominated by the orientation of the material's dielectric tensor with respect to the dark matter wind, and is maximized when the crystal is oriented such that the dark matter wind is completely aligned with the largest and smallest components of the dielectric tensor at two different times of the day. Because of the large modulation, any putative dark matter scattering signal could be rapidly verified or ruled out by changing the orientation of the crystal with respect to the wind and observing how the daily modulation pattern changes.

Chapter 5: Single phonon excitations are sensitive probes of light dark matter in the keV-GeV mass window. For anisotropic target materials, the signal depends on the direction of the incoming dark matter wind and exhibits a daily modulation. We discuss in detail the various sources of anisotropy, and carry out a comparative study of 26 crystal targets, focused on sub-MeV dark matter benchmarks. We compute the modulation reach for the most promising targets, corresponding to the cross section where the daily modulation can be observed for a given exposure, which allows us to combine the strength of DM-phonon couplings and the amplitude of daily modulation. We highlight Al_2O_3 (sapphire), $CaWO_4$ and h-BN (hexagonal boron nitride) as the best polar materials for recovering a daily modulation signal, which feature $\mathcal{O}(1-100)\%$ variations of detection rates throughout the day, depending on the dark matter mass and interaction. The directional nature of single phonon excitations offers a useful handle to mitigate backgrounds, which is crucial for fully realizing the discovery potential of near future experiments.

Chapter 2

Fundamentals of the Hunt for Dark Matter

The evidence for DM also gives us information about its properties. Accordingyly, investigating the evidence for its existence also means collecting clues about its nature. In the next section (Sec. 2.1) we discuss the evidence for (and therefore the known properties of) DM.

In Sec. 2.2 we explore the thermal freeze-out scenario and the weakly interacting massive particle (WIMP) miracle.

Sec. 2.3 lays out the framework for the direct detection of dark matter. The detailed discussion of the kinematics including the daily and annual modulations of the rate help to interpret the work done on background suppression in the chapters to follow.

In Sec. 2.4 we consider a nonminimal dark sector by focusing on asymmetrically produced dark matter. We discuss how composite states can form, and how the coherent enhancement can provide a massive advantage for the low threshold experiments.

2.1 Dark Matter: Statement of the Problem, and the Evidence

Evidence for Dark Matter

Since the only way the DM was observed to interact with the "ordinary" matter is through gravity, the observations that indicate its existence are all large-scale cosmological or astrophysical observations. In this section we will investigate the observations that serve as evidence for DM in rough chronological order, and then discuss the crude properties of DM that we infer from this observational evidence.

Zwicky and the Galaxy Cluster Masses

In papers published in the 1930s, Zwicky has calculated the mass of the Coma galaxy cluster using the virial theorem [9] (utilizing the redshift data by Hubble and Humason [10]). Hubble and Humason noticed that eight galaxies in the Coma cluster were observed to have a peculiar velocity distribution with large scatters compared to other clusters observed. This peculiarity attracted the interest of many, and Zwicky was the first to get a mass estimate of the galaxy cluster via the virial theorem. After this analysis, he famously announced (in his original 1933 paper in German) "If this would be confirmed, we would get the surprising result that dark matter is present in much greater amount than luminous matter." which became a popular quote in virtually any dark matter related presentation. Although he was cautious with the statement, he came up with both the first evidence and the name for this new type of matter: dark matter.

Zwicky started with the fundamental law of the motion of nebulae (σ), which was fundamentally a $\vec{F} = m\vec{a}$ equation recast for the nebulae:

$$M_\sigma \frac{d^2\vec{r}_\sigma}{dt^2} = \vec{F}_\sigma \ , \tag{2.1}$$

with M and $\vec{r}$ denoting the mass and position of the nebula respectively, and $\vec{F}$ stands for the total force acting on it. Multiplying both sides by $\vec{r}$ and summing over the nebulae (σ index) yields:

$$\frac{1}{2}\frac{d^2\Phi}{dt^2} = \mathrm{Vir} + 2K_T \ , \tag{2.2}$$

where $\Phi = \sum_\sigma M_\sigma r_\sigma^2$ is the polar moment of inertia, $\mathrm{Vir} = \sum_\sigma \vec{r}_\sigma \cdot \vec{F}_\sigma$ is the virial, and K_T is the total translational kinetic energy of the nebulae in the galaxy cluster. Zwicky assumes the cluster is stationary and therefore the polar moment of inertia oscillates around a constant value in time. This makes the time average of the change in Φ zero. Thus, denoting the time averages with a bar, one gets:

$$\overline{\mathrm{Vir}} = -2\overline{K}_T \ . \tag{2.3}$$

Then, assuming the gravitational interactions among the nebulae are accurately described by Newton's law of gravity, one also gets $\mathrm{Vir} = U$ where U is the total gravitational potential energy of the cluster due to its constituent nebulae. Combining these equations gives rise to the equation that is known as the virial theorem:

$$-\bar{U} = -2\bar{K}_T = \sum_\sigma M_\sigma \overline{v_\sigma^2} \ , \tag{2.4}$$

where again, the σ indices denote individual nebulae, and v_σ is the speed of a single nebula. Zwicky assumes a spherical distribution of nebulae in the cluster and uses the corresponding polar moment of inertia:

$$U = -G\frac{3M_{\mathrm{cluster}}}{5R_{\mathrm{cluster}}} \ , \tag{2.5}$$

with G being the familiar Newton's gravitational constant. Using double bars to denote averaging over both time and the masses, $\sum_\sigma M_\sigma \overline{v_\sigma^2}$ can be recast as:

$$\sum_\sigma M_\sigma \overline{v_\sigma^2} = M_{\text{cluster}} \overline{\overline{v^2}} \ . \tag{2.6}$$

This gives a way of writing down the cluster mass:

$$M_{\text{cluster}} = \frac{5 R_{\text{cluster}} \overline{\overline{v^2}}}{3G} \ . \tag{2.7}$$

In his original paper, Zwicky discusses that the uniform mass distribution assumption is not valid for the Coma cluster, and following an example nonuniform mass distribution he comes with a more conservative estimate of the cluster mass:

$$M_{\text{cluster}} > \frac{R_{\text{cluster}} \overline{\overline{v^2}}}{5G} \ . \tag{2.8}$$

Then, having this framework built, Zwicky analyzed the Coma cluster (assuming 1000 galaxies, a radius of 2×10^6 light years, and using the observed 700 km/s velocity dispersion), and he arrived at an unexpectedly high mass to light ratio (γ) of around 500 [9]. He compared this result to the mass to light ratio obtained from the local Kapteyn stellar system ($\gamma' = 3$), and stated that the discrepancy is so great that a further evaluation of the problem is in order. In the same paper, Zwicky made statements describing his thoughts about what this "dark matter" is: "we must know how much dark matter is incorporated in nebulae in the form of cool and cold stars, macroscopic and microscopic solid bodies, and gases." Zwicky realized that this mysterious form of matter was non-luminous. As we have discussed in the preceding chapters, this observational evidence also gave us clues about the properties of DM. In the following years, methods similar to Zwicky's established the existence of dark matter with much higher confidence. Still, Zwicky's prediction is infamous for being the very first prediction of DM.

Rubin and The Galactic Rotation Curves

One way to measure the speed of the gas rotating around galaxy centers is to measure the redshift (or Doppler shift) of the light coming from the baryons (For example, redshifts in the 21 cm hyperfine transition observation of hydrogen atoms [11]). Assuming certain symmetrical structures for the galaxies, significant information about the expected velocities for the rotating gasses can be inferred. Assuming the mass distribution in galaxies is cylindrically symmetric (which is a reasonable assumption considering the disk shaped galaxies), one can write down the expected circular speed of rotating gas particles (for example, stars) at a distance r from the center, by using Newtonian gravity:

$$v_\theta(r) = \sqrt{\frac{G M_{\text{enclosed}}(r)}{r}} \ , \tag{2.9}$$

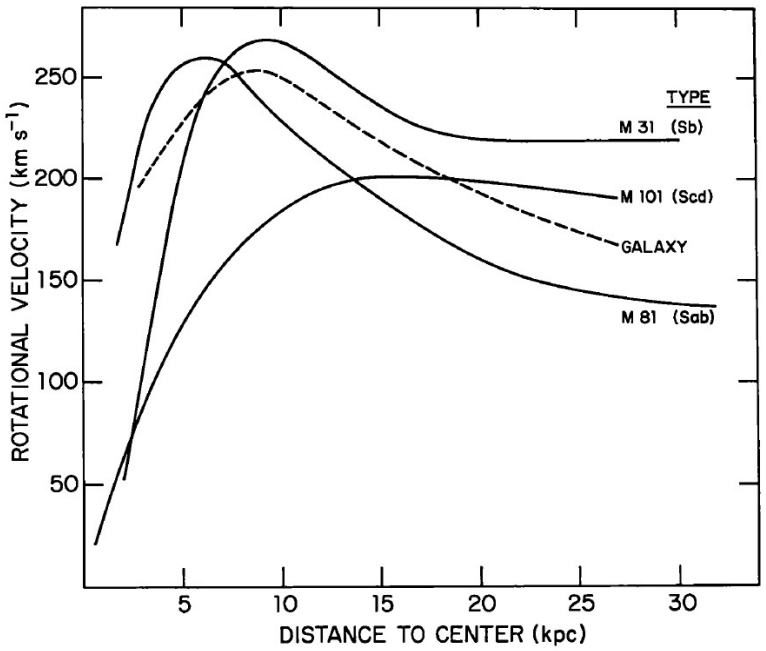

Figure 2.1: Rotation curves of 3 galaxies (M31, M101, and M81) in addition to the Milky Way. The curves flatten in large radii. [12]

where $M_{\text{enclosed}}(r)$ is the mass enclosed in a cylindrically symmetric Gaussian shape with radius r, and v_θ denotes the circular (tangential) speed. The radial dependence of the speed above will depend on the mass distribution inside the galaxy. However, outside the galaxy where the enclosed mass is simply the total mass of the galaxy, the radial dependence simplifies:

$$v_\theta(r) = \sqrt{\frac{GM_{\text{total}}}{r}} \text{ outside the galaxy.} \tag{2.10}$$

This behavior of $v_\theta(r) \propto r^{-1/2}$ is called Keplerian fall-off, which indicates the expected behavior of circular speed outside the galaxy. However, in the '70s and '80s, multiple papers have strongly established that the rotation curves were linear in lower radius values and flattened at higher r values, rather than the expected $r^{-1/2}$ fall-off [11–14] (an example figure demonstrating this behavior can be seen in Fig. 2.1). Assuming spherical halo shapes for the galaxies, flat rotation curves implied a linear increase of total mass with radius.

The easiest way to explain this is the presence of matter outside the luminous part of the galaxy [1]. For example, assuming uniform mass distribution in a sphere ($M_r \propto r^3$), the

[1]It is worth noting that another way of explaining this behavior is to think that the standard Newtonian gravity picture works differently at large scales. There are models (called modified Newtonian dynamics or MOND models) exploring this possibility, however they are not as successful as the cold particle DM picture in explaining other evidence we will discuss in the following sections.

circular speed would be:

$$v_\theta(r) \propto \sqrt{\frac{M_{\text{total}}}{r}} \propto r \ . \tag{2.11}$$

This explains the linear dependence of the circular speed on radius in lower radii values. The fact that the curve flattens in the high radii values indicates that, at those higher distances from the center, the enclosed mass still increases as the radius increases, implying the presence of the non-luminous "dark" matter. Even though the calculational details of the picture change depending on the actual mass distribution of individual galaxies, these rough properties derived (like expected Keplerian fall-off where there is no mass and linear curves at small radii, etc.) hold for other cylindrically symmetrical distributions as well.

The advent of radio telescopes and further observations to this day have only confirmed these nontrivial findings further [15, 16]: the rotation curves either flattened or declined at a much slower rate than the naively expected Keplerian fall-off behavior of $v_\theta(r) \propto r^{-1/2}$, providing strong evidence for nonluminous DM.

Cosmic X-ray Observations

The baryonic matter under a strong gravitational potential emits Bremsstrahlung radiation, whereas the baryonic matter in environments with weak gravitational potential present emits much fewer photons. Measuring the x-ray profile of a baryonic gas (which includes its thermal Bremsstrahlung profile) provides a way of measuring the gravitational potential affecting the gas, therefore the mass profile of the galaxy. By assuming spherically symmetric galaxies, and with help from statistical mechanics, the mass content of a galaxy can be estimated as follows.

Assuming spherical symmetry, the Euler's equation of fluid dynamics can be recast as:

$$\rho \frac{d\vec{v}}{dt} = -\nabla p - \rho \nabla \Phi \ , \tag{2.12}$$

where ρ and p denote the density and the pressure respectively. In equilibrium where $\vec{v} = 0$, Eq. 2.12 implies

$$\frac{dp}{dr} = -\frac{G_N M(r) \rho}{r^2}, \tag{2.13}$$

where G_N is the gravitational constant, and $M(r)$ is the mass enclosed in the radius r. To write the pressure p as a function of temperature T, we can utilize the ideal gas law by assuming a gas consisting of nucleons:

$$p = \frac{\rho k_B T}{m_N}, \tag{2.14}$$

where m_N is the mass of a nucleon. Substituting the expression for p in Eq. 2.14 into Eq. 2.13, the mass enclosed $M(r)$ can be written as:

$$M(r) = \frac{k_B T r}{G_N m_p} \left(-\frac{d\ln\rho}{d\ln r} - \frac{d\ln T}{d\ln r} \right), \tag{2.15}$$

Figure 2.2: Baryonic mass density in the Bullet Cluster (obtained through X-ray observations, shown in pink) and "dark" mass density in the Bullet Cluster (obtained through gravitational lensing, shown in blue) overlayed. The image was created by combining the work of Refs. [19, 20].

which relates the total mass profile to the temperature and the gas density profile. This relation can be used to probe the mass content of a galaxy by using its temperature data.

When the temperatures are measured using x-ray profiling, the discrepancy between the observed temperatures and the temperatures expected from the gravitational effects of baryonic matter implies the presence of nonbaryonic matter in galaxies [17]. This alone serves as proof that DM exists, however the evidence becomes stronger when combined with weak gravitational lensing, which is discussed in the next subsection.

Weak Gravitational Lensing

According to the theory of general relativity, the path of light is affected by gravitation, and thus the massive objects bend the trajectories of photons. This distortion in the observed images due to photons tracking curved geodesics can be used to probe the presence of gravitational force, and hence the mass in a region. Applying this method in large scales, for example to the galaxy clusters, provides another way of probing the mass present in those galaxy clusters [18].

Overlaying the mass profile of luminous baryonic matter obtained through x-ray observations and the "dark" mass profile obtained through the gravitational lensing yields an

interesting observation that can be seen in Fig 2.2. After the collision of these two huge galaxy clusters, the baryonic gas clouds collided and their shapes were distorted. However the "dark" clouds did not interact (or interacted very weakly) by means of any interaction other than gravity. This observation of colliding baryonic gas and collisionless DM gas serves as one of the most compelling pieces of evidence for the existence of DM, partly because this phenomenon is hard to explain with competing modified gravity models and more directly indicates a particle DM compared to the other evidence we have discussed so far.

Cosmic Microwave Background and Matter Power Spectra

Details of the predictions of Cosmic Microwave Background (CMB) and matter power spectra are beyond the scope of this brief review, still, we will qualitatively discuss how the presence of cold DM fits greatly to our understanding of cosmology and cosmic evolution. As discussed in Ch.7 of Ref. [3] and Ch.9 of Ref. [2], the anisotropies in both the CMB and power spectra sensitively depend on the presence of DM in the Universe.

As shown in Fig. 2.3, both the CMB and power spectra strongly confirm the ΛCDM cosmology which relies on the presence of dark matter. These figures can be qualitatively interpreted as follows: Both CMB and power spectra are measures of anisotropies in structure in the Universe. The lack of DM is expected to give rise to a much more isotropic or "smooth" universe, and the anisotropies observed in cosmic structures are hard to explain without proposing the existence of the DM. The existence of DM provides "gravitational potential wells" that help the matter collapse together, helping the formation of the anisotropic structures observed. This, which is quantitatively shown in Refs. [2, 3] provides yet another powerful evidence for DM. Just like the weak gravitational lensing and the Bullet Cluster discussion, this anisotropic structure formation (derived from CMB and power spectra) is also another piece of DM evidence that is hard to explain with MOND theories, strengthening the case for the particle DM.

General Properties of Dark Matter

So far we have discussed the evidence for DM, and all the observations considered were related to large scales. Thus almost all of our understanding of what DM is comes from the macroscopic/cumulative observations of it. Since no DM particle has been observed in a laboratory, we have no direct clues about its particle physics properties. Still, the macroscopic observations provide rough information on the particle properties the DM has to have. These are the requirements a DM hunter has to fulfill when considering the possibilities about what DM could be.

To start with, as the name implies, DM has to be dark. In other words, it should not interact electromagnetically, or emit photons. This virtual lack of electromagnetic interaction of DM can be used to put constraints on how much charge it can have [23]. Not being able to emit photons implies DM cannot cool efficiently by means of photon emission, therefore it is dissipationless. Without this efficient electromagnetic cooling mechanism available, it is

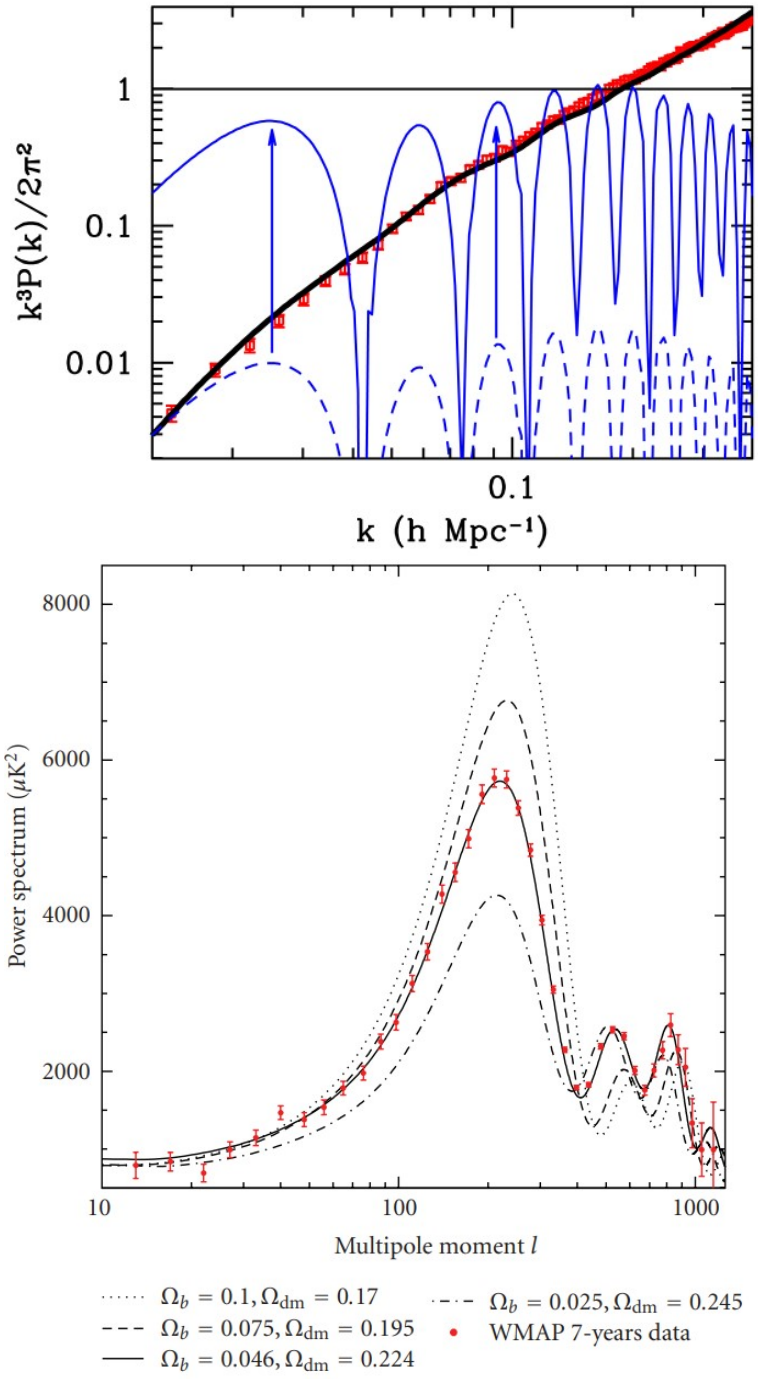

Figure 2.3: **Top:** An analysis of the matter power spectra, comparing the DM picture (black line) and a no DM picture (dashed blue line) to the observations (shown in red) [21] (The solid blue lines are predictions of a MOND theory.). **Bottom:** An analysis of the CMB spectra, comparing various scenarios of abundances of DM to the observations (shown in red) using WMAP 7-years data. [22].

harder for DM to lose its energy, collapse on itself and form structures. This explains why DM is more evenly spread in space compared to baryonic matter.

Following the discussion on Bullet Cluster in Sec. 2.1, DM gasses apparently do not interact (or interact very weakly) with interactions other than gravity. The fact that DM clouds in the Bullet Cluster passed through each other with virtually no distortion to their shapes translates to limits on how much DM particles can interact with each other or with baryonic matter.

DM also needs to be fluid, in the sense that, it cannot consist of a small number of ultra-heavy objects. The possible extremely heavy dark matter particles would distort the other stellar objects, for example, stellar clusters [24]. The observed behavior of visible stellar objects puts constraints on how large or "granulated" the DM can be. Gravitational lensing observations also put constraints on the granularity of DM, since the DM masses that are too massive would have corresponding weak gravitational lensing signatures.

Another property of DM is, it is classical in the sense that it is localized in galaxies. The fact that DM can be confined to smaller galaxies like dwarf galaxies indicates that its quantum properties (de Broglie wavelength, to be specific) allow it to be confined to these scales. This also translates to limits on how large the de Broglie wavelength of a DM particle can be.

Since only the crude properties like the ones discussed can be inferred about the DM, the range of possibilities is wide. A large number of different theoretical candidates were explored: Some were minimal extensions to the standard particle and cosmology pictures, and some others were nonminimal models with more complex internal dynamics (Nonminimal "dark sectors" which are well motivated by various top-down approaches like string theory and supersymmetry, and aim to solve various problems of SM in addition to the DM problem, are discussed in more detail in Ch. 2.4.) An overview of the popular DM candidates is shown in Fig 2.4.

Distribution of Dark Matter in the Universe: Density and Velocity Profiles

The flattening rotation curves we have discussed indicate a DM density profile that has a radial dependence of $\rho(r) \propto 1/r^2$. Having this piece of information, and considering the rough properties of DM discussed, we can use classical mechanics to try to infer the velocity distribution of the DM gas.

The evolution of the phase space density $f(\vec{r}, \vec{v})$ of a gas is described by the Boltzmann equation:

$$\vec{L}(f) = \vec{C}(f) \ , \tag{2.16}$$

where $\vec{L}(f)$ is the Liouville operator and $\vec{C}(f)$ is the collision operator. In the non-relativistic limit, the Liouville operator can be written as:

$$\vec{L}(f) = \frac{\partial f}{\partial t} + \dot{\vec{r}}\frac{\partial f}{\partial \vec{r}} + \dot{\vec{v}}\frac{\partial f}{\partial \vec{v}} \ . \tag{2.17}$$

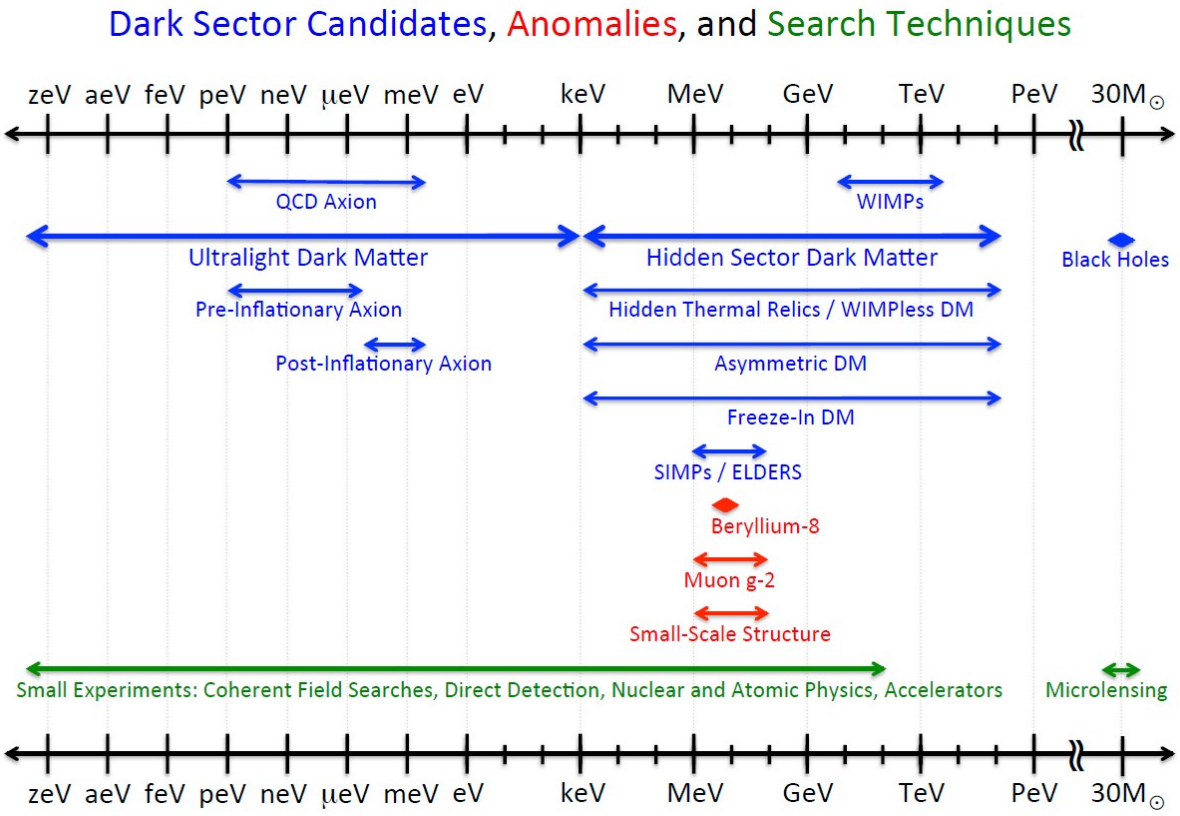

Figure 2.4: A summary of popular DM candidates and the search techniques, from Ref. [25].

Putting the possibility of the DM interactions in parentheses and assuming the gas is collisionless, we will have $\vec{L}(f) = 0$. According to Jeans theorem, solution to this requirement in steady state ($\frac{\partial f}{\partial t} = 0$) can only be an $(\vec{r}, \vec{v})$ pair that satisfies

$$\frac{d}{dt} I(\vec{r}(t), \vec{r}(t)) = 0 \tag{2.18}$$

for integrals of motion $I(\vec{r}(t), \vec{r}(t))$. Accordingly, for a spherically symmetric, steady state halo, Jeans theorem yields that the $f(\vec{r}, \vec{v})$ can only depend on the energy. For convenience, we define the energy per unit mass $\varepsilon = \Psi - \frac{1}{2}v^2$ where Ψ is the gravitational potential. Aiming to get a $\rho(t) \propto r^{-2}$, we conveniently choose a phase space density distribution $f(\vec{r}, \vec{v}) = f(\varepsilon) \propto e^{\varepsilon}$. This yields (with the velocity dispersion σ):

$$\rho \propto \int_0^\infty dv\ v^2 f(v) = \int_0^\infty dv\ v^2 \exp\left(\frac{\Psi - v^2/2}{\sigma^2}\right) \propto e^{\Psi/\sigma^2}\ . \tag{2.19}$$

This combined with the Poisson's equation $\nabla^2\Psi = -4\pi G\rho$ gives

$$\rho(r) = \frac{\sigma^2}{2\pi G r^2} \ , \tag{2.20}$$

which is the $\rho(r) \propto r^{-2}$ density distribution we aimed for. As a result, we see that a velocity distribution

$$f(v) \propto e^{-v^2/\sigma^2} \tag{2.21}$$

gives us a mass density profile that is consistent with the flattening rotation curves, thus it is a good ansatz for the actual velocity distribution of DM. This observation comes with a slight caveat: This density profile, when integrated, would yield an infinite mass. This indicates that the assumption of flat rotation curves should no longer be valid in high radial distances (which are not in the reach of current observations).

In this calculation to get an analytic velocity distribution expression, we have made various assumptions (steady state and axially symmetric galaxies, etc.) that are not completely valid. So it is helpful to compare the behavior of this analytic expression to the results of more sophisticated simulations. One famous set of figures comparing the Maxwell-Boltzmann (MB) velocity distribution to results of various simulations is shown in Fig. 2.5.

2.2 Thermally Produced Dark Matter: The WIMP Example

Relic Density and the WIMP Miracle

WIMP stands for "weakly interacting massive particle" and has been a popular candidate for dark matter (due to reasons we will discuss in this section). Even though the lack of WIMP signals in recent detection experiments challenged the WIMP paradigm, it still provides an informative framework to study DM detection phenomenology and relevant particle production mechanisms. Accordingly, in this section, we will discuss some popular (proposed) DM production mechanisms, and the reasons the idea of WIMP got the field so excited that the term "WIMP miracle" was introduced.

We start with considering the production of DM with the freeze-out mechanism. We will consider a $2 \to 2$ event $\chi\chi \to XX$ where χ and X denote the DM and SM particles respectively. To review the essence of freeze-out mechanism, in the early universe when this reaction is in chemical equilibrium, the number of DM and corresponding SM particles are also in chemical equilibrium. Then, as the Universe expands and cools down, the possibility of particles finding each other to react gets lower and the reaction "freezes", leaving the DM with a constant co-moving density [2]. Beyond this point the DM density is diluted only by Hubble expansion. The time that this decoupling from the equilibrium happens is when the

[2]Exceptions like self interactions of DM are ignored in this deliberately simple picture.

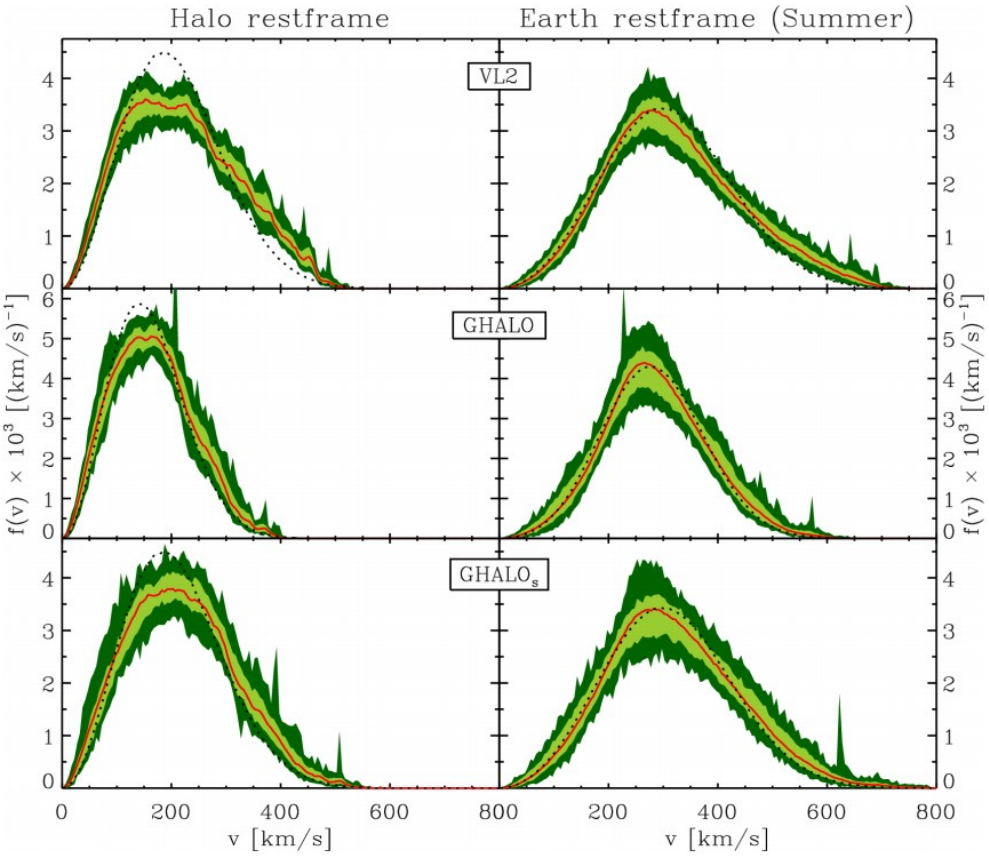

Figure 2.5: Comparison of the best fitting Maxwell-Boltzmann velocity distribution (dotted lines) with the results of Via Lactea and GHALO simulations (red lines). Light green regions indicate 68% scatter and dark green boundaries indicate maximum and minimum ranges [26]. As can be seen, MB velocity distribution is not a perfect fit to the simulation results, but is a reasonable analytic estimate.

reaction rate falls below the Hubble expansion rate, which corresponds to the condition:

$$\Gamma_{\text{chemical}} = n_\chi \langle \sigma v \rangle \sim H \ , \tag{2.22}$$

where Γ, n_χ, $\langle \sigma v \rangle$ and H stand for the reaction rate, DM number density, velocity-averaged cross section and Hubble rate. Even after this $\chi\chi \to XX$ reaction "freezes" and is decoupled from the chemical equilibrium, it can still be in a state of kinetic equilibrium through the corresponding elastic events $\chi X \to \chi X$. Similar to above, these elastic interactions also "freeze" or decouple when $\Gamma_{\text{thermal}} = n_X \langle \sigma v \rangle \sim H$, and the particles move freely without chemical or thermal interactions. From the cosmology textbooks, we learn the temperature dependence of particle number densities in relativistic and non-relativistic (hot and cold) regimes:

$$\begin{aligned} &n_\chi \propto T^{3/2} e^{-m_\chi/T} \text{ for cold and} \\ &n_\chi \propto T^3 \text{ for hot particle species.} \end{aligned} \tag{2.23}$$

Now, we proceed to investigate the freeze-out density of DM candidates. The equilibrium condition indicates:

$$\langle \sigma v \rangle_{12} (n_\chi^{eq})^2 = \langle \sigma v \rangle_{34} n_3^{\text{eq}} n_4^{\text{eq}} \ . \tag{2.24}$$

Here the numbers 1,2,3 and 4 denote the particles in the $\chi\chi \to XX$ event, and n_3 and n_4 are written independently to incorporate the possibility of different final particles. Then the corresponding Boltzmann equation can be written as

$$\dot{n} + 3Hn = \langle \sigma v \rangle_{12} \left(n_{\text{eq}}^2 - n^2 \right) \ . \tag{2.25}$$

Switching to the yield notation ($Y = n/s$ where s is the entropy density), and using the fact that sa^3 is a constant (a is the scale factor), the yield equation can be written as:

$$\frac{dY}{dt} = \langle \sigma v \rangle_{12} s \left(Y_{\text{eq}}^2 - Y^2 \right) \ . \tag{2.26}$$

Noting that $dx/dt = Hx$ (x is defined as m/T) , the equation can be written as a derivative in terms of x:

$$\frac{dY}{dx} = -\frac{xs\langle \sigma v \rangle_{12}}{H(m)} \left(Y^2 - Y_{\text{eq}}^2 \right) \ . \tag{2.27}$$

The equation above describes the yield of desired particle species as a function of temperature T, thus gives us an account of the particle density via the mechanism of freeze-out as the Universe evolves. It can be approximately solved analytically, or can be solved numerically. Evaluating certain limits allows deriving rough conclusions. When the rate of interaction is higher than the Hubble rate, the particles maintain equilibrium and the yield depends on the temperature of the Universe specifically at that point in time (to express this with equations, $Y\left(x \lesssim x_{\text{f.o.}}\right) \simeq Y_{\text{eq}}(x)$ since $\Gamma \gg H$. Here f.o. stands for freeze-out.) On the other hand, after the decoupling when the reaction rate is much smaller than the Hubble rate, the

yield is already frozen out and it corresponds to its value at the freeze-out temperature or the time (which means, $Y\,(x \gtrsim x_{\text{f.o.}}) \simeq Y_{\text{eq}}(x_{\text{f.o.}})$ since $\Gamma \ll H$.) The freeze-out event stalls the yield of DM in the Universe which would otherwise decrease exponentially. Using this information, and conveniently isolating the x dependence by using $\langle\sigma v\rangle = \langle\sigma v\rangle_0 x^{-n}$ and $s = s_0 x^{-3}$, Eq. 2.27 can be simplified to[3]:

$$\frac{dY}{dx} \simeq -\frac{\lambda}{x^{n+2}} Y^2, \text{ where } \quad \lambda = \frac{\langle\sigma v\rangle_0 s_0}{H(m)} \ . \tag{2.28}$$

Solving this differential equation yields

$$\frac{1}{Y_{\text{today}}} - \frac{1}{Y_{\text{f.o.}}} = \frac{\lambda}{(n+1)x_{\text{f.o.}}^{n+1}} \ . \tag{2.29}$$

Using the fact that typically $Y_{\text{f.o.}} \gg Y_{\text{today}}$:

$$Y_{\text{today}} \simeq \frac{n+1}{\lambda} x_{\text{f.o.}}^{n+1} \ . \tag{2.30}$$

For the sake of the argument, by picking $x_{\text{f.o.}} = 10$, we can estimate the DM abundance:

$$\left(\frac{\Omega_\chi}{0.2}\right) \simeq \frac{x_{\text{f.o}}}{10} \left(\frac{5 \times 10^{-9}\text{GeV}^{-2}}{\sigma}\right) \tag{2.31}$$

and therefore (depicting the interaction strength with $\langle\sigma v\rangle \sim \alpha^2/m^2$):

$$\Omega_\chi h^2 \sim \frac{3 \times 10^{-26}\ \text{cm}^3/\text{s}}{\langle\sigma v\rangle} \simeq \left(\frac{0.01}{\alpha}\right)^2 \left(\frac{m}{200\ \text{GeV}}\right)^2 \ . \tag{2.32}$$

If we substitute the weak-scale interaction strength $\alpha \sim 0.01$ and mass $m \sim 200$ GeV, we get the observed DM density. A 200 GeV DM particle interacting at the weak-scale almost magically giving the correct DM density pleasantly surprised the people and this phenomenon was called the "WIMP miracle". Weak-scale was a natural place to expect beyond-the-standard particle physics and cosmology (due to, for example, naturalness considerations) and the idea of WIMP attracted significant interest. In addition to the minimal extensions to standard pictures, the similar particles proposed by top-down approaches like supersymmetry added to the excitement, and WIMPs became the leading candidates in the hunt for DM. There has been and still is a significant effort to detect WIMPs (which will be discussed in more detail in the later sections), however, proposed WIMPs were elusive so far and no signal has been detected.

[3] $\langle\sigma v\rangle$ is typically a series in x, and here we assume one annihilation mode dominates.

Caveats to the WIMP Miracle

Even though the WIMP picture miraculously gives us the correct abundance with an interaction strength that is at the weak-scale, the requirement in Eq. 2.32 is not exclusive to WIMPs. The requirement can be satisfied by using a wide range of α and m values while keeping the α/m ratio the same (For examples of these alternative possibilities, you can see Ref. [27]).

The thermal production of DM via freeze-out mechanism and a simple, one-type DM particle were other assumptions we had made. There are multiple ways that the WIMP picture might change, even when these assumptions are still made.

One caveat is the possibility of having a resonance at temperatures near the freeze-out temperature $T_{\text{f.o.}}$. If $T_{\text{resonance}} \simeq T_{\text{f.o.}}$, the velocity averaged cross section used in the freeze-out calculation $\langle\sigma v\rangle_{\text{f.o.}}$ will be much higher than the $\langle\sigma v\rangle_{\text{today}}$. This discrepancy between the interaction strengths at the freeze-out time and today introduces a complication to the standard freeze-out picture.

Similarly, having a kinematic energy threshold for the production of the final SM particles also introduces a sharp change in the $\langle\sigma v\rangle$. Decreasing temperature, therefore decreasing collision energy would imply that if the Universe cools down enough to kinematically prohibit the pair production of the SM particles, the $\langle\sigma v\rangle$ would sharply decrease. This would also imply $\langle\sigma v\rangle_{\text{today}} < \langle\sigma v\rangle_{\text{f.o.}}$

There are more possible exceptions to the standard WIMP freeze-out picture than can be discussed here. Some notable examples are self interacting dark matter (SIDM) and the asymmetric dark matter (ADM). Self interacting dark matter could change the number density of the DM particles while keeping the entropy unaffected [28] and asymmetric dark matter (which is covered in Chapter 3) produces the observed DM abundance with an annihilation mechanism similar to the mechanism created the Baryon asymmetry [29]. More broadly, other possible exceptions are "hidden valley" or dark sector theories that introduce more sophisticated interaction mechanisms for the dark sector compared to the simpler picture studied in this chapter [30, 31].

2.3 Direct Detection of Dark Matter

Even though there could be theoretical reasons to expect the existence of a certain particle (like the case for the neutrinos in the first half of the 21st century), the way to actually confirm its existence and show that it is more than a useful theoretical tool is, its detection. This makes the detection of dark matter crucial.

The DM can interact with the SM particles elastically or inelastically. An inelastic interaction, for example:

$$\chi + X \to \chi' + X' \,, \tag{2.33}$$

(again, with χ's denoting DM particles and X's denoting SM particles) would imply at least two different types of DM particles. Even though the work has been done to explore this

possibility independent of the details of the nonminimal dark sector [32], the details of these inelastic scattering events highly depend on the DM model considered. And since our current understanding of the particle properties of DM and the details of the phenomenology of dark sector are also minimal, the theory space for inelastic scattering is wide. However, elastic scattering, which can be stated in the form:

$$\chi + X \to \chi + X \tag{2.34}$$

allows a minimal treatment with a single DM particle without requiring a richer dark sector phenomenology. This makes it possible to study elastic scattering events in a rather model-independent way, which we will do in this section. Since the scattering events are also interactions, the details of elastic scattering events will also depend on the DM models considered, though many of the conclusions we arrive at in this section will be applicable to all the elastic scattering events.

The reader probably already knows that DM detection is a challenge and the extraordinary effort to detect it through multiple ingenious experiments has not returned a positive outcome so far. The main reason that makes the detection of DM a challenge is: We do not know what dark matter is, and we have little information about its particle properties (which are coming from cosmology). For this reason, it is fair to say that we do not know what we are looking for. Given that the hypothesized particle's properties are almost completely unknown, and the way it interacts with SM particles, or if it interacts with SM particles at all (other than gravitational interaction) are a complete mystery, designing a detection experiment also becomes a harder challenge with endless possibilities. For the case of recent particle discoveries in the past century (for example, for the cases of Higgs particle and neutrinos), the detection was a challenge even though the way those particles interact with other SM particles were known/predicted. Experimentalists knew how the hypothesized particles were expected to interact with the more familiar SM particles, and designed the experiments accordingly, still it took decades to detect them. In the current state of little to no information regarding the properties of DM, this challenge is amplified.

Another reason that makes DM detection a challenge is, the kinematic restrictions on detection. In a scattering event, the maximum energy deposited is determined by the kinematics, and if that maximum energy deposited is below the threshold energy of the detection experiment the signal will not be noticed. Therefore ideally for DM detection, the kinematic space of the scattering events should be available for the detection, which can be achieved with lower experimental thresholds or larger DM masses (a large particle can deposit higher energy upon impact). Exploring the conservation of energy helps us see this more quantitatively. For elastic scattering described in Eq.2.34, we label the initial momentums of SM and DM particle p_{X1} and $p_{\chi 1}$ respectively.:

$$p_{X1} = (m_N, 0, 0, 0) \quad , \quad p_{\chi 1} = \left(m_\chi + \frac{1}{2} m_\chi v^2, m_\chi v, 0, 0\right) \ , \tag{2.35}$$

where m_N denotes the mass of the target nucleus. With q being the momentum transferred, we can write down the momentum conservation (after boosting to the center of mass frame

for convenience):

$$\begin{aligned} \vec{q} &= \vec{p}_{X2} - \vec{p}_{X1} \ , \\ \vec{p}_{X1} &= \mu_{\chi N}\vec{v}_{\chi} \ , \\ \vec{p}_{X2} &= \vec{q} + \mu_{\chi N}\vec{v}_{\chi} \ , \end{aligned} \tag{2.36}$$

where $\mu_{\chi N}$ is the reduced mass of the target nucleus and the DM particle. If we conveniently denote the scattering angle with θ, squaring $\vec{q}$ would give:

$$q^2 = 2p_{X1}^2 - 2\vec{p}_{X1}\cdot\vec{p}_{X2} = 2p_{X1}^2(1-\cos\theta) = 2\mu_{\chi N}^2 v_{\chi}^2(1-\cos\theta) \ . \tag{2.37}$$

Since the recoil energy E_R in the center of mass frame is given by $E_R = \frac{q^2}{2m_{\chi N}}$, it can be written as:

$$E_R = \frac{q^2}{2m_N} = \frac{\mu_{\chi N}^2}{m_N} v_{\chi}^2(1-\cos\theta). \tag{2.38}$$

Eq. 2.39 gives us a way to calculate the minimum DM mass m_{χ} we can probe for a given detector threshold energy ($E_{\rm th}$).

$$E_{R\rm min} = E_{\rm th} = \frac{q^2}{2m_N} = \frac{m_{\chi\rm min}^2}{m_N} v_{\chi}^2(1-\cos\theta). \tag{2.39}$$

In the expression above, since we are looking for the minimum DM mass, we made the simplification that $\mu_{\chi N} \approx m_{\chi\rm min}$. Considering the approximate $E_{\rm th}$ of the noble gas experiments as ≈ 1 keV, substituting the galactic escape velocity ($v_{\rm esc} \approx 600$ km/h) as an ansatz for the maximum velocity of the DM particle, and considering a Xenon target as an example (with $A = 131$), the minimum mass that can be detected $m_{\chi\rm min}$ is found to be around 10 GeV. This means that, if the event considered is a nuclear recoil, the lowest mass accessible to the currently running experiments is in the 1-10 GeV range.

The exercise above has shown that the mass range that can be detected by means of nuclear recoils is already limited. However, even if the DM particles are heavy enough and observable events happen, this still is not sufficient to announce the existence of dark matter due to competing background events. Sensitive DM detection experiments will detect background signals from other particles (like neutrinos.) As a result, having a sufficient DM signal-to-noise ratio is also crucial. We can write down the rate of scattering from a target material as:

$$R = K\frac{v\rho_{\chi}}{m_{\chi}}\sigma \ , \tag{2.40}$$

where $K \approx 6\times 10^{26}/A$ is the number of target nuclei (each with A nucleons) per kilogram, σ is the scattering cross section and ρ_{χ} is the DM density. Substituting the "WIMP-like" scattering cross section of $\sigma \sim 10^{-37}\text{cm}^2$, the DM density of $\rho_{\chi} \approx 0.3$ GeV/cm^3, the DM velocity of $v_{\chi} \approx 240$ km/s, and an atomic number of $A \approx 130$, we find that the expected rate of events (per kilogram per day) is around 0.01 - 0.1. This small event rate confirms the toughness of DM detection. The DM-SM scattering rate can be increased by increasing the target size, however this would increase the background noise as well. Background

suppression is important and an active area of research [33]. One way of suppressing the background is to make the DM-SM scattering events more distinctive, which can be achieved by utilizing the DM's unique properties. For example, the DM is thought to move in the galaxy in the form of a DM wind, and this wind's rotation around the center of the galaxy means that at a given time of the day or the year the DM wind will be approaching the experiment from a different direction. This periodic change in the direction of incoming DM wind can be used to isolate the DM-SM scattering events. Two of the periodic motions that can be utilized for this purpose are:

- Earth's motion around the Sun: The relative speed of the Earth with respect to incoming DM wind at different times of the year will give rise to a change in DM flux, which can be detected as a change in the observed event rate [34].
- Earth's daily rotation: If the scattering event rate is dependent on the orientation of the target (in other words, if the interaction is not isotropic), the rate will depend on from which direction the DM wind is approaching, which also depends on the time of the day [35].

Both these scenarios will be discussed in detail. Since the competing background events (like neutrinos from the Sun or the black novae) do not share the same motion directions as the DM wind, being able to utilize the directionality of the DM wind would help distinguish the events of interest, making the signal-to-noise ratio higher.

Scattering Event Rates

We have already discussed the event rates to some extent, but in this section we will discuss how to evaluate the expected event rates in more detail. We can state the differential event rate as:

$$\frac{dR}{dE_R} = \frac{n_\chi}{m_N} \left\langle v_\chi \frac{d\sigma}{dE_R} \right\rangle \ , \tag{2.41}$$

where $d\sigma/dE_R$ is the differential scattering cross section. Writing the velocity averaging explicitly using the DM velocity distribution, the same expression can be written as:

$$\frac{dR}{dE_R} = \frac{\rho_\chi}{m_\chi m_N} \int d^3v v f_{\rm lab}(\mathbf{v}, t) \frac{d\sigma}{dE_R} \ , \tag{2.42}$$

where $f_{\rm lab}$ is the velocity distribution in the laboratory frame. The minimum speed detectable $v_{\rm min}$ is determined by the kinematics of the event. Following Eq. 2.39 and considering the back-scatter scenario which corresponds to the minimum DM speed that can be detected:

$$v_{\rm min} = \sqrt{\frac{m_N E_R}{2\mu_{\chi N}^2}} \tag{2.43}$$

which would correspond to the minimum boundary of the velocity integral. This expression implies the $v_{\min}$ gets smaller as the detector gets more sensitive (in other words, as E_{th} gets smaller), and $v_{\min}$ becomes larger as m_χ becomes smaller. This is expected since lighter DM particles need higher speeds to deposit the same amount of energy, therefore to be detected by the experiment with a constant energy threshold. The maximum boundary $v_{\max}$ is typically taken to be the galactic escape speed of $v_{\text{esc}} \approx 600$ km/s. An inspection of Fig. 2.5 will show that as $v_{\min}$ gets larger, the tail of the velocity distribution is probed. As a result, the tail behavior of the velocity distribution becomes significant especially for low mass DM scenarios.

Now, to proceed, we boost the DM velocity to the lab frame to be able to use the velocity distribution in the lab.

$$f_{\text{lab}}(\mathbf{v}) = f\left(\mathbf{v} + \mathbf{v}_{\text{obs}}(t)\right), \text{ where } \mathbf{v}_{\text{obs}}(t) = \mathbf{v}_0 + \mathbf{v}_e(t). \tag{2.44}$$

$v_0 \approx 220$ km/s is the Sun's speed around the galactic center and $v_e \approx 30$ km/s is the speed of the Earth around the sun. Combining Eq. 2.42 and Eq. 2.44, we get:

$$\frac{dR}{dE_R} = \frac{\rho_\chi}{m_\chi m_N} \int d^3v v f\left(\mathbf{v} + \mathbf{v}_{\text{obs}}(t)\right) \frac{d\sigma}{dE_R} \tag{2.45}$$

To proceed further, one needs to make assumptions about the form of the differential scattering cross section $d\sigma/dE_R$ which is model dependent. Therefore we will consider a sample interaction model by using effective operators, following Ref. [36].

Incorporating Specific DM-SM Interactions

Since electroweak interaction has historically been a source of "new physics", and further implied by the WIMP miracle, considering a Fermi four-interaction as an effective theory would be a good starting point. We focus on a spin-1/2 Dirac Fermion DM and the interaction with the SM particles happens through the mediator ϕ. To include various possibilities, we do not make any assumptions about the mass or the spin of the mediator particle. To start exploring the widely studied phenomenon of DM-nucleon interaction, we further assume the interacting SM particles are quarks Q. In the light of these, the effective interaction can be written down as:

$$\mathcal{L} = g'\left(g, q^2, m_\phi\right) \bar{\chi}\Gamma_\chi \chi \bar{Q}\Gamma_Q Q \ . \tag{2.46}$$

For completeness, $\Gamma_{\chi,Q}$ could be any of $\{I, \gamma^5, \gamma^\mu, \gamma^\mu\gamma^5, \sigma^{\mu\nu}, \sigma^{\mu\nu}\gamma^5\}$, and $g'\left(g, q^2, m_\phi\right)$ denotes a generic effective coupling (with g denoting the bare coupling). $g'\left(g, q^2, m_\phi\right)$ is proportional to $1/m_\phi^2$ and $1/q^2$ for heavy mediator $\left(q^2 \ll m_\phi^2\right)$ and light mediator $\left(q^2 \gg m_\phi^2\right)$ scenarios respectively.

For the next step we follow the usual procedure of effective theory mapping in the nonrelativistic limit. We will map the quark operators to the target particle operators (nucleons for this case) to get the amplitude $\mathcal{M}$ for the DM-nuclei interaction. Then we will utilize the spinor algebra to evaluate this amplitude in the nonrelativistic limit. As a final step,

we will use Fermi's golden rule to get the differential scattering cross section $d\sigma/dE_R$ from the nonrelativistic amplitude $\mathcal{M}_{\rm nr}$. This procedure is best demonstrated by focusing on an example Lagrangian, which we do below by considering a spin-independent interaction.

$$\mathcal{L}_1 = g\bar{\chi}\chi\bar{Q}Q \ . \tag{2.47}$$

For simplicity, we assume an interaction with a heavy mediator (which is also called short range or contact interaction) therefore the coupling g is independent of the momentum transfer q. What we are interested in is the interactions with nucleons (n, p). Accordingly, we map the interaction terms to the nucleon operators. This would give us an amplitude $\mathcal{M}$ that has terms of the form $\langle n|\bar{Q}Q|n\rangle$ and $\langle p|\bar{Q}Q|p\rangle$. Such terms can be evaluated using the QCD energy-momentum tensors [37]. Conveniently, fraction of a nucleon mass accounted by a quark flavor q is defined as $m_n f^n_{T_q} \equiv \langle n \left| m_q \bar{Q}Q \right| n \rangle$ and this way the couplings can be stated as:

$$f_n = \sum_{q=u,d,s} m_n \frac{g}{m_q} f^n_{T_q} + \frac{2}{27} f^n_{T_G} \sum_{q=c,b,t} m_n \frac{g}{m_q} \ , \tag{2.48}$$

where $f^n_{T_G} = 1 - \sum_{q=u,d,s} f^n_{T_q}$ [38]. When the couplings are mapped into nucleon couplings this way, the interaction amplitude can be recast as:

$$\mathcal{M} = f_p \bar{\chi}\chi\bar{p}p + f_n \bar{\chi}\chi\bar{n}n \ . \tag{2.49}$$

The expression above assumes that protons are neutrons behave as single target particles and their internal structures are not resolved (in other words, we are in the nonrelativistic limit). The modifications required if the momentum transfer is large enough to probe the internal structure of the nucleons will be discussed below. For now, we stick to this nonrelativistic limit. Noting that $\bar{p}p$ and $\bar{n}n$ are the proton and the neutron numbers respectively, $\mathcal{M}$ can be recast in terms of the nucleon fields N:

$$\mathcal{M} = \left[Z f_p + (A - Z) f_n \right] \bar{\chi}\chi \bar{N}\Gamma_N N \ , \tag{2.50}$$

where A and Z are the mass and the atomic number respectively. The most general form of the Lorentz-invariant matrix Γ_N, since the answer depends only on q_μ and P_μ, gives rise to:

$$\bar{N}\Gamma_N N = \bar{N}N + \bar{N}\gamma^\mu N q_\mu + \bar{N}\gamma^\mu N P_\mu + \bar{N}\sigma^{\mu\nu} N q_\mu P_\nu \ . \tag{2.51}$$

Utilizing the Dirac equation's implications $\gamma^\mu p_\mu N(p) = m_N N(p)$ and $\bar{N}\left(p'\right)\gamma^\mu p'_\mu = m_N \bar{N}\left(p'\right)$, the amplitude $\mathcal{M}$ can be simplified to:

$$\mathcal{M} = \left[Z f_p + (A - Z) f_n \right] \bar{\chi}\chi \bar{N}N \ . \tag{2.52}$$

Before we proceed further, this is a good point to incorporate the possibility of high momentum transfer events probing the structure of the nucleus. If the interaction is coherent over all nucleons as in the case of the one we are considering, a form factor can be obtained

by taking the Fourier transform of the mass distribution in the nucleus. This results in the Helm form factor [39];

$$F(q) = 3e^{-q^2 s^2/2} \left(\frac{\sin(qr_n) - qr_n \cos(qr_n)}{(qr_n)^3} \right) , \tag{2.53}$$

where r_n is the nucleus' radius, and $s \simeq 0.9$ fm. With this, the more general form of $\mathcal{M}$ can be written as:

$$\mathcal{M} = [Zf_p + (A-Z)f_n]\, \bar{\chi}\chi \bar{N} N F(q) . \tag{2.54}$$

Not surprisingly, when the q is small, $F(q) \simeq 1$ and we retrieve the Eq. 2.52. Now the next step is to find the nonrelativistic limit of the amplitude $\mathcal{M}$. We will use spinor algebra following the procedure outlined in the Quantum Field Theory textbooks:

$$N^s(p) = \begin{pmatrix} \sqrt{p\cdot\sigma}\xi^s \\ \sqrt{p\cdot\bar{\sigma}}\xi^s \end{pmatrix} . \tag{2.55}$$

Above s denotes spin, and ξ is a two-component spinor. In the nonrelativistic limit,

$$\sqrt{p\cdot\sigma} \approx \sqrt{m_N - \mathbf{p}\cdot\sigma} \approx \sqrt{m_N}\left(1 - \frac{\mathbf{p}\cdot\sigma}{2m_N}\right) \tag{2.56}$$

which yields:

$$\begin{aligned} \bar{N}^{s'}(p')\, N^s(p) &= \left(N^{s'}(p')\right)^\dagger \gamma^0 N^s(p) \\ &= \left(\sqrt{p'\cdot\sigma}\xi^{s'\dagger}, \sqrt{p'\cdot\bar{\sigma}}\xi^{s'\dagger}\right) \begin{pmatrix} 0 & 1 \\ 1 & 0 \end{pmatrix} \begin{pmatrix} \sqrt{p\cdot\sigma}\xi^s \\ \sqrt{p\cdot\bar{\sigma}}\xi^s \end{pmatrix} \\ &= \xi^{s'\dagger}\left(\sqrt{p'\cdot\bar{\sigma}}\sqrt{p\cdot\sigma} + \sqrt{p'\cdot\sigma}\sqrt{p\cdot\bar{\sigma}}\right)\xi^s \\ &\approx 2m_N \xi^{s'\dagger}\xi^s , \end{aligned} \tag{2.57}$$

where s and s' denote the spins of incoming and outgoing nuclei respectively. A similar treatment of $\bar{\chi}\chi$ gives $\bar{\chi}\chi \approx 2m_\chi \xi^{r'\dagger}\xi^r$ where r and r' denote the spins of incoming and outgoing DM particles. This makes the nonrelativistic amplitude $\mathcal{M}_{\rm nr}$:

$$\mathcal{M}_{\rm nr} = 4m_N m_\chi \left[Zf_p + (A-Z)f_n\right] F(q) \xi^{s'\dagger}\xi^s \xi^{r'\dagger}\xi^r . \tag{2.58}$$

We conveniently drop $4m_N m_\chi$ because this part originates from the relativistic normalization convention, and get the differential scattering cross section as:

$$\frac{d\sigma}{dE_R} = \frac{2m_N}{\pi v^2} \frac{1}{(2J_N+1)(2J_\chi+1)} \sum_{\rm s,s',r,r'} \left[Zf_p + (A-Z)f_n\right]^2 F^2(q) \left|\xi^{s'\dagger}\xi\right|^2 \left|\xi^{r'\dagger}\xi^r\right|^2 , \tag{2.59}$$

where J_N and J_χ are the nuclear and the DM spin respectively. After spin summations are evaluated, we get:

$$\frac{d\sigma}{dE_R} = \frac{2m_N}{\pi v^2} \left[Zf_p + (A-Z)f_n\right]^2 F^2(q) . \tag{2.60}$$

Not surprisingly, we observe that $\frac{d\sigma}{dE_R}$ is independent of spin, since we had started with a spin independent Lagrangian. We also see that if the coupling to protons and neutrons are the same, we get $\frac{d\sigma}{dE_R} \propto A^2$ which indicates a coherent coupling to all nucleons in the target nucleus.

Similarly, a spin-dependent Lagrangian is expected to give a spin-dependent differential cross section. Following an example in Ref. [37], we can consider the interaction:

$$\mathcal{L} = g\bar{\chi}\gamma_\mu\gamma^5\chi\bar{Q}\gamma^\mu\gamma^5 Q \ , \tag{2.61}$$

where g denotes the coupling. This would give rise to a differential cross section:

$$\frac{d\sigma}{dE_R} = \frac{16 m_N}{\pi v^2} G_F^2 J(J+1)\Lambda^2 \frac{S(|\boldsymbol{q}|)}{S(0)} \ , \tag{2.62}$$

where $S(|\boldsymbol{q}|)$ is the spin-independent form factor that would be obtained from the nuclear calculations, $\Lambda = (1/J)\left[a_\mathrm{p}\left\langle S_\mathrm{p}\right\rangle + a_\mathrm{n}\left\langle S_\mathrm{n}\right\rangle\right]$, G_F is the Fermi coupling constant, $\left\langle S_\mathfrak{p}\right\rangle = \left\langle N\left|S_\mathrm{p}\right|N\right\rangle$ is the spin of the proton part of the nucleus (and similar for $\left\langle S_\mathfrak{n}\right\rangle$), and a_p and a_n are the effective couplings of the DM particle to the protons and the neutrons respectively. One observation we make is, for the case of spin-dependent interactions the interaction is not coherent over all the nucleus. Accordingly, we do not see an A^2 dependence in the differential cross section. This lack of "constructive interference" among target constituents results in smaller expected interaction rates. Accordingly, the relevant bounds are weaker compared to the bounds for spin-independent interactions. In Fig. 2.6, we see a compilation of the bounds and the projected bounds [30]. The figure explores the scenario of spin independent scattering with a heavy mediator. The target material used depends on the specific experiment, thus it is convenient to factor out the nuclei-dependence to write the bounds in terms of scattering from individual nucleons:

$$\sigma_\mathrm{N} = \frac{\mu_{N\chi}^2}{\mu_{n\chi}^2} A^2 \sigma_n, \qquad \text{where } \sigma_\mathrm{N} \text{ is given by } \frac{d\sigma}{dE_R} = \frac{2m_N}{4\mu_{N\chi}^2 v^2}\sigma_\mathrm{N} F^2(q) \ . \tag{2.63}$$

Accordingly, the cross section value constrained in Fig. 2.6 is σ_n.

Some properties common to all shown "WIMP detection" experiments are: They all lose sensitivity at around $m_\chi \simeq 10$ GeV due to experimental energy thresholds (depositing enough energy to induce a detectable signal gets harder as the mass gets smaller). Sensitivities also gradually decrease with increasing mass because the expected DM number density decreases (hence the positive slope of the constraint curves at high masses). These experiments probed the 10 GeV $-$ 100 GeV range the best, however DM has not been detected yet.

Form of the σ_n can be evaluated further when focused on specific models. For instance, for tree-level scattering through the Z boson:

$$\sigma_n \approx \frac{g^4\mu_n^2}{4\pi m_Z^4} \approx 10^{-39}\ \mathrm{cm}^2 \ , \tag{2.64}$$

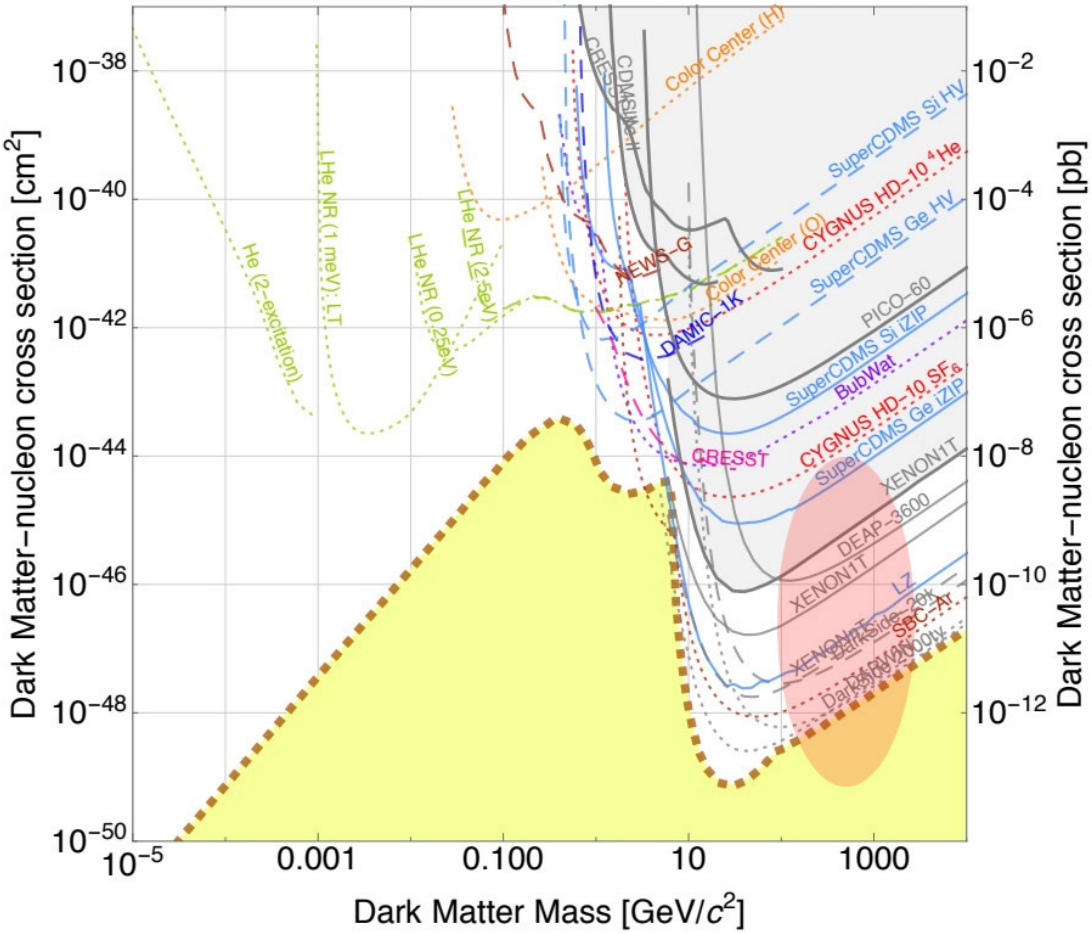

Figure 2.6: Current and projected constraints for the DM-nucleon interaction (with 90% confidence intervals) [30]. Solid, dashed and dotted lines indicate short, medium and long term projections respectively. Red circle indicates the rough prediction region for MSSM. Gray-shaded areas indicate the best experimental bounds, and yellow region indicates the cross section values where the experiments become sensitive to scattering of neutrinos from target nuclei (Note that the figure reflects the bounds and constraints from 2017, the year figure was produced.)

or for neutralinos scattering through Higgs in MSSM, the σ_n can be stated as [40]:

$$\sigma_n \approx 8.3 \times 10^{-42}\ \mathrm{cm}^2 \left(\frac{Z_d}{0.4}\right)^2 \left(\frac{\tan\beta}{30}\right)^2 \left(\frac{100\ \mathrm{GeV}}{m_H}\right)^4 , \tag{2.65}$$

with Z_d, $\tan\beta$ and m_H denoting the Higgsino fraction, the mixing angle and the Higgs mass respectively.

A Closer Look: Elastic Neutralino Scattering

In this subsection we demonstrate the model dependence of scattering cross sections further, specifically by focusing on the case of neutralinos. In MSSM, the neutralinos are the neutral fermion mass eigenstates that are mixtures of $\left(\tilde{B}, \tilde{W}_3, \tilde{H}_1^0, \tilde{H}_2^0\right)$. Bino ($\tilde{B}$), Wino ($\tilde{W}_3$), and two Higgsinos ($\tilde{H}_1^0, \tilde{H}_2^0$) are the fermionic supersymmetric partners of the hypercharge gauge boson, SU(2) neutral gauge boson (W^0), and two neutral MSSM Higgses respectively. Even though a deep understanding of SUSY is not required to follow the argument in this subsection, in case the reader is interested, one or few of the great reviews on supersymmetry (like Refs. [37, 41]) can be consulted.

The mass matrix depicting the mixing of the neutralino in the $\left(\tilde{B}, \tilde{W}_3, \tilde{H}_1^0, \tilde{H}_2^0\right)$ basis after the electroweak symmetry breaking is:

$$\mathcal{M}_{\tilde{\chi}^0} = \begin{pmatrix} M_1 & 0 & -\frac{g' v_1}{\sqrt{2}} & +\frac{g' v_2}{\sqrt{2}} \\ 0 & M_2 & +\frac{g v_1}{\sqrt{2}} & -\frac{g v_2}{\sqrt{2}} \\ -\frac{g' v_1}{\sqrt{2}} & +\frac{g v_1}{\sqrt{2}} & 0 & -\mu \\ +\frac{g' v_2}{\sqrt{2}} & -\frac{g v_2}{\sqrt{2}} & -\mu & 0 \end{pmatrix} \tag{2.66}$$

with g and g' denoting the SU(2) and U(1) hypercharge coupling constants respectively, and $v_{1,2}$ being the vacuum expectation value (VEV) of the real, neutral parts of the two Higgs doublets. The corresponding mass parameters are the gaugino masses M_1 and M_2, and the supersymmetric Higgs-higgsino mass parameter μ. In this basis, the neutralino can be written as:

$$\tilde{\chi}_i^0 = N_{i1}\tilde{B} + N_{i2}\tilde{W}_3 + N_{i3}\tilde{H}_1^0 + N_{i4}\tilde{H}_2^0. \tag{2.67}$$

Conveniently, the bino, wino and higgsino fractions for the lightest neutralino are defined to be $|N_{11}|^2$, $|N_{12}|^2$, and $(|N_{13}|^2 + |N_{14}|^2)$ respectively. The composition of the lightest neutralino is determined by the relative magnitudes of the mass parameters M_1, M_2 and μ, and the phenomenology of neutralino direct detection is highly dependent on the composition of the neutralino. Below we focus on some important cases to demonstrate the significant effect the neutralino composition has on the scattering cross section. Following Ref. [42], we rewrite the neutralino in the photino, zino and higgsinos basis:

$$\chi = \gamma_1\tilde{\gamma} + \gamma_2\tilde{Z} + \gamma_3\tilde{H}_1^0 + \gamma_4\tilde{H}_2^0. \tag{2.68}$$

The dominant contribution to spin-independent cross section for the elastic scattering of a neutralino with a nucleus i of atomic number A is due to the exchange of H_2 and $\tilde{q}$ (squark). Assuming the squarks are heavier than all the other particles involved, and assuming they are degenerate for simplicity, the coherent spin-independent contribution to the cross section is given by [42]:

$$\sigma_i^{\mathrm{SI}} = \frac{4\sqrt{2}}{\pi} G_{\mathrm{F}} m_{\mathrm{Z}}^2 \frac{m_i^2 m_\chi^2}{(m_i + m_\chi)^2} A^2 \left[\frac{g_{\mathrm{H}}^2}{m_{\mathrm{H}_2}^4} + \epsilon \frac{g_{\mathrm{H}} g_{\tilde{\mathrm{q}}}}{m_{\mathrm{H}_2}^2 m_{\tilde{\mathrm{q}}}^2} + \frac{3}{4} \frac{g_{\tilde{\mathrm{q}}}^2}{m_{\tilde{\mathrm{q}}}^4} \right]. \tag{2.69}$$

The couplings $g_{\rm H}$ and $g_{\tilde{\rm q}}$ are:

$$\begin{aligned} g_{\rm H} &= \left(g^{\rm gg}_{\phi \rm NN} \frac{2k^{(2)}_{\rm u} + k^{(2)}_{\rm d}}{3} + g^{\rm ss}_{\phi \rm NN} k^{(2)}_{\rm d} \right) (\gamma_3 \sin\alpha + \gamma_4 \cos\alpha)\, \gamma_2 \\ g_{\overline{\rm q}} &= \left(g^{\rm gg}_{\phi \rm NN} \frac{2k^{\tilde{q}}_{\rm u} + k^{\overline{\rm d}}_{\rm d}}{3} + g^{\rm s\overline{s}}_{\phi \rm NN} k^{\tilde{\rm d}}_{\rm d} \right) \gamma_2, \end{aligned} \tag{2.70}$$

where

$$g^{\rm gg}_{\phi \rm NN} = -\left(\sqrt{2} G_{\rm F}\right)^{1/2} \frac{\alpha_{\rm s}}{4\pi} \frac{\langle N|GG|N\rangle}{\bar{\Psi}_{\rm N}\Psi_{\rm N}} \simeq 5 \times 10^{-4}, \tag{2.71}$$

is the coupling of the gluons inside the nucleon to a standard Higgs through one loop of heavy quarks. The crucial part of equations 2.69 and 2.70 for our discussion is their dependence on the fractions γ_i. It can be seen that there are multiple terms in Eq. 2.69 that are of the form $\sigma^{\rm SI}_i \propto \sim (\gamma_3+\gamma_4)^a(\gamma_2)^b$ where a and b are 1 or 2 depending on the term. Qualitatively, these terms can be interpreted as the higgsino fractions multipled by the gaugino (bino plus wino) fractions. Accordingly, the spin independent contribution to cross section is maximized for mixed neutralino states, and suppressed for pure states.

On the other hand, if we focus on the spin-dependent cross section for the elastic scattering of a neutralino with a nucleus i, which is driven by the coupling to the Z boson, we get [42]:

$$\sigma^{\rm SD}_{\rm N} = 3 \frac{G^2_{\rm F}}{2\pi} \alpha_{\rm Z} g^2_{\rm A} \frac{m^2_\chi m^2_{\rm N}}{(m_\chi + m_{\rm N})^2} \tag{2.72}$$

where $\alpha_{\rm Z} = (\gamma^2_4 - \gamma^2_3)^2$. Again, the important aspect for our discussion is the dependence on the γ_i fractions. This time the dependence on fractions is rather nontrivial: The coupling (and therefore the rate) vanishes for pure higgsino states.

To summarize the conclusions in this subsection:

- The spin-independent contribution to cross section (through H_2 and $\tilde{q}$ exchange) is maximized for the mixed states and suppressed for the pure states.
- The spin-dependent contribution to the cross section (through Z exchange) depends on the higgsino fractions, but vanishes for pure higgsino states.

As can be seen, the MSSM neutralino serves as a perfect demonstration for the dependence of the scattering cross sections on the assumptions and the parameters of the underlying models.

Kinematics of Direct Detection

So far we have discussed the ways of constraining the expected interaction cross section of DM and targets. We also have mentioned that a crucial step in DM detection is to increase

the signal-to-noise ratio, so that we can be sure that our signal is a DM signal. Considering the diversity and the abundance of cosmic particle accelerators that could give rise to false detection signals, the task of background reduction is significant. Two of the most popular methods proposed for background reduction are, to utilize the changing directionality of incoming DM particles with respect to the annual and daily motions of the Earth. The DM is expected to form a halo around the galactic center. Accordingly, the direction and the flux of incoming DM particles depend on both the time of the year and the day. In this subsection we explore utilizing the expected annual and daily rate modulations to improve the signal-to-noise ratio in DM detection.

Annual Modulation

If we restate the Eq. 2.44:

$$f_{\text{lab}}(\mathbf{v}) = f\left(\mathbf{v} + \mathbf{v}_{\text{obs}}(t)\right), \text{ where } \mathbf{v}_{\text{obs}}(t) = \mathbf{v}_0 + \mathbf{v}_e(t) \tag{2.73}$$

and expand the lab velocity as:

$$\mathbf{v}_{\text{obs}}(t) \approx \mathbf{v}_0 \left(1 + \epsilon \cos\left[\omega\left(t - t_0\right)\right] + \cdots\right) \ , \tag{2.74}$$

where $\omega = 2\pi/\text{year}$ is the angular frequency of the Earth around the sun, t_0 is the initial time that corresponds to the initial phase of the oscillation, and ϵ is conveniently defined as $\tilde{v}_e/v_0$ where $\tilde{v}_e$ is the projection of Earth's velocity along the direction of the Sun's velocity. Since ϵ is small, to a good approximation, the velocity distribution can be expanded as:

$$f\left(\mathbf{v} + \mathbf{v}_{\text{obs}}(t)\right) \simeq f\left(\mathbf{v} + \mathbf{v}_0\right) + \epsilon \cos\left[\omega\left(t - t_0\right)\right] f'\left(\mathbf{v} + \mathbf{v}_0\right) + \cdots \tag{2.75}$$

which allows us to write down the rate as:

$$\frac{dR}{dE} = A_0 + A_1 \cos\left[\omega\left(t - t_0\right)\right] + \cdots \tag{2.76}$$

Eq. 2.76 shows us that the rate has two terms: a constant term and a term that modulates with the period of a year. The expansion yields higher terms as well which may become significant depending on the details of the velocity distribution. However, here we will consider only the two terms shown above for simplicity.

This annual modulation can be interpreted physically. DM dust is assumed to be at rest with respect to the galactic center, therefore its velocity in the lab frame is equivalent to the opposite of the Sun's velocity. Fig. 2.7 schematically shows that the relative speed of incoming DM particles depends on the direction of the velocity of the Earth. This means the flux of incoming DM particles varies around the year, resulting in an expected annual modulation in the DM scattering rate.

In addition, Fig. 2.7 includes another factor that affects the DM flux: Gravitational focusing [34]. If, with respect to the incoming DM particles, the Earth is "behind" the Sun,

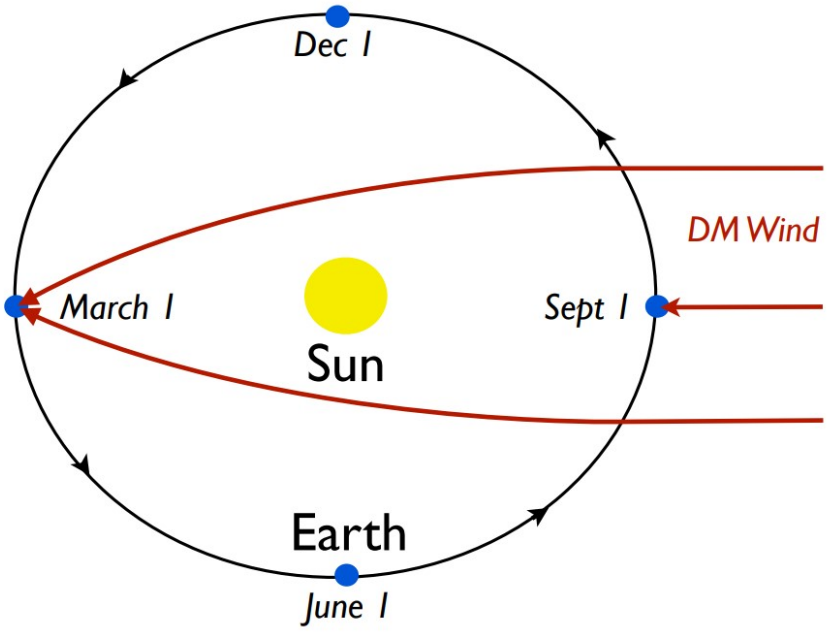

Figure 2.7: A schematic representation of the annual modulation of the flux of incoming DM particles, from Ref. [34].

the Sun acts as a gravitational lens collecting the DM particles closer as shown in Fig. 2.7. On the contrary, if the Earth is in front of the Sun in terms of facing the DM particles first, the trajectories of incoming DM particles are not altered in a similar way. This effect also causes a change in flux which depends on relative orientations of the Earth and the Sun, and the total effect of the annual modulation should be evaluated by considering these multiple factors altogether. A unique aspect of this gravitational focusing is, it affects the heavier DM particles more therefore the trajectories of the heavier DM particles are bent more compared to the lighter ones. This effect theoretically provides a probe to isolate the different effects in annual modulation with higher confidence, which helps to reduce the signal-to-noise ratio.

Daily Modulation

In the previous section, we have explored the expected annual modulation in the scattering rate, which depended on the changing flux of incoming DM particles throughout the year. In this section we will consider the daily modulation of the expected rate. As the Earth rotates around its axis, the relative velocity (therefore the speed) of incoming DM particles with respect to the detector changes (visualized in Fig. 2.8). This gives rise to a change in flux. Also, more importantly, it may boost the speed of the incoming DM particles (in the lab frame) and cause them to deposit higher recoil energies. This makes DM particles easier to detect. To explore this possibility, we refer back to Eq. 2.45.

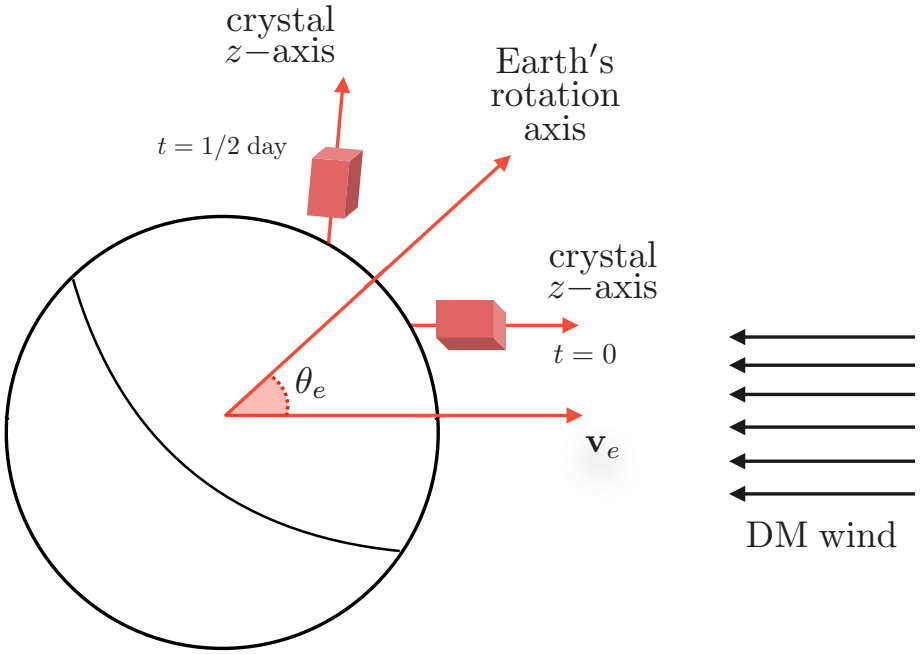

Figure 2.8: A visualization of the daily modulation of incoming DM flux, taken from Ref. [7]

$$\frac{dR}{dE_R} = \frac{\rho_\chi}{m_\chi m_N} \int d^3v v f\left(\mathbf{v} + \mathbf{v}_{\rm obs}(t)\right) \frac{d\sigma}{dE_R} \ . \tag{2.77}$$

As we can remember from the Fermi's golden rule, $\frac{d\sigma}{dE_R}$ has an energy conservation delta function.

$$\frac{dR}{dE_R} \propto \delta\left(E_f - E_i - \omega\right) \ . \tag{2.78}$$

Above we denote the deposited energy with ω. This energy conservation condition can be applied to the velocity integral:

$$g(\boldsymbol{q}, \omega) \equiv \int d^3v f_\chi(\boldsymbol{v}) 2\pi\delta\left(E_f - E_i - \omega\right) \ . \tag{2.79}$$

So far what we have done does not have a physical significance, we simply started thinking of the energy conserving delta function as a part of velocity integral rather than the $\frac{dR}{dE_R}$. However, when the commonly used Maxwell-Boltzmann velocity distribution is used, the integral in Eq. 2.79 can be evaluated analytically to find:

$$g(\boldsymbol{q}, \omega) = \frac{2\pi^2 v_0^2}{N_0 q} \left[\exp\left(-v_-^2/v_0^2\right) - \exp\left(-v_{\rm esc}^2/v_0^2\right)\right] \ , \tag{2.80}$$

where

$$v_- = \min\left\{\frac{1}{q}\left|\boldsymbol{q}\cdot\boldsymbol{v}_{\rm e} + \frac{q^2}{2m_\chi} + \omega\right|, v_{\rm esc}\right\} \ . \tag{2.81}$$

The $g(\boldsymbol{q},\omega)$ function serves as a phase-space weight factor which determines where in the phase space the events are favored or suppressed kinematically. To investigate the behavior of $g(\boldsymbol{q},\omega)$ function further, we conveniently define

$$v_* \equiv \frac{q}{2m_\chi} + \frac{\omega}{q}. \tag{2.82}$$

- For $v_* \geq v_{\rm esc} + v_{\rm e}$, we would have $v_- = v_{\rm esc}$ and the $g(\boldsymbol{q},\omega)$ function would be zero at all times. This corresponds to the kinematically forbidden region.
- For $v_{\rm e} \leq v_* < v_{\rm esc} + v_{\rm e}$, the $g(\boldsymbol{q},\omega)$ function is maximized when $\hat{\boldsymbol{q}} \cdot \hat{\boldsymbol{v}}_{\rm e} = -1$. To state this qualitatively, in this region, the rate is expected to get maximized when the relative directions of $\hat{\boldsymbol{q}}$ and $\hat{\boldsymbol{v}}_{\rm e}$ correspond to full back-scatter.
- Finally, in the $v_* \leq v_{\rm e}$ region, $g(\boldsymbol{q},\omega)$ function is maximized when $\hat{\boldsymbol{q}} \cdot \hat{\boldsymbol{v}}_{\rm e} = -v_*/v_e$. In this region the events are kinematically allowed for any momentum transfer direction, therefore $g(\boldsymbol{q},\omega)$ function is always positive for any $\hat{\boldsymbol{q}}$.

Behaviors explained above in these three regions are visualized in Fig. 2.9. Not surprisingly, the kinematic weight assigned to events by the $g(\boldsymbol{q},\omega)$ function depends on the relative orientations of momentum transfer $\hat{\boldsymbol{q}}$ and Earth velocity's direction $\hat{\boldsymbol{v}}_{\rm e}$. Since $\hat{\boldsymbol{v}}_{\rm e}$ changes with time during the day, the kinematically favored regions in the scattering events also vary with time. This gives rise to the daily modulation of the rate of scattering events. The potential for utilizing this modulation for reducing background and improving signal-to-noise ratio was explored in recent works such as Refs. [7, 43–45].

2.4 A Glimpse Into the Hidden Sector: Asymmetric Dark Matter Nuggets

The dark matter conundrum is one of the multiple puzzles beyond what is explained by the standard pictures in particle physics and cosmology. Many popular attempts to tackle the DM question assume minimalist extensions to the standard picture: DM is a single type of stable particle for which the relic density is set by the thermal freeze-out mechanism. In this picture, the DM particles interacted with and annihilated each other as the Universe was cooling down, and eventually when the temperature fell below the freeze-out temperature, the relic density was set. In Sec. 2.2 we have discussed how the DM masses around the weak interaction range ($\sim$ 1 TeV) correspond to the observed DM relic density, resulting in a celebrated "coincidence" called WIMP miracle. Considering the significance of the weak-scale when it comes to looking beyond the Standard Model, this WIMP framework naturally attracted the interest of both theorists and experimentalists. As a result of being a minimal extension to the standard picture, the WIMP framework provided sharp predictions for experimental programs to explore.

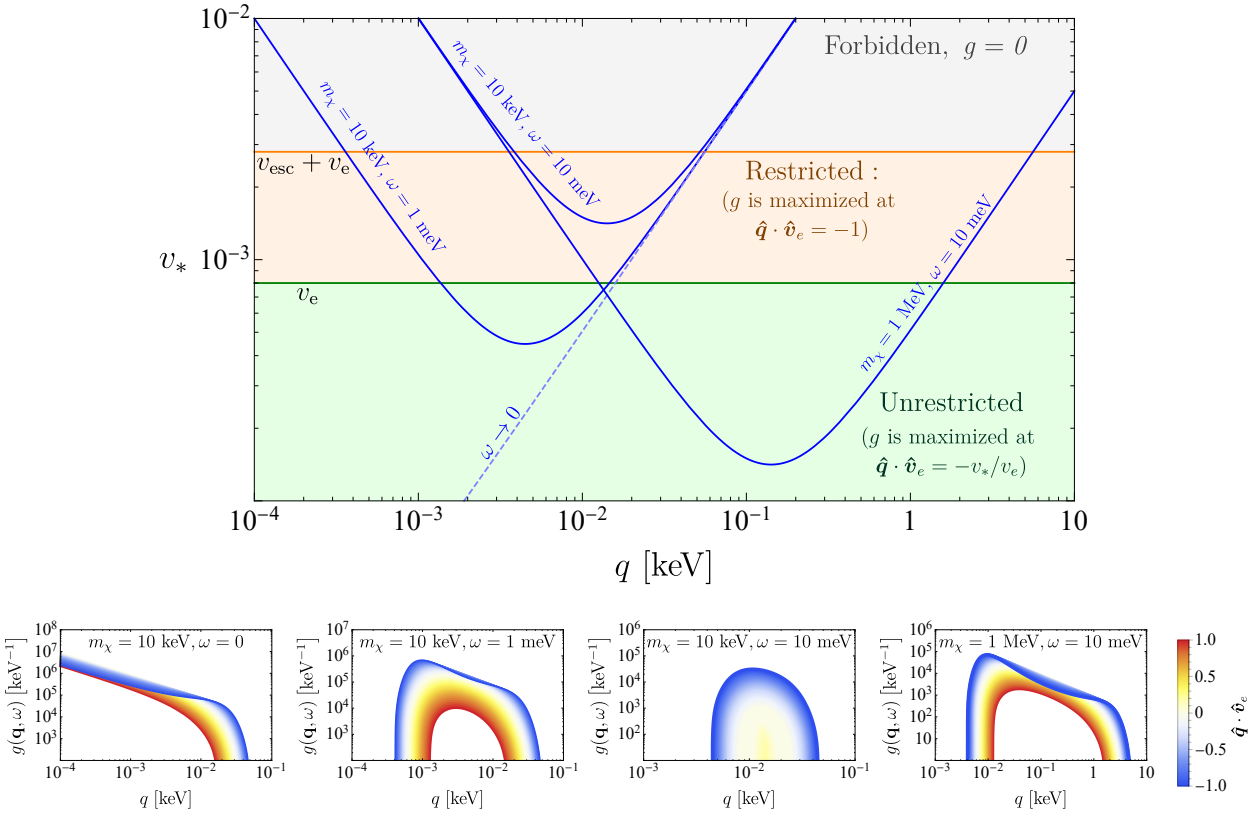

Figure 2.9: **Top:** A visualization of $v_* \equiv \frac{q}{2m_\chi} + \frac{\omega}{q}$ versus momentum transfer q for various m_χ and ω values. By comparing v_* to $v_{\rm e}$ and $v_{\rm e} + v_{\rm esc}$ we can observe the different regions described in the text for $g(\boldsymbol{q}, \omega)$. **Bottom:** $g(\boldsymbol{q}, \omega)$ versus q for several fixed m_χ, ω values, with varying $\hat{\boldsymbol{q}} \cdot \hat{\boldsymbol{v}}_{\rm e}$. The $g(\boldsymbol{q}, \omega)$ function weights different $\hat{\boldsymbol{q}}$ directions according to their relative orientation with respect to $\boldsymbol{v}_{\rm e}(t)$. All the plots in this figure are from Ref. [8]

Even though the WIMP picture of DM sounds promising, this minimalist way of tackling the DM problem is not the only way. It is possible to imagine a DM particle spectrum like the one in the Standard Model, with its own dynamics, gauge groups and quantum numbers. In other words, there could be a "hidden sector" of DM particles that interact with the SM particles via weakly interacting mediators or portals (in addition to gravity). Such dark sectors are also motivated by top-down models like string theory and supersymmetry. Further motivation for these nonminimal DM sectors comes from other problems beyond the Standard Model, like hierarchy problem, baryon asymmetry or CP violation. The possibility of resolving multiple beyond the SM puzzles with the same framework motivated many theorists to introduce nonminimal dark hidden sectors. Some famous examples are:

- Axions: Introducing a Peccei-Quinn symmetry [46, 47] to solve the strong CP problem predicts a sub-eV particle (axion) [48] that interacts weakly with the SM particles. The aforementioned properties make this particle a natural DM candidate.
- DM can be supersymmetric neutralinos, therefore can be incorporated in the supersymmetry framework [37].
- Another DM candidate, sterile neutrinos, aim to solve the neutrino oscillations problem [49].
- The DM particles could have an asymmetry in their abundance similar to the baryon asymmetry, which would help to explain the similarity of observed DM and baryon abundances [29].

The list above is not comprehensive, and there is a wide range of hidden sector DM models (a visual representation summarizing the proposed DM models can be seen in Fig. 2.10). In the following sections, we will discuss the idea of "asymmetric dark matter" (ADM) and the composite states of it called "nuggets", as an example hidden sector model.

Asymmetric Dark Matter

In the standard WIMP picture, the production of DM by means of thermal freeze-out is not relevant to the baryon asymmetry. The observed baryon abundance is the result of the generation of baryon asymmetry, which apparently is not related to the abundance of WIMPs. However, observations indicate that the abundances of DM and baryons are close:

$$\frac{\Omega_{\mathrm{b}}}{\Omega_{\mathrm{dm}}} \simeq 0.2. \tag{2.83}$$

The fact that these two seemingly unrelated mechanisms produce similar amounts of the Universe's energy content is puzzling, which naturally leads theorists to consider a possible similarity in the production mechanisms. Why would two supposedly irrelevant production mechanisms result in similar amounts of matter? Could there be a relation between them? Could the DM and baryons have a common or related origin? These questions are the main motivations behind the asymmetrically produced DM models.

There is a wide variety of ADM theories [29]. We will focus on the properties common to the popular ADM models.

First, the generation of asymmetry in the dark sector should also satisfy the Sakharov conditions: the (dark) baryon number violation, C and CP violation, and interactions out of thermal equilibrium. The first condition is required by the definition of (dark) baryon asymmetry. The C and CP symmetry violations ensure the distinguishability of (dark) matter from anti-matter. The requirement for interactions out of equilibrium allow the relic DM particles to "survive" annihilation therefore prevents the asymmetry generated from getting washed out.

The ADM mechanism can be thought of as consisting of three steps:

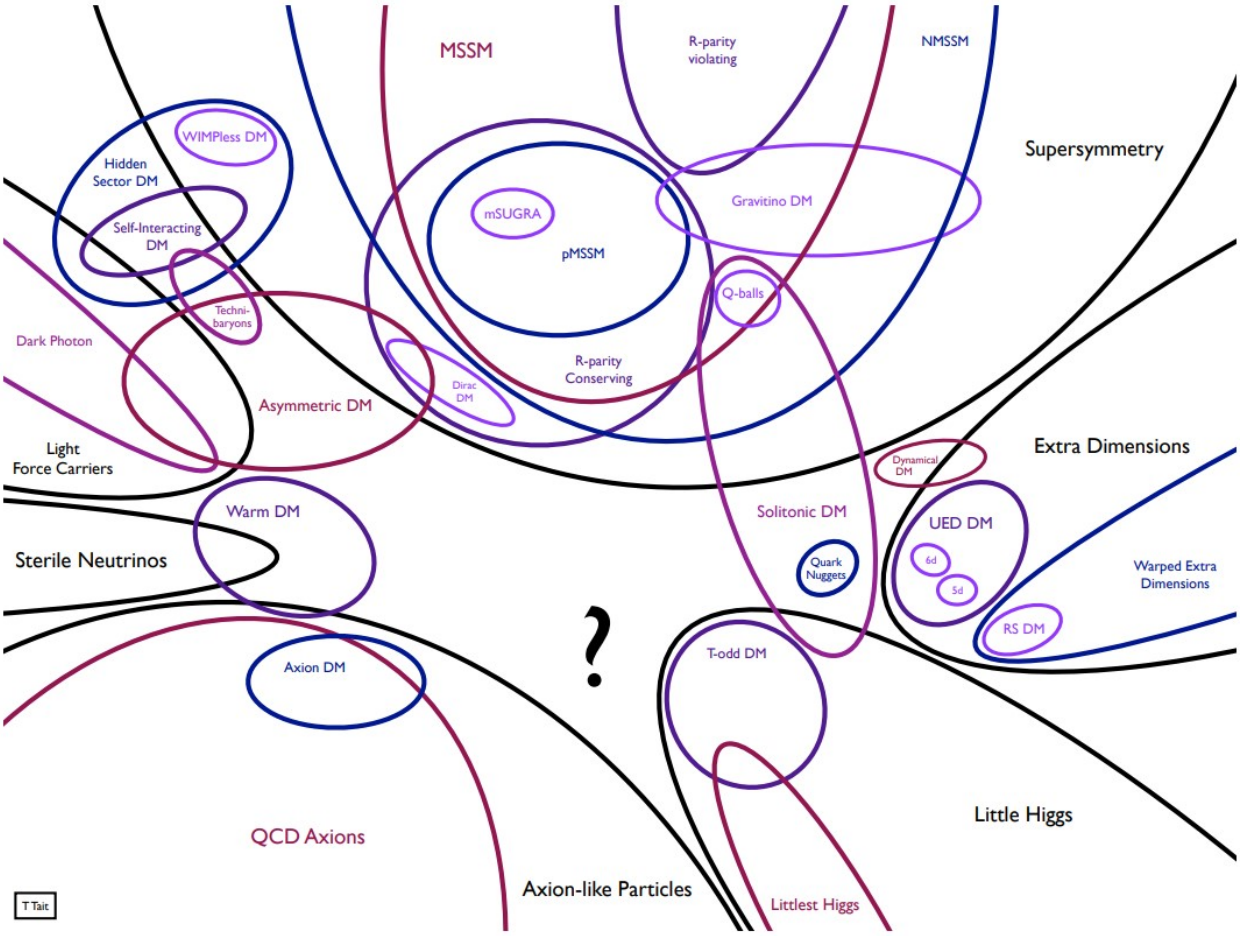

Figure 2.10: A visual representation of the landscape of DM candidates, by T. Tait (Taken from Ref. [50]).

i) An asymmetry needs to be generated in the visible and/or dark sectors. This can be achieved in scenarios where the DM and SM particles share a common quantum number, or there is an equivalent "dark baryon number" $B_{\rm D}$ for the DM particles, similar to the baryon number for the visible particles $B_{\rm V}$. The asymmetry could have been generated in one sector and transferred to the other, or it can be generated in both sectors simultaneously.

ii) The asymmetry transfer mechanism between the dark and visible sectors loses its efficiency, freezing in the asymmetric abundances in both sectors separately.

iii) The symmetric abundances need to annihilate away, leaving only the asymmetric components of the DM and baryon abundances.

Step 1: Asymmetry Generation

One way the asymmetry can be generated is if the visible baryons and the DM particles share a common quantum number. In this case the asymmetry can be distributed between the dark and the visible sectors through relevant interactions. After these interactions decouple from the thermal plasma, the generated asymmetries would be frozen-in.

Another possibility is the generalization of the visible baryon number $B_{\rm V}$ to the dark sector, introducing a dark baryon number $B_{\rm D}$ which is also conserved at low energies. In this picture, there are multiple possibilities:

i) A linear combination of $B_{\rm D}$ and $B_{\rm V}$ could be conserved while a linearly independent combination is broken.

ii) $B_{\rm D}$ is broken while $B_{\rm V}$ is not, or vice versa.

iii) Both $B_{\rm D}$ and $B_{\rm V}$ are broken.

The scenarios described in 2 and 3 are qualitatively similar: the asymmetry is distributed between the sectors through interactions (discussed in more detail in the next subsection). Scenario 1 is different. The conserved and broken combinations can be written as:

$$\begin{aligned} B_{\rm con} &= aB_{\rm V} + bB_{\rm D}, \\ B_{\rm bro} &= cB_{\rm V} + dB_{\rm D}, \end{aligned} \tag{2.84}$$

After normalizing the coefficients and redefining, the above definitions can be simplified further:

$$\begin{aligned} B_{\rm con} &= B_{\rm V} - B_{\rm D}, \\ B_{\rm bro} &= B_{\rm V} + B_{\rm D}. \end{aligned} \tag{2.85}$$

Under these requirements, since $B_{\rm con}$ is zero before and after the asymmetry generation, the Universe produces equal amounts of $B_{\rm D}$ and $B_{\rm V}$. Accordingly, this scenario implies both sectors have the same amount of asymmetry, and the asymmetry in the hidden sector "cancels" the asymmetry in the visible sector.

Step 2: Transfer of Asymmetry

In general, transfer mechanisms can be grouped into two:

- Electroweak sphalerons: If the DM particles carry a global dark baryon number $B_{\rm D}$ the sphalerons may violate the relevant $U(1)_D$ global symmetry.

- Higher dimension operators and renormalizable interactions: Introducing an interaction between the SM quantum number $B - L$ and the dark quantum number $B_{\rm D}$ will allow scatterings inducing the chemical equilibrium. This way the asymmetry in one sector will be transferred to the other.

Step 3: Interactions Out of Equilibrium

The symmetric component of the abundance should annihilate away, which provides constraints on the pair-annihilation scattering cross sections. The relative abundances of symmetric and asymmetric components depend on the temperature when the asymmetry is produced. The DM particles can directly annihilate to light mediators, or they can annihilate through mediators heavier than themselves.

Production of Composite States: ADM Nuggets

We have discussed how the idea of ADM is analogous to SM baryons in many aspects. Pursuing this analogy further, it is natural to hypothesize bound states of ADM (called nuggets), similar to SM nuclei. If asymmetrically produced baryons can fuse to form SM nuclei throughout cosmic history, the same is possible for ADM as well. In addition to being a natural next step in SM baryon-DM resemblance, there are independent reasons that motivate the exploration of composite ADM models. To list a few:

- In the standard freeze-out scenario, particles heavier than ~ 10 TeV are not compatible with the observed DM abundance. Since the heavier ADM nuggets form in the hidden sector from the lighter constituents, they do not suffer from the aforementioned restriction, and the formation of ultra-heavy composite states is possible. Therefore if ADM nuggets exist they can be way heavier than 10 TeV, which provides an interesting picture for the DM detection experiments.

- As we will discuss, ADM nuggets can be very large in size, which introduces the possibility of significant coherent enhancement. If the size of the ADM nugget is smaller than the inverse momentum transfer of the scattering event, the coherent enhancement will boost the scattering cross section. However, typically the experiments with the lower energy thresholds also have smaller exposure. Therefore this possibility of coherent enhancement introduces an interesting trade-off between lower threshold and higher exposure.

Drawing analogies from the SM baryons, we can initially think of ADM nuggets with ~ 100 constituents. However, there is no reason to think that the bottlenecks that prevent nuclei with more constituents also exist in the hidden sector. It is possible for the DM particles to interact with attractive forces only, which makes it possible to form much larger nuggets than SM nuclei. An ultra-large nugget with 10^3 to 10^{20} constituents means the N_χ^2 coherent enhancement can significantly boost the scattering cross section (The number of constituents 10^3 to 10^{20} was motivated in Ref. [51]). The comparison of low threshold - low exposure and higher threshold - higher exposure experiments for ADM nugget detection is presented in Ch. 3.

In our discussion of the formation of ADM nuggets, we will follow Refs. [51–53]. In this section, we denote the DM particles with χ. The properties of the constituents are denoted

by lowercase letters (like m_χ) whereas the properties of nuggets are denoted by uppercase letters (like M_χ.) First, we need to start with assumptions for the interaction between ADM constituents. We will assume no long-range repulsive force like SM electromagnetism exists in the hidden sector, so that the formation of ultra-large composite states is possible. And if we introduce a long-range attractive interaction, the relevant Lagrangian can be written as:

$$\mathcal{L} = \bar{\chi}\left[i\partial - (m_\chi - g_\phi\phi)\right]\chi + \frac{1}{2}(\partial\phi)^2 - \frac{1}{2}m_\phi^2\phi^2 - V(\phi)\ . \tag{2.86}$$

The above Lagrangian describes a Dirac fermion DM with a real scalar mediated interaction. The nuggets start efficiently forming when the Universe's temperature falls below the binding energy of the ADM nugget. Having the ADM framework set with constituents interacting attractively, the bulk nuclei-like properties of the nuggets like the saturation density and binding energy can be computed using the $\sigma - \omega$ and compound nucleus models from the nuclear physics [51–53]. By solving the Boltzmann equation numerically, Ref. [52] also obtains a distribution for the nugget sizes exiting synthesis. It was observed that if multiple states adjacent in size (for example, $N = 3, 4$) are unstable, a bottleneck is expected to occur. The results for the nugget size distribution for the cases with and without low N bottlenecks were shown in Fig. 2.11. For the benchmark couplings considered that allow the two-body fusion, the results show that in the absence of the bottleneck the mass regime most motivated is 10^3 GeV $\lesssim M_\chi \lesssim 10^{20}$ GeV. In the presence of a bottleneck, a bimodal mass distribution is observed where the nugget sizes are distributed between a dominant smaller-mass population and a subdominant larger-mass population.

When the nugget radius is larger than the de Broglie wavelength of the mediator, the nugget "saturates". Even though the properties of low N nuggets highly depend on the model considered, the saturated nuggets have their properties parametrized in two quantities, the (isolated) constituent mass m_χ, and the mass per constituent in the nugget (which is also called reduced constituent mass) $m_{\bar{\chi}}$. For example, two important quantities, the total nugget mass and the nugget radius can be written as:

$$\begin{aligned} M_\chi &= N_\chi \bar{m}_\chi + \epsilon_{\rm surf} N_\chi^{2/3}, \\ R_\chi &= \left(\frac{9\pi}{4}\frac{M_\chi}{\bar{m}_\chi^4}\right)^{1/3}, \end{aligned} \tag{2.87}$$

where $\epsilon_{\rm surf}$ denotes the surface energy density. In the absence of a bottleneck, the details of the nugget formation and synthesis are quite model independent, and can be stated as [51]:

$$N_\chi \simeq 10^{12}\left(\frac{g_*\left(T_{\rm syn}\right)}{10}\right)^{3/5}\left(\frac{1\ \text{GeV}}{\bar{m}_\chi}\right)^{12/5}\left(\frac{\bar{m}_\chi^3}{n_{\rm sat}}\right)^{4/5}\left(\frac{T_{\rm syn}}{\bar{m}_\chi}\right)^{9/5}. \tag{2.88}$$

The equation implies that the lower constituent masses result in larger nuggets, which is not surprising since lower constituent masses also imply lower saturation densities.

In this section we have briefly discussed the asymmetric dark matter nuggets by focusing on a real-scalar mediated interaction. A more detailed survey into the direct detection

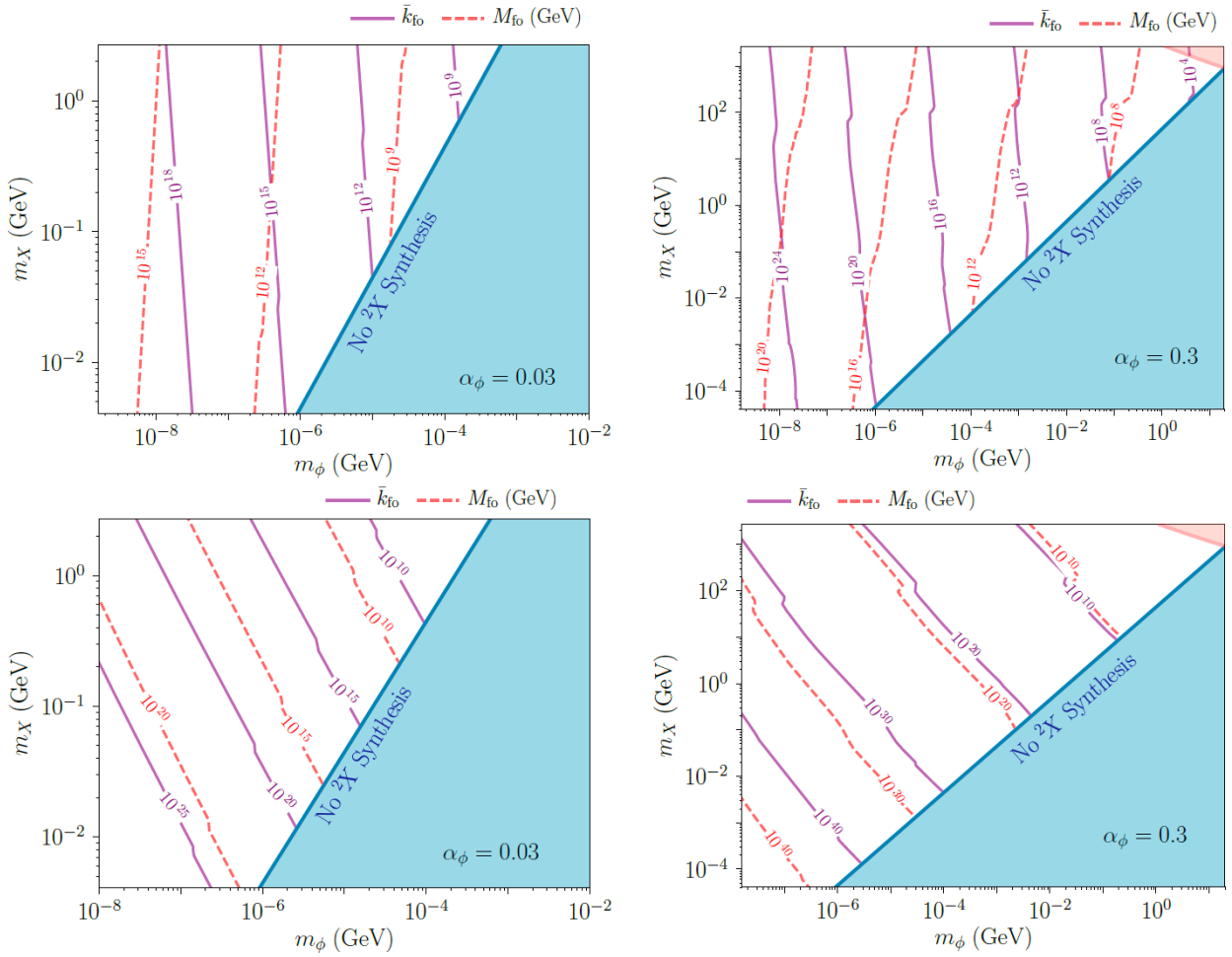

Figure 2.11: The top (bottom) row shows the results in the absence (presence) of the low N bottleneck. $k_{\rm fo}$ and $M_{\rm fo}$ stand for the nugget constituent number and the typical nugget mass respectively. The blue region corresponds to small binding energies that prevent the formation of two-body bound states, and therefore prevent the production of larger nuggets. Results are taken from Ref. [51].

prospects of asymmetrically produced dark nuggets, including the interactions mediated by scalars and vectors, is presented in Ch. 3.

Chapter 3

Direct Detection of Bound States of Asymmetric Dark Matter

3.1 Introduction

The last decade has seen a dramatic broadening in the types of Dark Matter (DM) theories that are being proposed and searched for using various experiments [25, 54]. Previously the Weakly Interacting Massive Particle (WIMP) and the axion were the focus of both theoretical and experimental attention, and for good reason: in addition to solving the DM mystery, they resolve another theoretical puzzle, the hierarchy problem and the strong CP problem, respectively. As the WIMP has not surfaced, the urgency to look elsewhere has increased. At the same time, a qualitative expansion of the number of DM candidates has occurred. Most of the new ideas have centered around *hidden sector* DM, where the dynamics of the non-Standard Model sector allow for a wider range of dark matter candidates and signatures.

Most of the work in hidden sector dark matter has focused on candidates of a low mass [55–60], as envisioned and proposed in the hidden valley model. This focus is partly phenomenologically motivated, but as thermal candidates with mass above 10 TeV cannot obtain the correct relic abundance through a standard thermal freeze-out scenario, there is also theoretical motivation. A natural question is what models of DM exist above this "unitarity bound" and how one searches for such candidates.

Here we consider the detection of very heavy composite bound states of Asymmetric Dark Matter (ADM). These states satisfy the unitarity bound because they are synthesized relatively late in the Universe from light constituents in a hidden sector. The symmetric component of the DM freezes out through annihilation to light force mediators in the hidden sector, as proposed in the original models [61, 62]. If the forces in the hidden sector are sufficiently strongly attractive and long range, the DM states will bind and grow into large states, as shown in [63–67]. When the states grow to a size such that the Fermi degeneracy pressure dominates the dynamics of the bound state, they "saturate" to a constant density [68, 69]; we call these states ADM nuggets. If the confining force in the dark sector undergoes

a first order phase transition, dark quark nuggets can form[70, 71], though in this chapter we focus on nuggets formed via fusion. Because the properties of ADM nuggets depend on very few parameters, such as the force range and strength and the constituent masses, and combined with the requirement that the states can form in the first place, the theory space is fairly predictive. It was found in [72] that the natural size of ADM nuggets, formed via early universe fusion, is $M_X \lesssim 10^{20}$ GeV, and that they give distinctive signatures in the structure of galaxies and can produce signatures in indirect detection [67, 72].

Due to their large size, the scattering of ADM nuggets in direct detection experiments can benefit from a significant N_X^2 coherent enhancement, with N_X the number of constituents in the nugget. The corresponding phenomenology was studied in [73, 74], where it was shown how the recoil spectrum of an ADM nugget can be distinguished from that of normal WIMP DM. The focus of this previous work was primarily on noble liquid and semi-conductor experiments, and in this chapter we aim to extend it by including more recent, lower threshold ideas for both electron and nucleon couplings. We furthermore consider both massive and light mediators, as well as a light, kinetically mixed dark photon mediator. Our motivation is that the N_X^2 enhancement only holds *as long the momentum transfer is low compared to the inverse radius of the nugget*, which correlates strongly with the experimental threshold. This effect was recently exploited for the largest composite objects, $M_X \gtrsim 10^{20}$ GeV, whose interaction cross-section is dominated by the object's geometric size, in the context in particular of gravitational wave detectors and spin precession experiments [75]. Here we focus on the regime most motivated by synthesis considerations (in the absence of a bottleneck, see [72]), 10^3 GeV $\lesssim M_X \lesssim 10^{20}$ GeV, and show how the recent program towards ultra low threshold detectors can impact the nugget DM parameter space.

In particular, a number of experiments have been recently proposed that are sensitive to very low momentum transfers, both for DM coupling to nucleons (see e.g. [76–82]) as well as electrons (see e.g. [83–88]); some of these experiments are also sensitive to interactions via dark photons. Due to the increased sensitivity via the coherent enhancement, these experiments are natural places to look when searching for ADM nuggets. However, these novel experiments are very small in volume compared to the large noble liquid detectors used in classic WIMP searches. Our goal is to quantify the relative reach of low threshold experiments compared to the classic WIMP-like searches. We will show that the relative sensitivity at a given nugget mass depends strongly on the constituent mass, which (largely) fixes the nugget radius. For lower constituent masses, where the nugget saturation densities are lower and their size is larger, the low threshold experiments dominate; for larger constituent masses, the opposite is true and the noble-liquid experiments provide better sensitivity. This result highlights the necessity of a multi-prong experimental approach to place constraints on ADM nuggets.

The outline of this chapter is as follows. In the Sec. 3.2 we review the model of composite dark matter we employ, and lay out our conventions and the main formulas for the direct detection of nuggets. We also review the relevant constraints from probes other than direct detection. In Secs. 3.3 and 3.4 we consider the direct detection prospects of ADM nuggets with couplings to nucleons and electrons respectively. We conclude in Sec. 3.5.

3.2 Composite Asymmetric Dark Matter

The goal of this section is to give a brief review of ADM nugget properties and their formation history. This allows us to select a natural model space for direct detection, as well as define our conventions for the direct detection parameter space. We also discuss the relevant constraints on the particle mediating the scattering with the Standard Model (SM), from probes other than direct detection.

Model and formation history

In the absence of a bottleneck, such as provided by electromagnetism in the SM, fermionic DM with a sufficiently attractive and long-range force can be synthesized with as many as $\sim 10^{20}$ constituents. We refer the reader to [72] for a review of nugget synthesis and properties. A generic Lagrangian to describe the properties of bound states of the fermions is given by

$$\mathcal{L} = \bar{\chi}(i\partial\!\!\!/ - m_\chi)\chi - \frac{1}{2}m_\varphi^2\varphi^2 + \frac{1}{2}m_V^2 V_\mu^2 - \bar{\chi}\left[g_\varphi\varphi + g_V V\!\!\!/\right]\chi - V(\varphi, a, V, A)\,, \tag{3.1}$$

where χ are the constituent fermions of the bound state and for compactness we have omitted the kinetic terms of the scalar, φ, and vector, V, mediators. Such a weakly coupled model (with φ relabeled as the σ and V relabeled as the ω) is employed in nuclear physics to describe the gross features of the underlying strong dynamics.

To determine the reach of direct detection experiments, we need to parametrize the properties of the nuggets. The properties of nuggets with only a few constituents are quite model-dependent. However, once the nugget radius exceeds the de Broglie wavelength of the force mediator, the nugget enters a constant density regime called saturation. Here, it can be shown that all the nugget properties can be parameterized in terms of just two quantities [69, 72] – the constituent mass m_χ and the reduced constituent mass $\overline{m}_\chi$, with the latter taking into account the in-medium effects of the nugget on the constituent mass. For example, the radius of a bound state of N_X constituents,

$$R_X = \left(\frac{N_X}{4/3\pi n_{\rm sat}}\right)^{1/3}, \tag{3.2}$$

is determined by the saturation density $n_{\rm sat}$. This quantity is in turn is set by $\overline{m}_\chi$:

$$\frac{n_{\rm sat}}{\overline{m}_\chi^3} = \begin{cases} \frac{1}{3\pi^2} & \frac{C_V^4}{C_\varphi^2} \le \frac{1}{8} \\ \frac{1}{3\pi^2}\left[\frac{1}{2} + \left(\frac{C_V^4}{C_\varphi^2}\right)^{\frac{1}{3}}\right]^{-3} & \frac{C_V^4}{C_\varphi^2} > \frac{1}{8} \end{cases} \qquad \frac{\overline{m}_\chi}{m_\chi} = \begin{cases} \left(\frac{2}{C_\varphi^2}\right)^{\frac{1}{4}} & \frac{C_V^4}{C_\varphi^2} \le \frac{1}{8} \\ \frac{1}{(C_\varphi C_V)^{\frac{1}{3}}}\left[\frac{1}{2} + \left(\frac{C_V^4}{C_\varphi^2}\right)^{\frac{1}{3}}\right] & \frac{C_V^4}{C_\varphi^2} > \frac{1}{8} \end{cases} \tag{3.3}$$

where

$$C_V^2 \equiv \frac{g_V^2}{3\pi^2}\frac{m_\chi^2}{m_V^2} \qquad \text{and} \qquad C_\varphi^2 \equiv \frac{g_\varphi^2}{3\pi^2}\frac{m_\chi^2}{m_\varphi^2}\left[1+\frac{2g_\varphi^2 V(m_\chi/g_\varphi)}{m_\varphi^2 m_\chi^2}\right]^{-1}. \tag{3.4}$$

In order for the bound states to reach saturation, neither m_φ or m_V can be too small, i.e, it must be that both m_ϕ and m_V must be larger than R_X^{-1}. Thus we see that m_χ and $\overline{m}_\chi$ tend not to be widely separated.

The total nugget mass is

$$M_X = N_X \overline{m}_\chi + \epsilon_{\rm surf} N_X^{2/3}, \tag{3.5}$$

where $\epsilon_{\rm surf}$ is the surface energy density. In a general model with both attractive and repulsive forces, $\epsilon_{\rm surf}$ is typically within an $O(1)$ number of $\overline{m}_\chi$ and hence is a negligible contribution to the total mass for large nuggets (see Refs. [69, 72] for a discussion and calculations).

For our purposes, we choose $M_X = N_X \overline{m}_\chi$ and $n_{\rm sat} = \bar{m}_\chi^3/(3\pi^2)$ to illustrate the reach of direct detection experiments. All our results will be parametrized in terms of M_X and $\overline{m}_\chi$ with the radius of the nugget in Eq. (3.2) written in terms of these variables,

$$R_X = \left(\frac{9\pi}{4}\frac{M_X}{\bar{m}_\chi^4}\right)^{1/3}. \tag{3.6}$$

Note that throughout this chapter we use a convention where the index χ is used as a constituent label, while X refers to the bound state of χ's.

A natural question to ask is the typical size of nuggets that are synthesized via early universe fusion. While the size of synthesized states is in general model-dependent, large nuggets that constitute a significant fraction of the DM energy density are most naturally synthesized in the absence of a bottleneck to formation. In this case, the dynamics of synthesis are quite model-independent, determined only by the Hubble parameter and the geometric cross section of the nugget. One finds the synthesized size to be [72]

$$N_X \simeq 10^{12}\left(\frac{g_*(T_{\rm syn})}{10}\right)^{3/5}\left(\frac{1\ \text{GeV}}{\overline{m}_\chi}\right)^{12/5}\left(\frac{\bar{m}_\chi^3}{n_{\rm sat}}\right)^{4/5}\left(\frac{T_{\rm syn}}{\overline{m}_\chi}\right)^{9/5}. \tag{3.7}$$

Thus we see that lower constituent masses tend to give rise to larger nuggets. The reason for this can be seen in Eq. (3.3): nuggets with low constituent masses tend to have lower saturation densities, and hence larger sizes, implying that freeze-out of the synthesis process happens later. As we will see in the next section, however, self-interaction constraints tend to favor smaller interaction cross sections, implying that nuggets typically are not too large if they compose all the dark matter. Furthermore, if there is an additional mediator, either scalar or vector, whose de Broglie wavelength exceeds the radius of the nugget, its couplings must be extremely small in order to not affect the formation history and structure of ADM nuggets. In this work we will however take the nugget mass as a free parameter, with all nuggets having the same mass for simplicity. We leave the interplay between the nugget mass distribution, as predicted from the formation history, and the direct detection bounds for future studies.

Constraints on the mediator

We assume that the Dark Sector interacts with the Standard Model via a mediator[1], ϕ, which couples either to nucleons or electrons,

$$\mathcal{L} \supset \tfrac{1}{2} m_\phi^2 \phi^2 + g_\chi \phi\, \bar{\chi}\chi + g_n \phi\, \bar{n} n + g_e \phi\, \bar{e} e \ . \tag{3.8}$$

where n here stands for nucleons and e for electrons. The mass of the mediator, m_ϕ, can either be large or small, compared to the typical momentum transfer in direct detection experiments. In our analysis, we will always consider g_n or g_e separately, in Secs. 3.3 and 3.4 respectively. We will discuss these types of constraints in the rest of this subsection.

Mediator Interactions with Standard Model

The constraints on the coupling of the mediator to the Standard Model are highly dependent on the mediator mass, and we only consider a few benchmark scenarios, corresponding to the heavy and light mediator scenarios.

For a heavy mediator with a coupling to nucleons, the collider constraints depend on the UV completion of the $g_n \phi\, \bar{n} n$ coupling. We consider the

$$\mathcal{L} \supset \frac{\alpha_s}{4\Lambda} \phi G^a G^a \tag{3.9}$$

operator, where we fix $\Lambda = 2$ TeV. Λ is approximately the scale where Eq. (3.9) in turn must be UV completed, and its value is taken such that the UV completion can plausibly be outside the reach of the LHC, depending on the details of the model. Following [89], we then map this coupling to the effective nucleon coupling $g_n = \frac{2\pi}{9}\frac{m_n}{\Lambda} \approx 3.4 \times 10^{-4}$ and choose $m_\phi = 10$ GeV and $g_\chi = 1$. The mediator ϕ will then decay invisibly if $2m_\chi < m_\phi$, and to a pair of soft jets otherwise. The collider limits in these cases are extremely weak or non-existing respectively (see e.g. [90, 91]), and do not constrain the model for our choice of Λ. For the above parameter choices we can then estimate an upper bound on the nugget direct detection cross section of

$$\sigma_{Xn} \approx N_X^2 \frac{g_\chi^2 g_n^2}{4\pi} \frac{\mu_{Xn}^2}{m_\phi^4} \lesssim 3 \times 10^{-34} \times \left(\frac{N_X}{10^3}\right)^2 \times \mathrm{cm}^2 \tag{3.10}$$

with $\mu_{nX} \approx m_n$ the nugget-nucleon reduced mass. It is possible to further relax this constraint by considering a scenario where ϕ has $\mathcal{O}(10^{-1})$ couplings to the up and/or down quark, though this requires a relatively complex flavor model.

For a heavy mediator coupling to electrons, we take $m_\phi = 25$ MeV and $g_e = 10^{-4}$. This benchmark point is allowed by the current the $(g-2)_e$ and SLAC beam dump bounds [92], as well as the Babar bound [93, 94] and the projections for Belle II [95], both if ϕ decays visibly

[1]The mediator ϕ, responsible for the interactions with the SM, is in general not the same field as the mediator which binds the ADM nugget in Eq. (3.1), denoted by φ.

and invisibly. For $2m_\chi < m_\phi$ the mediator can decay to the dark matter, in which case the LSND bound considered in [96] applies. With the parameter choices above, it suffices to take $g_\chi = 10^{-1}$ to evade this constraint. For these choices, the direct detection cross section is roughly

$$\sigma_{Xe} \approx N_X^2 \frac{g_\chi^2 g_e^2}{4\pi} \frac{\mu_{Xe}^2}{m_\phi^4} \lesssim 2 \times 10^{-33} \times \left(\frac{N_X}{10^3}\right)^2 \times \mathrm{cm}^2. \tag{3.11}$$

We will see in Secs. 3.3 and 3.4 that this bound is largely irrelevant compared to the direct detection constraints, especially for $N_X \gg 1$.

For mediators with eV-scale masses, the most stringent constraints arise from astrophysical considerations, such as stellar cooling constraints. For even lighter mediators, constraints from fifth force and weak equivalence principle violation tests become more important. The constraints on light mediators in the mass range of an eV to a GeV are summarized in e.g. [97]. In this work, we do not scan over mediator masses, but instead choose a benchmark of $m_\phi = 1$ eV to illustrate the feasibility of detecting ADM nuggets via this portal. Stellar cooling constrains $g_n \lesssim 10^{-12}$ and $g_e \lesssim 10^{-15}$ for this mass [98]. Sec. 3.4 we will also briefly consider a dark photon mediator. The stellar bounds on the mixing parameter κ with the SM photon is roughly $\kappa \lesssim 10^{-12} \times \left(\frac{\mathrm{eV}}{m_{A'}}\right)$, with $m_{A'}$ the dark photon mass [99].

It is worth noting that once the stellar cooling constraints are satisfied, the mediator does not thermalize with the SM in the early universe [97]. The mediator is however in thermal contact with the ADM nuggets, and its relic abundance therefore depends on the details of the thermal history of the dark sector. In this work we aim to be as agnostic as possible about this aspect, but it would be interesting to explore possible CMB and/or BBN bounds in the context of a concrete formation history for the ADM nuggets.

Mediator Interactions with Dark Sector

The coupling of the mediator to the dark sector is constrained by DM self-interactions, both in the early universe and in the collisions of galaxy clusters, and by the properties of the bound states in the presence of an additional long-range mediator.

Self-interaction constraints tend to be quite stringent, as the DM-DM cross section is enhanced by the N_X^2 coherence factor. For a heavy (short range) mediator, we can assume that the DM-DM cross section is saturated to the geometric cross section. Since the short range force which binds the ADM nugget also contributes to DM-DM scattering, this remains true regardless of the strength of the DM-SM mediator. The bound is then

$$\sigma_{XX}^{\mathrm{geo}} = 4\pi R_X^2 \lesssim 1\,\mathrm{cm}^2 \times \frac{M_X}{\mathrm{g}}, \tag{3.12}$$

where the cross-section is chosen to be consistent with DM dynamics in the Bullet Cluster [100, 101]. This can be written as a lower bound on M_X using the relation in Eq. (3.6)

$$M_X \gtrsim 4 \times 10^{14}\,\mathrm{GeV} \times \left(\frac{\mathrm{MeV}}{\overline{m}_\chi}\right)^8. \tag{3.13}$$

This extreme sensitivity to $\bar{m}_\chi$ implies that no self-interaction bound exists for $\bar{m}_\chi \gtrsim 100$ MeV.

In the case of a light mediator, the cross section receives a contribution from the corresponding long range interaction, in addition to the purely geometric contribution that arises from the short range force that binds the ADM nugget. The range of the interaction is therefore larger than the radius of the ADM nugget, but the scattering is biased towards small angles. Therefore, the cross section of interest is the momentum transfer cross section, σ_T [102, 103], which can be approximated in terms of the classical "point of closest approach" d_C,

$$\sigma_T^{\text{light}} \sim 4\pi\, d_C^2 \sim \frac{4\pi}{m_\phi^2} \mathrm{W}\left[\frac{4\alpha_X m_\phi}{M_X v_{\text{rel}}^2}\right]^2 \lesssim 1\,\text{cm}^2 \times \frac{M_X}{\text{g}} \qquad \alpha_X \equiv N_X^2 \frac{g_\chi^2}{4\pi} \tag{3.14}$$

where W is the Lambert W function. The inequality again represents the Bullet Cluster constraint. The self-interaction bound for a light mediator is then

$$g_\chi \lesssim \left(\frac{\pi}{4}\frac{\bar{m}_\chi^4 v_{rel}^4}{M_X} \times \frac{1\,\text{cm}^2}{g}\right)^{1/4} e^{\frac{1}{4}\sqrt{\frac{m_\phi^2 M_X}{\pi} \times \frac{1\,\text{cm}^2}{g}}}. \tag{3.15}$$

The exponential term indicates that the bound quickly becomes negligible when the range of the mediator becomes small compared to the Bullet Cluster bound on the scattering length. This occurs for

$$M_X \gtrsim 10^{16}\,\text{GeV}\left(\frac{\text{eV}}{m_\phi}\right)^2. \tag{3.16}$$

In this regime the light mediator ϕ does not contribute to the SIDM bound, though the constraint in Eq. (3.13) still applies, due to the short range DM-DM force that binds the constituents of the ADM nugget.

The bounds in Eqs. (3.13) and (3.16) do not apply if the nuggets make up less than roughly 10% of the dark matter. Given the relative complexity of the dark sector and the non-trivial formation history, this is rather plausible, in particular if there are bottlenecks in the dark fusion processes [69]. To illustrate the variation in the direct detection phenomenology, we will consider a benchmark with $\bar{m}_\chi = 10$ MeV, which is excluded by self-interaction bounds for $M_X \lesssim 4 \times 10^6$ GeV if all of the DM is made up out of a nugget of a single mass. For this benchmark we therefore assume that the ADM nuggets we consider for direct detection compose 1% of the total DM density. All direct detection limits can be trivially rescaled to the desired subcomponent fraction, including 100%, in the large M_X part of the parameter space.

While the SIDM constraints do not apply for subcomponent DM, there are additional consistency conditions on g_χ which must be satisfied even in a subcomponent scenario: for example, the potential for a light scalar mediator will be modified due to the presence of the background charge density sourced by the nugget constituents. In particular, one expects

the mass of a light field to receive an in-medium correction of the order $\delta m_\phi^2 \sim \frac{g_\chi^2}{\bar{m}_\chi}\langle\overline{\chi}\chi\rangle$ with $\langle\overline{\chi}\chi\rangle \sim \bar{m}_\chi^3$ from the background χ-field in the nugget. If this correction reduces the range of the mediator inside the nugget to be comparable or smaller than the radius of the nugget itself ($\delta m_\phi^{-1} \gtrsim R_X$), the scattering cross section is dramatically altered[2]. To avoid this, we require

$$g_\chi \lesssim N_X^{-1/3}\,. \tag{3.17}$$

When the coupling becomes larger than this, the in-medium screening effects will alter the experimental reach, including its dependence on M_X, and so we will limit ourselves to regions of parameter space where Eq. (3.17) is satisfied. If one instead assumes a repulsive interaction instead of an attractive one, the ADM nugget becomes unbound unless, again, $g_\chi \lesssim N_X^{-1/3}$.

Finally, in Sec. 3.4 we will briefly consider the special case of a light, kinetically mixed dark photon acting as the mediator. In this case the interaction is repulsive and it may be difficult for large ADM nuggets to form, due to a Coulomb-like barrier sourced by the dark photon. In order for ADM nuggets to undergo fusion in the early universe, they must have enough kinetic energy to overcome this repulsive barrier, i.e.

$$\frac{\mu_{X_1X_2}v^2}{2} \gtrsim g_\chi^2\frac{N_{X_1}N_{X_2}}{R_{X_1}+R_{X_2}} \tag{3.18}$$

where $\mu_{X_1X_2}$ is the reduced mass of the two nuggets and we have allowed for the possibility that fusion occurs between nuggets of different sizes. Assuming fusion occurs either between nuggets of the same size or between a nugget and a single constituent, the barrier can be overcome if

$$g_\chi \lesssim \begin{cases} N_X^{-5/6} & \text{Two identical nuggets} \\ N_X^{-1/3} & \text{Constituent and a nugget} \end{cases}\,. \tag{3.19}$$

One might wonder whether instead of overcoming the barrier classically, it would be possible to have fusion occur via quantum mechanical tunneling through the barrier. In this case, the constraint on g_χ involves calculating the Gamow factor and requiring that the transmission probability is a sizable fraction of unity. The corresponding constraint on the coupling is

$$g_\chi \lesssim \begin{cases} N_X^{-5/4} & \text{Two identical nuggets} \\ N_X^{-1/2} & \text{Constituent and a nugget} \end{cases} \tag{3.20}$$

where in Eqs. (3.19)-(3.20), we assume that the fusion occurs in a thermal bath whose temperature is on the same order as $\bar{m}_\chi$. For scattering in this type of environment, fusion due to quantum mechanical penetration of the barrier is negligible until the barrier can be overcome classically. Therefore, we take Eq. (3.19) as indirect constraints on g_χ when considering dark photons. While model specific contributions can change the prefactors in Eq. (3.17) and Eq. (3.19), the scaling as a function of N_X will remain.

[2]This is akin to the Debye screening mass that a photon develops in a charged plasma.

Direct detection of composite Dark Matter

For a heavy mediator, the potential seen by a point-like DM particle is simply the sum of the potential for each of the scattering centers in the target. The part of the Hamiltonian governing this contact interaction is

$$\mathcal{V}(\mathbf{r}) = \sum_{J=1}^{N} \mathcal{V}_J(\mathbf{r}_J - \mathbf{r}) = \frac{2\pi b_{Xt}}{\mu_{Xt}} \sum_{J=1}^{N} \delta(\mathbf{r}_J - \mathbf{r}) \tag{3.21}$$

or in Fourier space

$$\mathcal{V}(\mathbf{q}) = \frac{2\pi b_{Xt}}{\mu_{Xt}} \sum_{J}^{N} e^{i\mathbf{q}\cdot\mathbf{r}_J}. \tag{3.22}$$

where J sums over all scattering centers with location $\mathbf{r}_J$, μ_{Xt} is the reduced mass of the DM and the SM target particle,[3] which we take to be a nucleon or an electron; we will generalize to nuclei in the next section. The DM-target scattering length is b_{Xt}, again defined as either the DM-nucleon or DM-electron scattering length, depending on the model and process under consideration. For simplicity we have assumed a single type of scattering center in the target, by pulling the b_{Xt}/μ_{Xt} factor in front of the sum; the generalization to multiple types of scattering centers is straightforward and will be included when appropriate (*e.g.* for a GaAs target). The potential is normalized such that the cross section for a probe on a single, free scattering center is

$$\overline{\sigma}_0 \equiv 4\pi b_{Xt}^2. \tag{3.23}$$

In other words, $\overline{\sigma}_0$ is the cross section for the scattering of a hypothetical DM nugget with radius zero off a SM nucleon or electron. Since this quantity is the analogue to the familiar DM-nucleon/DM-electron cross section for elementary DM, we will therefore use it to parametrize the constraints. In particular for DM that couples to nucleons, $\overline{\sigma}_0$ is defined as the cross section off a single, free nucleon, to allow for convenient comparison between targets with different atomic mass numbers.

Given that we will be comparing a variety of different target materials, it is helpful to explicitly separate the DM kinematics from the properties of the target by defining the structure function of the target by

$$S(\mathbf{q},\omega) \equiv \frac{1}{N} \sum_{f} \left| \sum_{J}^{N} \langle \lambda_f | e^{i\mathbf{q}\cdot\mathbf{r}_J} | \lambda_i \rangle \right|^2 \delta(E_f - E_i - \omega) \tag{3.24}$$

which is normalized to be an intrinsic quantity. The $\langle \lambda_{i,f}|$ are the initial and final states of the target, and the $E_{i,f}$ their corresponding energies; $\mathbf{q}$ and ω are respectively the momentum

[3] Throughout, we use the convection that lowercase letters indicate constituents and capital letters indicate the bound states. E.g. m_n and m_N refer to the nucleon mass and nucleus mass respectively.

transfer and the energy deposited by the DM. The states $\langle\lambda_{i,f}|$, and therefore the function $S(q,\omega)$, are highly material dependent and must be computed on a case-by-case basis. In general, $S(\mathbf{q},\omega)$ depends on the direction of $\mathbf{q}$, in particular for long-wavelength scattering in anisotropic crystals. However in this chapter we will always work in the isotropic approximation, where $S(\mathbf{q},\omega)$ only depends on $q \equiv |\mathbf{q}|$ and ω. It is worth noting that this prescription is correct only as long as the Born approximation is valid, i.e. as long as the total cross section remains smaller than the geometric cross section. This condition is violated in part of the parameter space, as we will comment on when appropriate.

By Fermi's golden rule, the differential cross section of a point-like probe with the target is then

$$\frac{d\overline{\sigma}}{dq\,d\omega} = \overline{\sigma}_0 \frac{q}{2v^2\mu_{Xt}^2} |F_{\rm med}(q)|^2\, S(q,\omega), \tag{3.25}$$

where v is the DM velocity in the lab frame. We have included the form factor induced by the mediator particle, which we take to be

$$F_{\rm med}(q) = \begin{cases} 1 & \text{(heavy mediator)} \\ q_0^2/q^2 & \text{(light mediator)} \end{cases}, \tag{3.26}$$

where q_0 is a reference momentum transfer. The typical momentum transfer is often proportional to μ_{Xt}, which depends on the target. We will not study the intermediate regime, where the mediator being heavy or light varies from experiment to experiment – we will assume that the mediator mass is such that either the heavy or light case applies for all experiments shown in a given plot. In terms of the underlying model parameters $\overline{\sigma}_0$ is given by

$$\overline{\sigma}_0 = N_X^2 \frac{g_t^2 g_\chi^2}{4\pi} \times \begin{cases} \mu_{Xt}^2/m_\phi^4 & \text{(heavy mediator)} \\ \mu_{Xt}^2/q_0^4 & \text{(light mediator)} \end{cases} \tag{3.27}$$

with g_t standing for g_e or g_n, depending on the case at hand. The N_X^2 factor makes the coherence over the nugget constituents explicit. Finally, with Eq. (3.27) it becomes manifest that the physical cross section for a light mediator in Eq. (3.25) is independent of the arbitrary parameter q_0.

Moving on to the scattering of extended nuggets, we must introduce a form factor to account for the non-zero radius of the DM particle, as laid out in [73]. For elastic scattering with uniform couplings to all constituents, the form factor is given by the Fourier transform of the mass density, ρ_X,

$$F_X(\mathbf{q}) = \frac{1}{M_X} \int d^3\mathbf{r}\; e^{i\mathbf{q}\cdot\mathbf{r}} \rho_X(\mathbf{r}). \tag{3.28}$$

Further assuming that the constituents of nuggets are uniformly distributed, the mass density is simply a three dimensional spherical top hat function and thus the form factor is

$$F_X(q) = \frac{3j_1(qR_X)}{qR_X} = \frac{3(\sin(qR_X) - qR_X\cos(qR_X))}{(qR_X)^3} \tag{3.29}$$

where $j_1(x)$ is a spherical Bessel function of the first kind (see Fig.3.1). The differential scattering cross section of an ADM nugget can then be written as

$$\frac{d\sigma}{dq\, d\omega} = \frac{d\overline{\sigma}}{dq\, d\omega}|F_X(q)|^2 \tag{3.30}$$

where $d\overline{\sigma}/dq\, d\omega$ is the differential cross section of a point-like dark matter particle with the same mass and coupling strength as the ADM nugget, as defined in Eq. (3.25). We have normalized the form factor such that $F_X(0) = 1$, such that we manifestly recover the point-like limit if $qR_X \ll 1$. In this regime all constituents contribute coherently and the scattering rate scales with the square of the number of constituents, as is evident from Eq. (3.27). If the inverse momentum transfer is smaller than the radius but still larger than the interparticle spacing of the nugget, coherence is lost and the form factor drops rapidly. Finally, once the momentum transfer is larger than the inverse interparticle spacing, we enter the regime of deep inelastic scattering (DIS), and the form factor description breaks down. Given the relatively low speed of the DM in the galaxy, the maximum momentum transfer in a single collision is $\mathcal{O}(m_N\, v) \sim 100$ MeV, such that DIS is only relevant for $\overline{m}_\chi \ll 100$ MeV. If the interior of ADM nugget is resolved in the collisions, the rate moreover is always dominated by the lowest accessible momentum transfer, such that the DIS contributions are a negligible correction. The one exception occurs for high threshold, noble liquid experiments when $\overline{m}_\chi \lesssim 10$ MeV; here, the experimental threshold pushes the scattering into the crossover region between the form factor and DIS descriptions. When relevant, we will comment on this effect when presenting our results.

We can combine Eq. (3.24) and Eq. (3.30) to obtain the differential rate per unit of

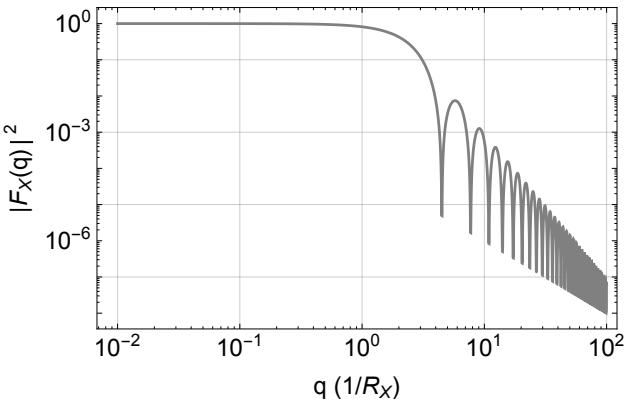

Figure 3.1: Nugget form factor, with q in units of $1/R_X$.

exposure, as seen by the experiments

$$\frac{dR}{d\omega} = \frac{\rho_X}{M_X}\frac{n_T}{\rho_T}\frac{\overline{\sigma}_0}{2\mu_{Xt}^2}\int dv\,\frac{1}{v}f(v)\int dq\,q\,|F_X(q)|^2\,|F_{\rm med}(q)|^2\,S(q,\omega) \tag{3.31}$$

with $\rho_X \approx 0.3$ GeV/cm^3 the DM mass density in the galaxy, ρ_T the mass density of the target material, and n_T the number of available scattering centers in the target. Here, $f(v)$ is the velocity distribution of the DM in the frame of the earth, given by

$$f(v) = \frac{1}{N_0}\frac{\pi v v_0^2}{v_e}\times\begin{cases} e^{-(v+v_e)^2/v_0^2}\left(e^{4v\,v_e/v_0^2}-1\right) & v < v_{esc}-v_e \\ e^{-(v-v_e)^2/v_0^2} - e^{v_{esc}^2/v_0^2} & v_{esc}-v_e < v < v_{esc}+v_e \\ 0 & v > v_{esc}+v_e \end{cases}, \tag{3.32}$$

$$N_0 \equiv \pi^{3/2}v_0^3\left[\mathrm{erf}(\tfrac{v_{\rm esc}}{v_0}) - \tfrac{2}{\sqrt{\pi}}\tfrac{v_{\rm esc}}{v_0}\exp\left(-(\tfrac{v_{\rm esc}}{v_0})^2\right)\right], \tag{3.33}$$

with $v_0 = 220$ km/s, $v_e = 240$ km/s, truncated by the escape velocity $v_{\rm esc} = 550$ km/s.

Energy and momentum conservation enforce target-dependent boundary conditions on the q-integral, depending on whether the DM scatters with a nucleus, a phonon or a bound electron. Finally, different detectors are sensitive to different energy ranges, which in turn restricts the integration range over ω. We will elaborate on all these differences and their impact in the following sections, but it should be already clear from Fig. 3.1 that in particular the boundary conditions on $|\mathbf{q}|$ will have a huge impact on the rate: if the threshold of a particular experiment is too high to allow for coherent scattering, its reach will be greatly reduced.

3.3 Nucleon couplings

In this section we consider the case where the nuggets have a coupling to SM nucleons only. The nucleon couplings give rise to a nuclear recoil, or in the case that the momentum transfer is smaller than the inter-atom spacing, coherent phonon excitations. As was shown in Refs. [68, 69, 72], there is enormous variation in dark nugget formation histories and resulting size. For this reason, it does not seem warranted at this point to carefully recast all existing limits on elementary dark matter to the composite case. Instead we consider a handful of simplified experimental concepts which are representative of the larger set of experiments and ideas for (future) dark matter direct detection, as listed in Table 3.1.

In particular, we compare high threshold, high exposure noble liquid experiments with low threshold, low exposure experiments such as semi-conductor or superfluid helium targets. (For a recent overview, see [25].) For nuggets on the higher end of the mass range, as we will see, only the low threshold experiments benefit from the coherent enhancement over nucleon number, such that they can be competitive despite their much lower exposure. This implies a high degree of complementarity between both approaches, which we quantify below. The calculations are qualitatively different depending on whether the scattering takes place in

Experiment	Exposure (kg-year)	Threshold	Timescale	N_{events}
XENON1T [104]	10^3	5 keV	existing limit	3
CDMSlite [105]	0.2	0.5 keV	existing limit	BD
Liquid Xe	1.5×10^4	5 keV	in progress	10
semi-conductor (Ge)	100	50 eV	in progress	10^4
semi-conductor (Si)	1	10 meV	R&D needed	3
superfluid He (recoil)	1	1 meV	R&D needed	3
superfluid He (phonon)	1	1 meV	R&D needed	3
GaAs (phonon)	1	1 meV	R&D needed	3

Table 3.1: Overview of assumed exposure and thresholds for the existing and future experiments considered in this work, for DM-nucleon couplings. N_{events} refers to the number of expected signal events that were assumed to estimate the 90% exclusion limits, where "BD" refers to a bin dependent analysis. (See text for details.)

the nuclear recoil regime, or in the regime where direct phonon production dominates and so we treat both cases separately.

Nuclear recoils

For ordinary nuclear recoils, the structure function in Eq. (3.31) is

$$S(q,\omega) = A^2 |F_N(q)|^2 \delta\left(\omega - \frac{q^2}{2m_N}\right), \tag{3.34}$$

with A the atomic mass number of the nucleus and m_N the mass of the nucleus. $F_N(q)$ is the Helm form factor of the nucleus

$$F_N(q) \equiv \frac{3j_1(qR_N)}{qR_N} e^{-q^2 s^2/2}, \tag{3.35}$$

with skin depth $s \simeq 0.9$ fm and $R_N \approx A^{1/3} \times 1.2$ fm. We have assumed that the scattering length is the same for protons and neutrons.

We take XENON1T [104] as a representative for the existing limits from the large exposure experiments;[4] PandaX-II [109] and LUX [110] have set very similar bounds. XENON1T

[4]The kinematic restriction in Eq. (3.34) is lifted if the nucleus emits a photon during its recoil [106], or by emitting a Migdal electron [107]. For light DM these processes add sensitivity for detectors of which the threshold would normally be too high to detect the regular nuclear recoil, as is evident from a recent LUX analysis [108]. For ADM nuggets, one can verify that the bremsstrahlung process never provides more reach than nuclear recoils, regardless of R_X. The recast of the Migdal effect is more involved, and we leave this for future studies.

reaches its maximal signal efficiency for $10\,\text{keV} \lesssim E \lesssim 45$ keV, but is partially efficient for substantially lower/higher recoil energies. To model this effect, we use the full efficiency curve supplied in [111] in our calculations. For our approximate reinterpretation, we use the "reference region" defined in [111], which contains roughly 50% of the signal and an expected background of 0.36 events. No events were observed and so we take 3 signal events in this region as our approximate limit. We consider CDMSlite [105] as an example of an existing, low-threshold experiment with a semi-conductor target. (Other experiments with competitive results on low-threshold nuclear recoils are CRESST-II [112] and NEWS-G [113].) CDMSlite had an exposure of 70 kg-days in their second run, with a threshold of roughly 0.5 keV and a maximal signal efficiency leveling around 50%. We use the full efficiency curve provided by the collaboration, which we unfold to nuclear recoil energies using the Lindhard formula with the parameters given in [105]. The analysis had a large number of background events, divided over four non-overlapping energy bins. For each bin, we extract a limit on the cross section assuming that all background events can be interpreted as signal, and select the strongest such limit for each mass point. This procedure reproduces the CDMSlite limit to within 50% for DM masses above roughly 10 GeV. For the part of the phase space near the detector threshold the agreement is worse, however our estimate is always conservative.

Loosely modeled after LUX-ZEPLIN [114], we estimate the reach for future high exposure experiments by assuming a 15 ton-year exposure and a 5 keV (75 keV) lower (upper) energy threshold. We further assume a background expectation of 5 events in the signal region, which corresponds to an expected 90% exclusion of roughly 10 signal events if no background subtraction is attempted. For a future, low threshold semi-conductor experiment we consider a Ge target with 100 kg-year exposure, a threshold of 50 eV and 10^4 expected background events. These parameters are loosely modeled after the superCDMS [115] projections.

Lastly, we consider a few ultra-low threshold options, for which the R&D is still ongoing: A miniaturized silicon detector with transition edge sensor (TES) read-out, for which we take the dynamic range between 10 meV and 1 eV, and a long-term exposure of 1 kg-year, which may eventually be achieved by multiplexing the detector. In the same vein, we include a superfluid helium target in nuclear recoil mode [79, 116, 117] with a dynamic range between 1 meV and 100 meV; superfluid helium in the phonon mode will be discussed in the next section. For both concepts, we (optimistically) assume negligible irreducible background. At least for radiogenic backgrounds, this is expected to be true due to the suppressed background spectrum at low recoil energies (see e.g. [118]) and the relatively low exposure. It is moreover straightforward to approximately rescale our projections for different background assumptions. Other future proposals, which we do not discuss here, include searches for anomalous color centers [76, 78], magnetic bubble chambers [119] and excitations in molecular gases [120].

In the remainder of this section we will present a number of analytic, approximate formulae for the rate. This will allow us to understand the features present in the sensitivity curves and to make explicit where low threshold detectors can perform better than the standard noble liquid experiments. We make the following approximations: (i) we set the DM velocity distribution to a delta function centered at v_0, (ii) drop the form-factor for the SM nuclei

($F_N \approx 1$) and (iii) take $M_X \gg m_N$, such that the reduced mass $\mu_{XN} \approx m_N$. The ADM nugget form factor can further be expanded as

$$|F_X(qR_X)|^2 = \begin{cases} 1 + \mathcal{O}(q^2 R_X^2) & qR_X \ll 1 \\ \frac{9}{2(qR_X)^4} + \mathcal{O}\left(\frac{1}{q^6 R_X^6}\right) & qR_X \gg 1 \end{cases}, \tag{3.36}$$

where the expansion at large momentum transfer only holds when the form factor is integrated against a smoothly varying function of q.

With the assumptions outlined above, the maximum and minimum momentum transfer for nuclear scattering is

$$q_{\max} = 2m_N v_0 \text{ and } q_{\min} = \sqrt{2m_N E_{\text{thres}}}, \tag{3.37}$$

where E_{thres} is the experimental threshold. There are then three regions of the sensitivity curve that each have a different dependence on the ADM nugget mass, as shown in Fig. 3.2. They are:

- Region I: No form factor suppression, $q_{\max} R_X \lesssim 1$.

  The ADM nugget radius is always less than the inverse momentum transfer. The SM nucleus therefore cannot probe any of the finite size properties of the ADM nugget and the nugget behaves like a point-like particle for all available phase space, regardless of the threshold of the detector. For heavy DM, this property holds when

  $$\frac{\overline{m}_\chi}{18\pi}\left(\frac{\overline{m}_\chi}{m_N v_0}\right)^3 \gtrsim M_X. \tag{3.38}$$

- Region II: Partial form factor suppression, $q_{\max} R_X \gtrsim 1 \gtrsim q_{\min} R_X$.

  The ADM nugget radius is larger than the inverse momentum transfer for some of the accessible phase space, and the coherent enhancement only occurs for a fraction of the scattering phase space. For heavy DM, this partial form factor suppression occurs when

  $$\frac{\sqrt{2}\overline{m}_\chi}{9\pi}\left(\frac{\bar{m}_\chi^2}{m_N E_{\text{thres}}}\right)^{3/2} \gtrsim M_X \gtrsim \frac{\overline{m}_\chi}{18\pi}\left(\frac{\overline{m}_\chi}{m_N v_0}\right)^3. \tag{3.39}$$

- Region III: Complete form factor suppression, $q_{\min} R_X \gtrsim 1$.

  The ADM nugget radius is larger than the inverse momentum transfer even for the smallest detectable momentum transfer, and thus the SM nucleus can probe the finite size properties of the ADM nugget for all of the accessible phase space. This implies that the coherent enhancement never occurs. For heavy DM, this complete form factor suppression occurs when

  $$M_X \gtrsim \frac{\sqrt{2}\overline{m}_\chi}{9\pi}\left(\frac{\bar{m}_\chi^2}{m_N E_{\text{thres}}}\right)^{3/2}. \tag{3.40}$$

Due to the simplicity of dynamic structure function for nuclear recoil, the detector-specific rate can be well approximated by an analytic expression. As we seek to determine which detectors work best for various regions of the ADM nugget parameter space, we pull out the dependence of the rate on the atomic mass number A by substituting $m_N = A\, m_n$.

For a heavy mediator, the fiducial cross section for an ADM nugget with mass M_X and radius R_X, scattering off of a target nucleus is

$$\sigma_{NR}^{\text{heavy}} \approx \overline{\sigma}_0 \times \begin{cases} \frac{A^2 q_{\text{max}}^2}{4 v_0^2 m_n^2} = A^4 & \text{Region I} \\ \frac{9A^2}{8 R_X^2 v_0^2 m_n^2} & \text{Region II} \\ \frac{9A^2}{8 q_{\text{min}}^2 R_X^4 v_0^2 m_n^2} = \frac{9A}{16 E_{\text{thres}} R_X^4 v_0^2 m_n^3} & \text{Region III} \end{cases}, \tag{3.41}$$

where $\overline{\sigma}_0$ is the reference cross section for scattering off a single, free nucleon, as defined in Eq. (3.23). In all regions, the cross section receives an A^2 enhancement from the coherence over the SM nucleus. In region I, this is supplemented with an A^2 phase space enhancement for heavy target nuclei, while for region III the $1/q_{\text{min}}^2$ phase space suppression partially cancels the effect of the coherent enhancement over the SM nucleus.

The effect of the form factor on the reach of two hypothetical experiments with different thresholds is shown in Fig. (3.2), where we labeled the transitions between regions I, II and III. In both panels, the crossover between regions I and II indicates where the form factor starts to reduce the reach relative to the point-like DM case. The left hand panel shows that this transition occurs sooner for lower values of $\overline{m}_\chi$, which correspond to a larger nugget. In the right hand panel we see that the transition between regions I and II is independent of E_{thres}, as expected from Eq. (3.38).

The dependence of the cross section on the dark nugget radius in the three different regions can be explained by simple arguments. In region I, where the nugget behaves like a point particle, there is no dependence on R_X. In region III, where the form factor is nontrivial for the entirety of the phase space, the expansion in Eq. (3.36) dictates that the cross section will scale as $1/R_X^4$. Lastly, in the intermediate region II, where the form factor only affects high momentum transfer scattering, the cross section scales with $1/R_X^2$. This is because the largest momentum transfer that is unaffected by the form factor is roughly $1/R_X$, such that one can obtain an estimate for the cross section by substituting $q_{\text{max}} \to 1/R_X$ in the expression for region I.

For interactions between the ADM nuggets and SM nuclei via a light mediator, these conclusions change qualitatively: the additional form factor in Eq. (3.26) further weights the matrix element towards lower momentum transfer and favors low threshold experiments over their higher threshold counterparts. The approximate fiducial cross section in this case is

$$\sigma_{NR}^{\text{light}} \approx \overline{\sigma}_0 \times q_0^4 \times \begin{cases} \frac{A^2}{4 q_{\text{min}}^2 v_0^2 m_n^2} = \frac{A}{8 E_{\text{thres}} v_0^2 m_n^3} & \text{Region I \& II} \\ \frac{3A^2}{8 R_X^4 v_0^2 m_n^2 q_{\text{min}}^6} = \frac{3}{64 A R_X^4 v_0^2 m_n^5 E_{\text{thres}}^3} & \text{Region III} \end{cases}, \tag{3.42}$$

where $q_0 = v_0 m_n$ is an arbitrary reference momentum, to render the definition of $\overline{\sigma}_0$ in Eq. (3.27) IR finite. The cross section is even more biased towards the low momentum

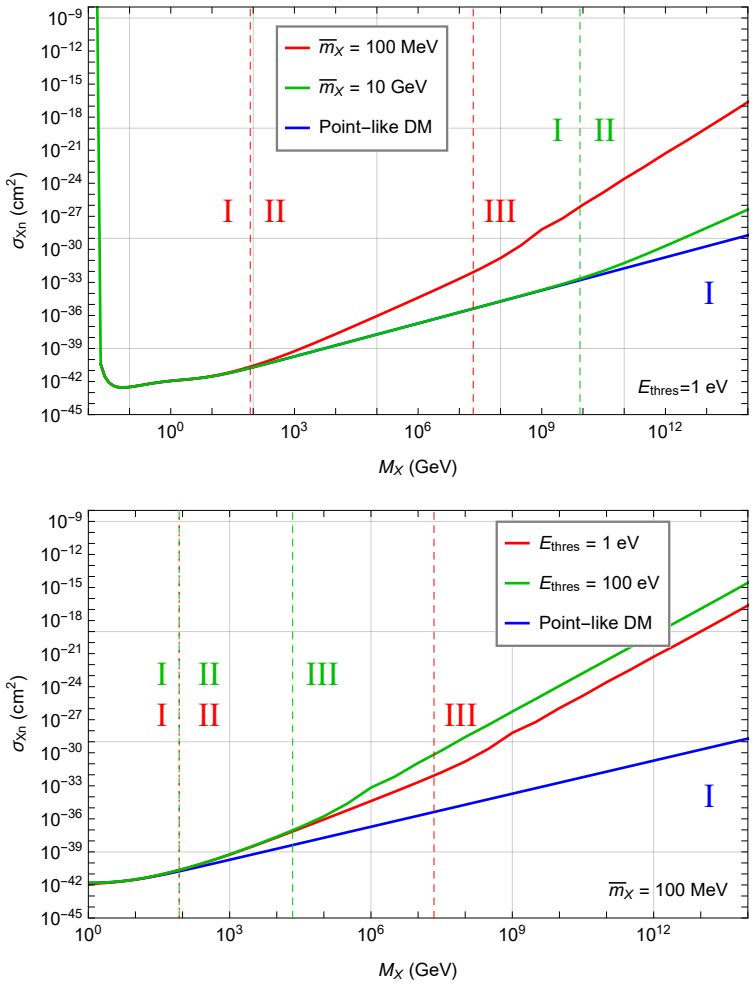

Figure 3.2: Example reach curves for nuggets and point-like DM particles for He target. **Top**: Fixed $E_{\rm thres} = 1$ eV, varying $\overline{m}_\chi$. **Bottom**: Fixed $\overline{m}_\chi = 100$ MeV, varying $E_{\rm thres}$. Roman numerals indicate the regions where the impact of the form factor differs qualitatively, as described in the text.

transfer regime, as is evident from the $q_{\rm min}$ factors in the denominator of both expressions. This implies that to leading order, there is no difference between regions I and II, since in both cases the process is still coherent near the low momentum threshold. The phase space distribution also changes the dependence on the atomic mass number A, making heavy nuclei detectors less favorable, as compared to the heavy mediator case in Eq. (3.41). For both Region I and Region II, where the dominant contribution to the scattering rate is unaffected by the form factor, there is no dependence on R_X. It is only in Region III, where the form

factor affects the entirety of the phase space, do we see a $1/R_X^4$ dependence that arises from the expansion of Eq. (3.36).

Collective Modes

When the inverse momentum transfer is larger than the inter-particle spacing, the response of the target is qualitatively different than what was considered in the previous section: the target can no longer be treated as a collection of non-interacting nuclei and instead one has to integrate out the atoms and use an effective description of a phonon gas at zero temperature. While scattering at such low momentum occurs for all types of dark matter, this contribution is typically heavily phase space suppressed for heavy dark matter. Large dark nuggets are an exception to this rule, as the coherent N_X^2 enhancement to the cross section at low momenta can overcome the phase space suppression in certain regions of the parameter space. A similar effect can occur when the scattering is due to a light mediator. Calculations of the single phonon production have been performed for the polar materials GaAs and sapphire [81, 82] and for two phonon/roton production in superfluid helium [79, 80].

For superfluid helium, we estimate the reach with the analytic expressions for the dynamic structure function in Refs. [79, 80] which match the simulation data [121] to within an order of magnitude. In particular, in the region where $|\mathbf{q}| \lesssim 1/\text{Å}$, the structure function can be approximated as

$$S(q,\omega) \approx \frac{q}{2m_{\rm He}c_s}\delta(\omega-\omega_q) + \frac{7m_{\rm He}^{5/2}}{60\pi^2\rho_0}\frac{c_s^4 q^4}{\omega^{7/2}} \tag{3.43}$$

where the first and second terms represent single and double phonon production respectively. However, for $q \lesssim$ keV and optimistic energy thresholds, the single phonon component is always too soft to contribute to the detection rate, as its energy is $\omega_q \approx c_s q$ where $c_s \approx 10^{-6}$ is the speed of sound in superfluid He. We therefore rely on double phonon production to detect ADM nuggets in superfluid helium when the momentum transfer is below the nuclear recoil threshold.

For scattering off phonon excitations in a crystal, the structure function is

$$S(\mathbf{q},\omega) = \frac{1}{2}\sum_\nu \frac{|F_\nu(\mathbf{q})|^2}{\omega_{\nu,\mathbf{q}}}\delta(\omega_{\nu,\mathbf{q}}-\omega) \tag{3.44}$$

with $F_\nu(\mathbf{q})$ and $\omega_{\nu,\mathbf{q}}$ are respectively the phonon form factor and energy corresponding to the phonon branch ν and momentum $\mathbf{q}$. We consider the example of GaAs, which has a cubic crystal structure with one gallium and one arsenic atom in its primitive cell, which give rise to 6 independent phonon modes. To leading order, only the longitudinal modes contribute with the form factor

$$|F_\pm(\mathbf{q})|^2 \approx \frac{q^2}{2}\left|\frac{A_{\rm Ga}}{\sqrt{m_{Ga}}}e^{i\mathbf{r}_{\rm Ga}\cdot\mathbf{q}} \pm \frac{A_{\rm As}}{\sqrt{m_{As}}}e^{i\mathbf{r}_{\rm As}\cdot\mathbf{q}}\right|^2 \tag{3.45}$$

where the + and − indicate the longitudinal acoustic (LA) and longitudinal optical (LO) mode, respectively. A_{Ga} and A_{As} are the atomic mass numbers for gallium and arsenic, while $\mathbf{r}_{Ga}$ and $\mathbf{r}_{As}$ are the locations of the gallium and arsenic atom with respect to the origin of the primitive cell. For a rough estimate, one can take $\mathbf{r}_{\rm Ga,As}\cdot\mathbf{q} \approx 0$. The LO mode has energy $\omega_{\rm LO} \approx 30$ meV, which is to good approximation momentum independent. For $q \lesssim 1$ keV, the LA mode has a linear dispersion relation $\omega_{\rm LA} = c_s q$ with the sound speed $c_s \approx 2\times 10^{-5}$. We refer to [82] for details on the derivation of Eq. (3.45).

Identical to the nuclear recoil case in the previous section, there are three qualitatively different regimes in the parameter space, set by the hierarchy between $q_{\rm min}$, $q_{\rm max}$ and $1/R_X$. The main difference is that for phonon modes $q_{\rm min}$ can be substantially lower than for nuclear recoil, thus enlarging the region of parameter space where coherence over the ADM nugget is possible (region I). We illustrate this for the case of the LA phonon in GaAs with simplified expressions for the fiducial cross section. The analogous expressions for the LO mode and helium can be easily derived. For the LA mode,

$$q_{\rm min} = E_{\rm thres}/c_s, \qquad q_{\rm max} = q_c \tag{3.46}$$

with $q_c \approx 1$ keV the momentum transfer at which the single phonon description starts to break down. For $q \gtrsim q_c$ one has to match to the nuclear recoil regime by including higher order corrections to the matrix element, which we do not attempt here. For a heavy mediator, the fiducial cross section is

$$\sigma_{LA}^{\rm heavy} \approx \overline{\sigma}_0 \times \frac{A}{3m_n^3 v_0^2 c_s} \begin{cases} q_c^3 & \text{Region I} \\ \frac{9\pi}{2R_X^3} & \text{Region II} \\ \frac{27 c_s}{2R_X^4 E_{\rm thres}} & \text{Region III} \end{cases}. \tag{3.47}$$

where we use that $A \approx A_{\rm Ga} \approx A_{\rm As}$. Due to the strong q_c^3/m_n^3 phase space suppression in the coherent regime (region I), we find that phonons in GaAs are never competitive with nuclear recoils in superfluid helium for a heavy mediator. The same conclusion holds for phonons in superfluid helium. For a light mediator on the other hand, the fiducial cross section is

$$\sigma_{LA}^{\rm light} \approx \overline{\sigma}_0 \times q_0^4 \times \frac{A}{m_n^3 v_0^2 c_s} \begin{cases} \frac{c_s}{E_{\rm thres}} & \text{Region I \& II} \\ \frac{9c_s^5}{10R_X^4 E_{\rm thres}^5} & \text{Region III} \end{cases} \tag{3.48}$$

This scaling is much more favorable for a low threshold, phonon based detection principle and, as we shall see in the next section this detection strategy can be competitive with high threshold, high exposure experiments.

Results

We now turn to a quantitative comparison of the numerical results. As discussed extensively in the previous sections, the key quantity is the radius of the ADM nugget, given by

$$R_X = \left(\frac{9\pi}{4}\frac{M_X}{\bar{m}_\chi^4}\right)^{1/3}. \tag{3.49}$$

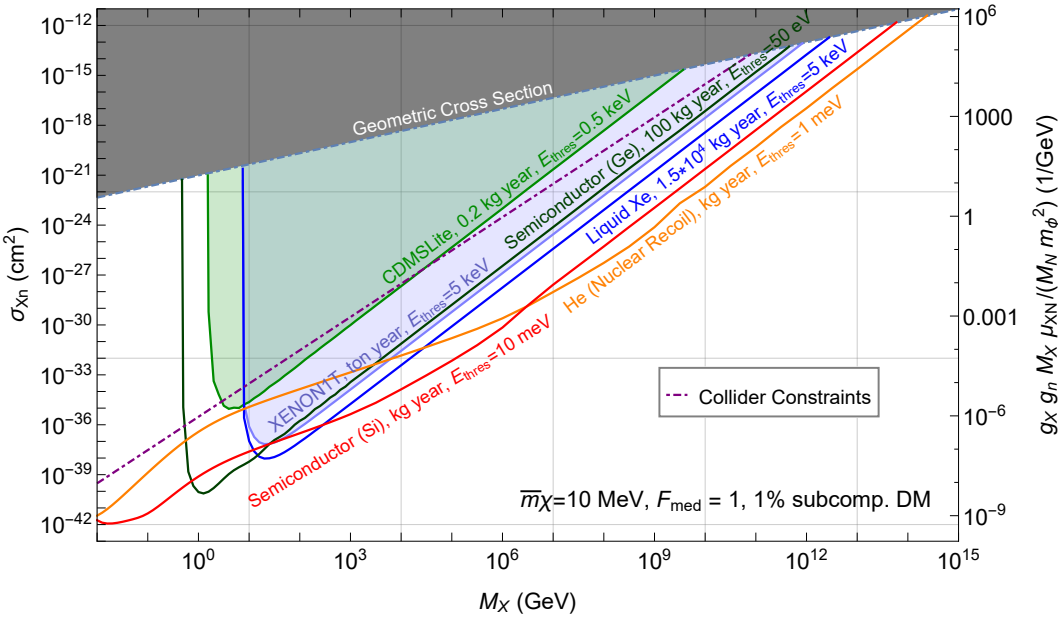

Figure 3.3: Existing and projected reach of experiments in Table 3.1 for heavy mediator coupled to nucleons and nuggets with 10 MeV constituents. We assume nuggets are 1% of the DM density due to SIDM constraints; the dot-dashed purple curve indicates the LHC constraint on the UV completion in (3.10).

In our reach estimate, we fix $\overline{m}_\chi$ to a few benchmark values and vary the ADM nugget mass M_X. For fixed $\overline{m}_\chi$, the radius therefore grows with increasing M_X, while for fixed M_X, smaller $\overline{m}_\chi$ correspond to a larger, less dense ADM nugget. We illustrate the direct detection phenomenology with the limiting cases of $\overline{m}_\chi = 10$ MeV and $\overline{m}_\chi = 10$ GeV; the $\overline{m}_\chi = 10$ MeV benchmark roughly corresponds to the lowest value for the constituent mass for which one can imagine a plausible formation history, consistent with Big Bang Nucleosynthesis. As discussed in Sec. 3.2, this benchmark is also in tension with self-interaction bounds if $M_X \lesssim 4 \times 10^6$ GeV, which leads us to assume that the ADM nuggets make up 1% of the total DM mass density. This bound does not apply for the $\overline{m}_\chi$ =10 GeV benchmark, which will roughly correspond to the highest value for which low threshold experiments can add sensitivity, for a heavy mediator.

The reach for a heavy mediator is shown in Figs. 3.3 and 3.4 for nuggets with constituent masses $\overline{m}_\chi = 10$ MeV and $\overline{m}_\chi = 10$ GeV respectively. In the gray region the cross section exceeds the geometric cross section for an ADM nugget with radius R_X; the parameter space there is unphysical. Current constraints are shown by shaded regions. There are parts of the parameter space, specifically at large cross sections and low nugget masses, where no experiment has any reach, as the nuggets are stopped by an overburden equivalent of around

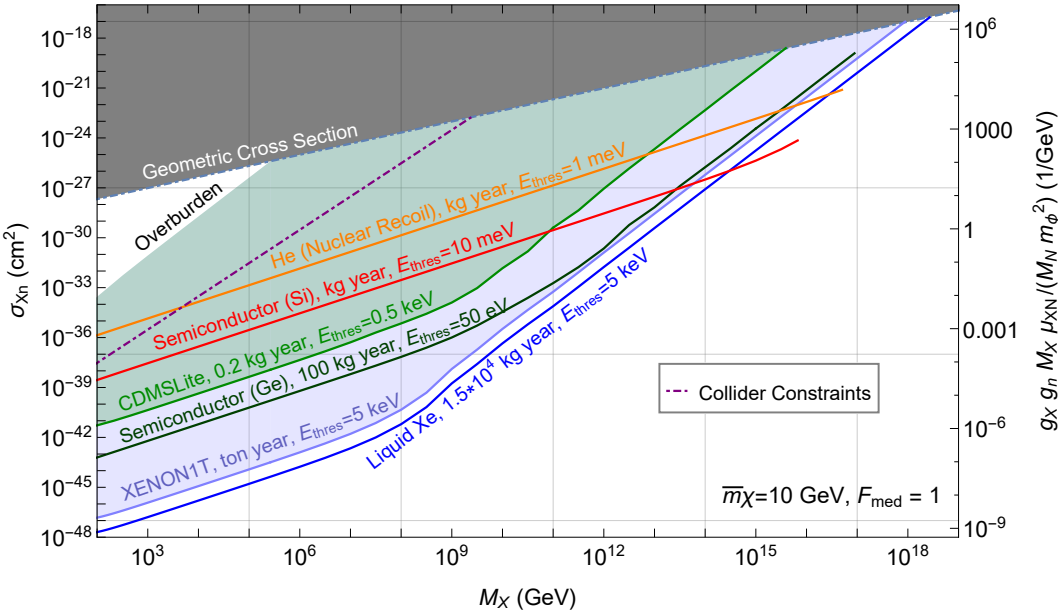

Figure 3.4: Existing and projected reach for the experiments described in Table 3.1, for heavy mediator interacting with nucleons and nuggets with 10 GeV constituents. The white triangle on the left marks where rock overburden eliminates underground direct detection sensitivity. Constraint curves terminate when the expected number of ADM nuggets passing through the detector drops below one per year.

2 km of rock. This overburden effect depends on M_X due to the ADM nugget's form factor, as computed in Appendix A. In other parts of the parameter space, multiple interactions in the detector can occur in the same event, which requires a dedicated analysis [122]. We also indicate, in dot-dashed purple, the LHC constraints on the UV completion described in Sec. 3.2. Lastly, note that the maximum nugget mass that a superfluid helium detector can probe with a kg-year exposure is slightly higher than that which can be probed by a silicon detector with the same exposures because of the difference in the detector volumes.

For $\overline{m}_\chi = 10$ MeV (Fig. 3.3), the ADM nugget is large enough such that the fully coherent regime (Region I) is never available, regardless of the detector. For high threshold, high exposure experiments, even partial coherence is not possible, regardless of M_X. The fiducial cross section is therefore heavily suppressed as the scattering is always in Region III. For a low threshold detector on the other hand, $q_{\min} R_X < 1$ as long as $M_X \lesssim 10^5$ (Si) or $M_X \lesssim 6 \times 10^7$ GeV (He), such that coherent scattering remains possible in part of the phase space (Region II). For larger M_X the low threshold detectors also transition to the fully incoherent regime (Region III), as is evident from the change in slope of the Si and He curves in Fig. 3.3. Beyond this point, the form factor suppression is present for all

experiments but it is more severe for the high threshold detectors.[5] This can be seen from the approximate formula for region III in Eq. (3.41), which shows that the fiducial cross section scales with $1/E_{\rm thres}$. The rate per unit exposure in Eq. (3.31) is moreover proportional to $1/m_N = 1/(A\, m_n)$, such that there is no residual enhancement for large nuclei. This implies that the relative reach of the various experiments in this regime is determined by the ratio of their exposure over their threshold, assuming comparable backgrounds rates.

For $\overline{m}_\chi = 10$ GeV (Fig. 3.4), the ADM nugget has a much smaller radius and thus does not suffer from form factor suppression for even intermediate masses. This means that the traditional, large exposure experiments perform best in most of the parameter space, except for very high M_X. Concretely, only for $M_X \gtrsim 10^{13}$ GeV a low threshold Si experiment with kg-year exposure would outperform the existing XENON1T limit, and even in this case a future liquid xenon experiment is still expected to set the best limit. In the intermediate regime for the constituent mass, 10 MeV $< \overline{m}_\chi <$ 10 GeV, the reach of both types of experiments is complementary: relatively low M_X is covered by liquid xenon detectors, while the reach for high M_X can be better for a low threshold experiment.[6]

The reach for a light mediator is shown in Fig. 3.5. "Light" here refers to a mediator whose mass is low compared to the typical momentum transfer in the scattering, meaning $m_\phi \ll m_N v_0$. The scattering is heavily biased towards the low momentum transfer regime, and a low threshold detector is always advantageous, regardless of the radius of the nugget (see Eq. (3.42)). In this scenario the phonon modes for helium and GaAs have the potential to outperform the high exposure experiments with several orders of magnitude in the full parameter space. For completeness, we also include a number of indirect constraints, for which we assumed the mediator mass m_ϕ to be 1 eV. For this mass value, the maximal coupling to the mediator to the SM nucleons is $g_n \sim 10^{-12}$, as derived from stellar cooling bounds [98]. This constraint on g_n is combined with several constraints on g_χ to demarcate regions that are either excluded via indirect constraints or must be handled with care. For example, DM self-interactions via a light mediator, derived in Eq. (3.15), exclude regions above the red dashed line, labeled as SIDM; this bound can be avoided if ADM nuggets are a subcomponent of the total DM density. There is also a region in Fig. 3.5 which is a priori physical, but for which our approximations do not apply: above the dot-dashed blue line, corresponding to Eq. (3.17), the mediator mass receives important in-medium corrections which should be accounted for in the scattering rate. This effect is expected to weaken the constraints; for more details we refer to Sec. 3.2.

[5] For the liquid xenon detectors the minimum momentum transfer is roughly ~ 10 MeV. For the $\overline{m}_\chi = 10$ MeV benchmark this means that strictly speaking the scattering always occurs in the cross over regime between the form factor description and the DIS description. We expect that the true constraints for the xenon experiments could therefore be somewhat weaker than what is shown in Fig. 3.3.

[6] The reach shown for He and Si is reduced because we assume an upper bound on the detectable energy, 100 meV and 1 eV, respectively. This is an estimate for the final generation of detector concepts, with the lowest thresholds. As these campaigns will occur in stages, gradually lowering the energy range of interest, our projections are likely somewhat conservative for this benchmark. The upper bound on deposited energy also invalidates some of the analytic relations in Sec. 3.3; the necessary modifications are easily derived.

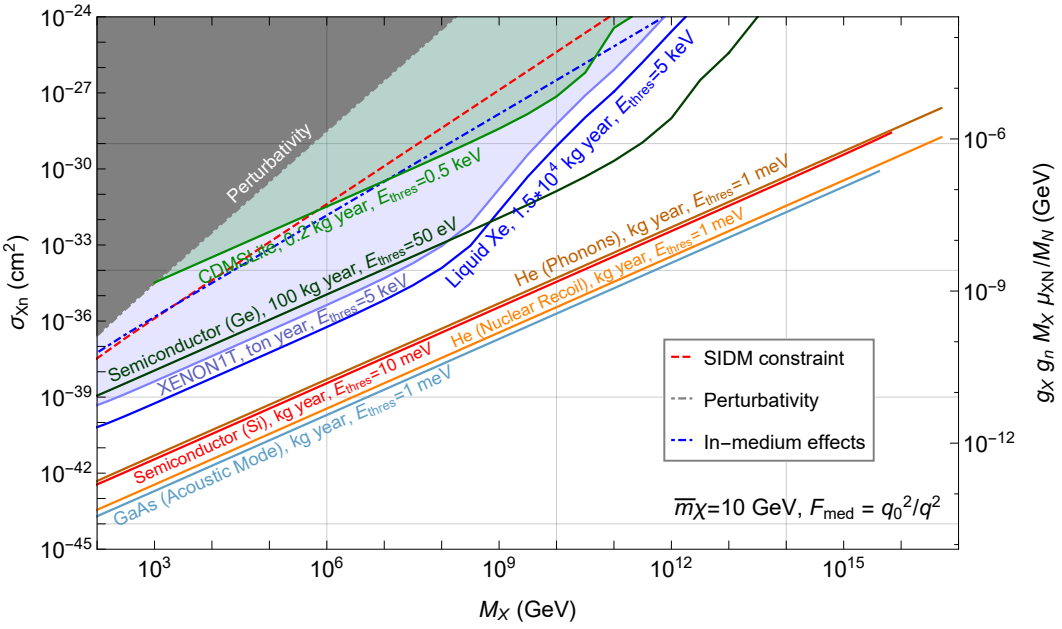

Figure 3.5: Existing and projected reach of experiments described in Table 3.1 for light mediator, coupling to nucleons and nuggets with $\overline{m}_\chi = 10$ GeV constituents. At high M_X, the curves terminate when the expected number of ADM nuggets passing through the detector volume per year drops below one. Above the dot-dashed blue line, the mediator receives important in-medium corrections inside the nugget. For the perturbativity, SIDM and in-medium correction bounds, we saturated the stellar cooling limits by fixing $g_n = 10^{-12}$, assuming a mediator mass of 1 eV (See text for details.)

While we also consider the case in which the light mediator is a dark photon, we will delay the discussion of this interaction until Sec. 3.4, in order to be able to present the constraints from both nucleon and electron interactions at the same time. For now, we just note that due to the heaviness of the DM nuggets, nuclear recoil experiments like XENON1T are able to place constraints on this type of interaction, as shown in Fig. 3.9.

3.4 Electron couplings

In this section, we consider scattering of ADM nuggets with electron couplings, including interactions mediated by dark photons. The leading existing electron-recoil limits are derived from XENON10 data [83, 123–125] and a recent surface run by the SENSEI collaboration [126]; SENSEI had a factor of ~ 10 lower threshold, but substantially smaller exposure. A comparable result exists from the SuperCDMS collaboration [127]. Near future (1-5 years)

detectors will have enhanced sensitivity to electron recoils, primarily by pushing for higher exposure, and in some cases lower thresholds. This includes semiconductor targets (SENSEI [25, 126], DAMIC-K [128], SuperCDMS [25]), scintillators [86], graphene (PTOLEMY [85, 129]) and xenon (LBECA [25]). As an example we take a silicon semiconductor with a kg-year exposure with a two electron threshold, as a future projection for SuperCDMS, SENSEI or DAMIC [25]. Finally, there are slightly longer term prospects for even lower threshold detectors, such as superconducting aluminum [87, 118], Dirac materials [88], and polar materials (e.g. GaAs, sapphire) [81, 82]. As representative examples we consider a superconducting target and, in the case of a dark photon mediator, a polar material (GaAs) and a nuclear recoil experiment (XENON1T). All (proposed) experiments we consider are listed in Table 3.2 (with the exception of XENON1T, which is listed in Table 3.1), along with their (assumed) thresholds and exposure. Just as we did for the nucleon couplings, we have assumed aspirational exposures for the more long term proposals; rescaling the projected limits for different assumptions is trivial.

Experiment	Exposure (kg-year)	Threshold	Timeline	N_{events}
XENON10	0.041	15 eV	existing	BD
SENSEI	5.2×10^{-8}	8.3 eV	existing	BD
Si semiconductor	1	4.7 eV	in progress	3
superconductor	1	1 meV	R&D needed	3
polar material (A' mediator)	1	30 meV	R&D needed	3

Table 3.2: Overview of assumed exposure and approximate thresholds for the existing and future experiments considered in this work, for electron-nugget couplings. N_{events} refers to the number of expected signal events that were assumed to estimate the 90% exclusion limits. (See text for details.) "BD" refers to a bin-dependent analysis, as described in the text.

Electron recoils

For reference, we summarize the dynamic structure factors for electron targets appearing in Eq. (3.31). The dynamic structure factor, $S(\mathbf{q}, \omega)$, in semiconductors and liquid xenon depends strongly on the electron potential in the medium. The electrons in a superconductor can be approximated by a non-interacting Fermi liquid at zero temperature, and the impact of Pauli blocking must be accounted for.

Ionization in Atomic Targets

In this process, the DM ionizes an electron in one of the outer shells of the target atom, Xe in the case at hand. The residual kinetic energy of the electron is deposited in the form

of secondary electrons or (unobserved) scintillation photons. The corresponding structure function is

$$S(q,\omega) = \frac{1}{4}\sum_{n,\ell}\frac{1}{\omega - |\epsilon_{n,\ell}|}|f_{n,\ell}(k',q)|^2 \tag{3.50}$$

with $\epsilon_{n,\ell}$ the binding energy of the atomic level (n,ℓ), $k' \equiv \sqrt{2m_e(\omega - |\epsilon_{n,\ell}|)}$ and the ionization form factor. The form factor $f_{n,\ell}(k',q)$ is non-trivial and must be computed from the atomic wave functions and the wave function of the outgoing, unbound electron, as detailed in Refs. [83, 123, 124, 130]. We compute the structure function and the electron yield as a function of the recoil energy with `QEdark` code [123, 124], which supplies $f_{n,\ell}(k',q)$ for Xe. Since the rate is dominated by the $4d^{10}$ and $5p^6$ shells, we neglect the remaining orbitals in our estimates. We further bin the differential rate according to the expected number electrons and require the signal to be below the XENON10 data [125] at 90% confidence level in each bin. The above approximations reproduce the limits for light, elementary dark matter in [124] to within $\sim 30\%$.

Electronic Transitions in Semiconductors

In semiconducting targets, such as silicon and germanium, the gap between a valence and conduction band is 1.1 eV and 0.67 eV respectively, which corresponds to the lower bound on the energy threshold. In practice, the threshold is often taken to be the energy needed to produce two or three electrons, in order to suppress the dark count rate and/or other low energy backgrounds. The structure function is

$$S(q,\omega) = \frac{1}{n_T}\sum_{i,i'}\sum_{G'}\int_{BZ}\frac{d^3k}{(2\pi)^3}|f_{i,k\to i',k',G'}|^2\delta\left(E_{i',k'} - E_{i,k} - \omega\right) \tag{3.51}$$

where n_T is the electron number density and the i, i' label the initial and final electronic bands, with energy $E_{i,k}$ at momentum k. The sum over G' is over the reciprocal lattice and the integrals over the initial and final electron momenta k, k' are over the first Brillouin zone. The transition matrix element $f_{i,k\to i',k',G'}$ is determined from the electron wave functions and has been evaluated numerically [84] with the `Quantum EXPRESSO` [131] package, and subsequently tabulated as part of the `QEdark` code [84, 123], which we use for our calculations. (See [130] for a semi-analytic approach.)

To convert the energy deposited by the DM to the number of ionization electrons (n_e), we assume the same linear relationship as in [84]. For the existing bounds, we recast the latest SENSEI limit [126]. Since this was a surface run, the one and two electron bins have a large amount of background events and we set a limit only with the $n_e \gtrsim 3$ and $n_e \gtrsim 4$ electrons selections, which respectively correspond to a threshold of 8.3 eV and 11.9 eV. In these two signal regions, 132 and 1 event(s), respectively, were observed and the bounds at 90% confidence level are computed by conservatively assuming that all observed events were signal. For each point in the parameter space, we take the strongest of these two limits. For the future reach of a larger exposure, underground detector, a negligible background is

assumed for $n_e \gtrsim 2$, which corresponds to an effective threshold of 4.7 eV; as a benchmark, we assume an exposure of 1 kg-year.

Scattering in Superconductors

In metal targets, DM can scatter off of the quasi-free valence electrons [87, 118], which have a typical Fermi velocity, $v_F \sim 10^{-2}$. In the superconducting phase, a small gap on the order of an meV develops above the Fermi surface, which forbids scattering processes with energy depositions less than the width of the gap. For energy depositions sufficiently above a meV, the existence of the gap can be neglected and the scattering becomes identical to that in a free Fermi gas, at zero temperature. In this case, the dynamic structure factor is

$$\begin{aligned} S(q,\omega) &= \frac{m_e v(2m_e\mu - \xi^2)}{2\pi q\ n_T}\Theta(\sqrt{2m_e\mu} - \xi) \\ \xi &= \text{Max}\left[\sqrt{2m_e(\mu-\omega)}, \frac{m_e}{q}\left(\omega - \frac{q^2}{2m_e}\right)\right] \end{aligned} \tag{3.52}$$

where m_e is the mass of an electron, μ the chemical potential and n_T is the electron number density. Note that for superconducting aluminum, $\mu \approx 11.7$ eV. The structure function is derived in greater detail in Appendix B. For the future reach, we assume a meV threshold, kg-year exposure and negligible irreducible backgrounds.

If the particle mediating the scattering is a kinetically mixed dark photon, the scattering is subject to screening by the valence electrons of the metal. In practice the rate is suppressed by the Thomas-Fermi screening length, which implies a reduction of the reach of several orders magnitude, depending on the momentum transfer. For our rate calculation we include the full momentum dependent correction to the dark photon propagator, following the discussion in [118].

Polar materials

The detector with a polar material target proposed in [81] can be described as an ultra-low threshold calorimeter for single, athermal phonon excitations. Since polar materials are insulators or semiconductors, the 1-10 meV threshold needed to detect single phonons is well below the band gap of the material. Unlike the examples discussed above, the detector is therefore not optimized for detecting electron excitations directly, but it is nevertheless still possible to excite phonons through the coupling to the inner shell electrons [82]. For a mediator coupling to electrons, a superconducting target tends to perform somewhat better than a polar material target. The kinetically mixed dark photon mediator is however an important exception due to the screening effect described in the previous section, which strongly limits the reach of superconductors for this scenario. For an insulator (e.g. sapphire) or a semiconductor (e.g. GaAs) this issue does not arise.

A defining feature of polar materials is that the optical phonon modes of the crystal correspond to the coherent oscillation of an electric dipole in each unit cell, which implies an

enhanced coupling to a kinetically mixed dark photon. In the limit where the dark photon is massless, the ADM nugget can be thought of as carrying a small electric charge. In this case the dynamic structure factor is [81, 82]

$$S(q,\omega) = \frac{2q^2}{e^2}\frac{\omega_{LO}}{n_T}\left(\frac{1}{\epsilon_\infty} - \frac{1}{\epsilon_0}\right)\delta(\omega_{LO} - \omega), \tag{3.53}$$

taking $\bar{\sigma}_0$ in Eq. (3.27) (for the massless case), $g_e = e$ and $g_t = \kappa e$ with e the electron charge and κ the kinetic mixing parameter. ϵ_0 and ϵ_∞ are the low and high frequency dielectric constants respectively, and $\omega_{\rm LO}$ is the energy of the longitudinal optical phonon in the zero momentum limit. The reference momentum is taken to be $q_0 = \alpha m_e$.[7] We note that the above equation is an analytic approximation, valid only for isotropic crystals like GaAs. The general structure function is more complicated and must be evaluated numerically; see [82] for details. Since the numerical treatment is rather computationally intensive, we restrict ourselves to the analytic formula in Eq. (3.53) for GaAs in this work. As in Sec. 3.3, we require $q < 1$ keV, to ensure the validity of the phonon description.

Results

We now turn to a quantitative comparison of the numerical results. As in the case of coupling to nucleons, the key quantity is the radius of ADM nugget, given by

$$R_X = \left(\frac{9\pi}{4}\frac{M_X}{\bar{m}_\chi^4}\right)^{1/3}. \tag{3.54}$$

In our reach estimate, we again fix $\bar{m}_\chi$ to two benchmark values and vary the ADM nugget mass M_X. As for DM coupling to nuclei, the scaling of a detector's sensitivity falls into three unique regions (see Fig. 3.2), depending on how the momentum transfer compares to the inverse radius. In Region I, the maximum allowable momentum transfer, $q_{\rm max}$, is smaller than the inverse radius. The scattering of a composite nugget is therefore fully coherent and also indistinguishable from that of an elementary DM particle. In Region II, while $q_{\rm max}R_X \gtrsim 1$, the lowest momentum transfer to which the detector is sensitive, $q_{\rm min}$, is still smaller than $1/R_X$. The scattering is therefore still coherent, but only in part of the phase space. In Region III, $q_{\rm min}R_X \gtrsim 1$ and the scattering is never coherent and thus the rate is strongly suppressed.

The transitions between Region I and II and Region II and III occur roughly when the inverse radius is small compared to the maximal momentum transfer and the experimental

[7] Note that our definition of the reference cross section $\bar{\sigma}_0$ differs with a factor of 4 from the definition in [81, 82].

momentum transfer threshold, i.e.

$$M_X \sim \begin{cases} 3\times 10^6\,\mathrm{GeV}\times\left(\frac{\overline{m}_\chi}{10\,\mathrm{MeV}}\right)^4\times\left(\frac{8\,\mathrm{keV}}{q_{\max}}\right)^3 & \text{transition between Region I and II} \\ 10^9\,\mathrm{GeV}\times\left(\frac{\overline{m}_\chi}{10\,\mathrm{MeV}}\right)^4\times\left(\frac{\mathrm{eV}}{E_{\mathrm{thres}}}\right)^3 & \text{transition between Region II and III} \end{cases} \tag{3.55}$$

where v_0 is the typical DM velocity in the Milky Way and $q_{\max}\approx 2\alpha m_e$, as explained below; this is significantly smaller than in the nuclear recoil case. Notice that, at least for atomic ionization and semiconductor detectors, Region II is fairly narrow, as $q_{\max}$ is numerically close to $q_{\min}\approx E_{\mathrm{thres}}/v_0$.

The structure functions are substantially more complicated than those for nucleon couplings in Sec. 3.3, but we can still extract the rough scaling of the scattering rate by making a number of additional approximations: if the electron were free, the structure function would simply be Eq. (3.34), except with the mass of the electron instead of mass of the nucleus and $A=1$. The effect of the electron being in a bound state is two-fold: first, the energy transferred to the electron, E_e, is now related to the momentum transfer via

$$E_e = \mathbf{q}\cdot\mathbf{v} - \frac{q^2}{2\mu_{XN}} \approx \mathbf{q}\cdot\mathbf{v}\,, \tag{3.56}$$

found by imposing energy conservation on the DM-electron-nucleus system. This implies the relation

$$q_{\min} = E_{\mathrm{thres}}/v_0 \tag{3.57}$$

between the minimum possible momentum transfer ($q_{\min}$) and the detector threshold (E_{thres}). Secondly, the electron is not only not at rest, but its velocity in the atom, v_e, is larger than the mean DM velocity. This implies that $q_{\max}\approx 2m_e v_e$, where $v_e\approx\alpha\approx 10^{-2}$, and we expect that the cross sections for scattering via a heavy mediator roughly scales as

$$\sigma_{ER}^{\mathrm{heavy}} \sim \overline{\sigma}_0\times\begin{cases} \frac{q_{\max}^2}{4v_0^2m_e^2} = \frac{v_e^2}{v_0^2} & \text{Region I} \\ \frac{1}{R_X^2}\frac{2}{v_0^2m_e^2} & \text{Region II} \\ \frac{1}{R_X^4}\frac{2}{q_{\min}^2v_0^2m_e^2} = \frac{1}{R_X^4}\frac{2}{m_e^2E_{\mathrm{thres}}^2} & \text{Region III} \end{cases}, \tag{3.58}$$

while for a light mediator, we expect the cross section to scale as

$$\sigma_{ER}^{\mathrm{light}} \sim \overline{\sigma}_0\times q_0^4\times\begin{cases} \frac{1}{4q_{\min}^2v_0^2m_e^2} = \frac{v_e^2}{v_0^2}\frac{1}{m_e^2E_{\mathrm{thres}}^2} & \text{Region I \& II} \\ \frac{1}{R_X^4}\frac{1}{v_0^2m_e^2q_{\min}^6} = \frac{1}{R_X^4}\frac{v_e^6}{v_0^2}\frac{1}{m_e^2E_{\mathrm{thres}}^6} & \text{Region III} \end{cases}. \tag{3.59}$$

Note that while these electron recoil cross sections have the same scaling dependence on $q_{\max}$, $q_{\min}$ and R_X as for the nuclear recoil case, the dependence on E_{thres} is altered, following

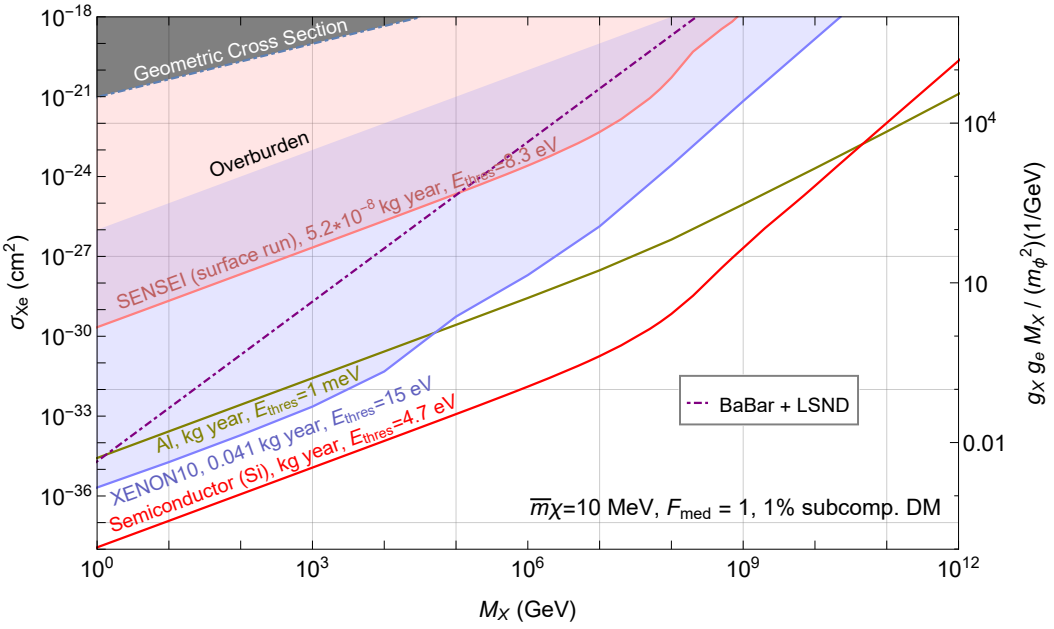

Figure 3.6: Existing and projected reach of experiments in Table 3.2 for heavy mediator interacting with electrons and nuggets with 10 MeV constituents. We assume nuggets make up 1% of the total DM density to evade SIDM constraints; the dot-dashed purple line is an intensity frontier constraint on a 10 MeV mediator; see Sec. 3.2. The grey area marks where geometric cross section is exceeded.

Eq. (3.57). These relatively crude approximations broadly reproduce the scaling behavior of the reach of the various detector types, but their quantitative accuracy is not always guaranteed, as more subtle but numerically important in-medium effects (e.g. Pauli blocking) are not accounted for. However, these in-medium effects can also sometimes be included in a similarly rough manner; when appropriate, we will provide an estimate of the consequences of these effects on specific detector limits in our discussions below. In our result plots, we always present the full, numerical results, as outlined in the preceding sections.

The reach for a heavy mediator is shown in Figs. 3.6 and 3.7 for $\overline{m}_\chi = 10$ MeV and $\overline{m}_\chi = 10$ GeV respectively. The grayed region again indicates cross sections larger than geometric, which are unphysical. For electron couplings there is a mild overburden effect for underground experiments, as argued in Appendix A. The parameter space where this is relevant is however fully covered by the SENSEI surface run. The dot-dashed purple line refers to the constraint in Eq. (3.11), which represents the intensity frontier bounds on the mediator particle, specifically from BaBar and LSND (see Sec. 3.2 for details).

When in Region I, i.e. when the ADM nuggets are quite small, low threshold detectors (superconductors in the present context) do not have an advantage over their counterparts

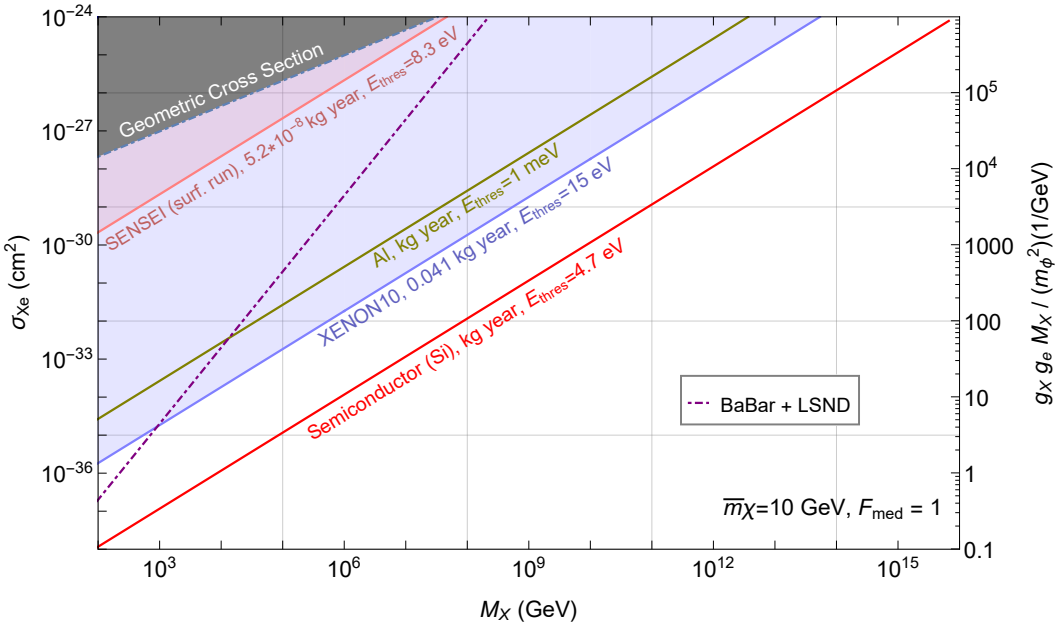

Figure 3.7: Existing and projected reach of experiments in Table 3.2 for heavy mediator coupled to electrons and nuggets with 10 GeV constituents. The dot-dashed purple curve is an intensity frontier constraint on a 10 MeV mediator, see Sec. 3.2. The grey area marks where geometric cross section is exceeded.

with higher thresholds: comparing a 1 eV threshold semiconducting experiment to a meV threshold superconducting experiment only shows the effect of Pauli blocking, which weakens the constraints by approximately three orders of magnitude. The initially surprising appearance of Pauli blocking can be understood in the following way: While one might naively expect that the rate for DM scattering in superconductors should be dominated by electrons deep in the Fermi sea (because the nugget carries plenty of kinetic energy), the rate is instead dominated by energy deposits near the detector threshold. The physical reason is that scattering of heavy, slow-moving dark matter off of a fast electron typically imparts a momentum transfer twice the initial electron momentum. For the electrons deep in Fermi sea, this does not suffice to knock the electron across the Fermi surface, and as such the process is Pauli blocked. Thus one can only scatter off electrons near the Fermi surface, which substantially reduces the number of available scattering centers for the ADM nugget.

Of the existing constraints for $\overline{m}_\chi = 10$ MeV (Fig. 3.6), the XENON10 limit is substantially stronger than the SENSEI limit, due to its much larger exposure. The 1, 2 and 3 electron bins for XENON10 however have a substantial amount of background, such that the reach at low M_X is primarily driven by bins with 4 or more electrons, effectively raising the threshold to $\sim$ 60 eV. With Eq. (3.55), this explains why the limit from XENON10

starts to deteriorate at lower M_X, as compared to the SENSEI limit. Focusing next on the reach of future semi- and superconductor experiments, note that both have the same $q_{\rm max}$, as it is set by twice the typical electron momentum. Therefore, both detectors transition between Region I and Region II around $M_X \gtrsim 3 \times 10^6$ GeV, and the difference in their reach at low nugget masses can be understood completely through the existence of Pauli blocking in superconductors. Moreover, the semiconductor detector rather quickly transitions from Region II to Region III, due the numerical coincidence that $q_{\rm min}$ is less than an order of magnitude smaller than $q_{\rm max}$ for this detector. This transition is delayed for the low threshold, superconducting device, such that it can eventually compensate for the suppression due to Pauli blocking. This is what occurs in Fig. 3.6, where superconductors begin to dominate over semiconductors around $M_X \approx 10^{11}$ GeV.

For more compact nuggets, i.e. with $\overline{m}_\chi = 10$ GeV, the ADM nuggets behave like point particles for all detectors, and there is no form factor suppression. The semiconductor (or ionization) experiments therefore always dominate, since they do not suffer from Pauli blocking. The reach is therefore primarily exposure-driven, as is shown in Fig. 3.7. A future noble liquid detector with sensitivity to ionization signals and more exposure than XENON10 (e.g. LBECA) could therefore be an interesting alternative to search for ADM nuggets, or heavy DM with electron couplings more generally. That is, provided that the backgrounds can be kept low, a caveat which applies to all future proposals we consider.

The reach for a light scalar mediator and for a light, kinetically mixed dark photon is shown in Figs. 3.8 and 3.9 respectively; both are for point-like nuggets, with $\overline{m}_\chi = 10\,\text{GeV}$. As in the nuclear recoil case, a mediator is considered "light" if its mass is small compared to the typical momentum transfer, in this case $m_\phi \ll \alpha m_e$. For the scalar mediator case, we take the mediator mass to be $m_\phi = 1$ eV, which corresponds to a maximal coupling to electrons of $g_e \sim 10^{-15}$ from stellar cooling constraints [98]. For the vector mediator case, we fix $\kappa = 10^{-10}$, which is consistent with stellar cooling bounds for a dark photon with mass $m_{A'} = 10^{-2}$ eV [99]. This constraint is combined with the constraints from perturbativity ($g_\chi \lesssim 1$) and dark matter self-interactions in Eq. (3.15). We also include the lines that demarcate regions that are a priori physical, but for which our approximations do not hold. In particular, in the region above the dot-dashed blue line, defined by Eq. (3.17), the mediator mass receives important in-medium corrections, as the charge density of the fermions can dramatically alter the light mediator's potential. Lastly, note that the maximum nugget mass that GaAs, silicon semiconductor and aluminum superconductor detectors can probe with a kg-year exposure are slightly different due to the difference in the detector volumes.

In direct detection experiments, the scattering rate for interactions via a light mediator is always dominated by low momentum transfer, due to the q_0^2/q^2 form factor in Eq. (3.26) and so low threshold experiments always perform best, as long as Pauli blocking or in-medium screening effects are not too severe. Focusing first on scalar mediators (Fig. 3.8), the existing constraints are provided by XENON10 and the surface run of SENSEI. For the future reach, superconductors dominate over semiconductors, despite the Pauli blocking suppression, as the rate per unit exposure is proportional to $1/q_{\rm min}^2 \sim 1/E_{\rm thres}^2$.

There are several important differences when considering a dark photon mediator (Fig. 3.9):

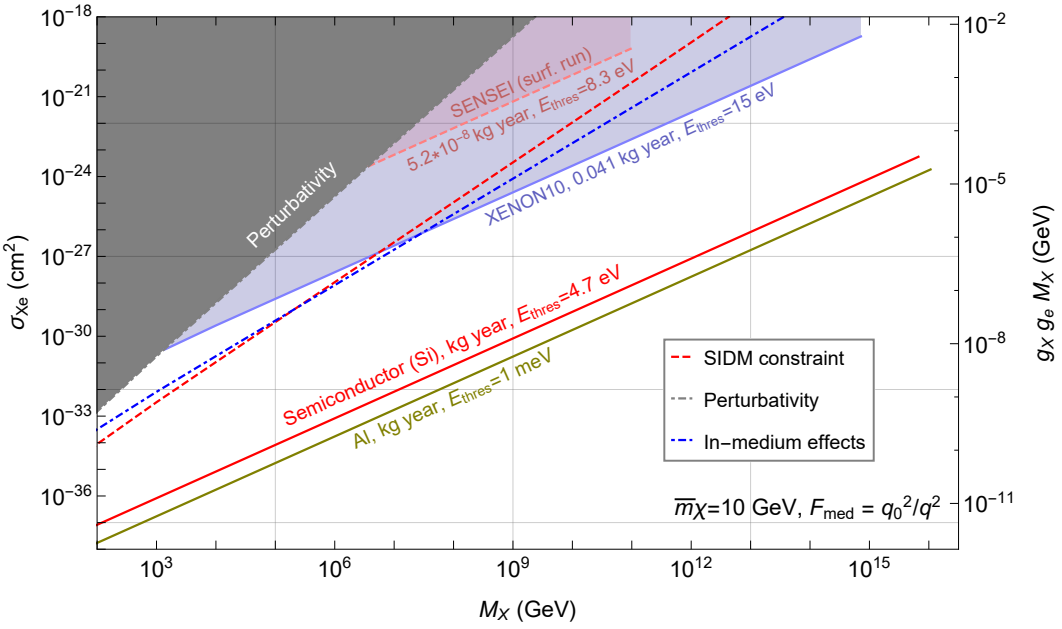

Figure 3.8: Reach curves of experiments in Table 3.2 for light scalar mediator. The perturbativity, in-medium effects and SIDM constraints are drawn assuming $g_e = 10^{-15}$, consistent with stellar cooling bounds for $m_\phi = 1$ eV. Pauli blocking is present only in superconductors.

For polar crystals (e.g. GaAs), the dark photon has a strong coupling to the optical phonons in material, which enhances their sensitivity. Superconductors on the other hand pay a large penalty in reach due to the screening by the valence electrons, as discussed in Sec. 3.4. On the other hand, for point-like nuggets, the typical momentum transfer can be substantially larger than a keV. This means that the electric charge of a nucleus is not significantly screened in the high threshold, noble liquid detectors, resulting in a nuclear recoil signature with coupling proportion to the charge of the nucleus (see e.g. [132]). As a result, XENON1T has a sensitivity similiar to that of a semiconductor detector for masses below 10^8 GeV. Above this mass, the DM form factor becomes nontrivial for XENON1T and thus the rate is suppressed relative to that in semiconductors. For indirect constraints, we also demarcate, with a dot-dashed green line, where the dark Coulomb barrier would forbid nuggets from successfully undergoing fusion in the early universe, as given in Eq. (3.19). Depending on whether the last fusion reaction to freeze out is between two large nuggets or a large nugget and a free constituents or small nugget affects the mass of the maximum nugget that can be synthesized [66, 69] and so we choose to plot both of these constraints.

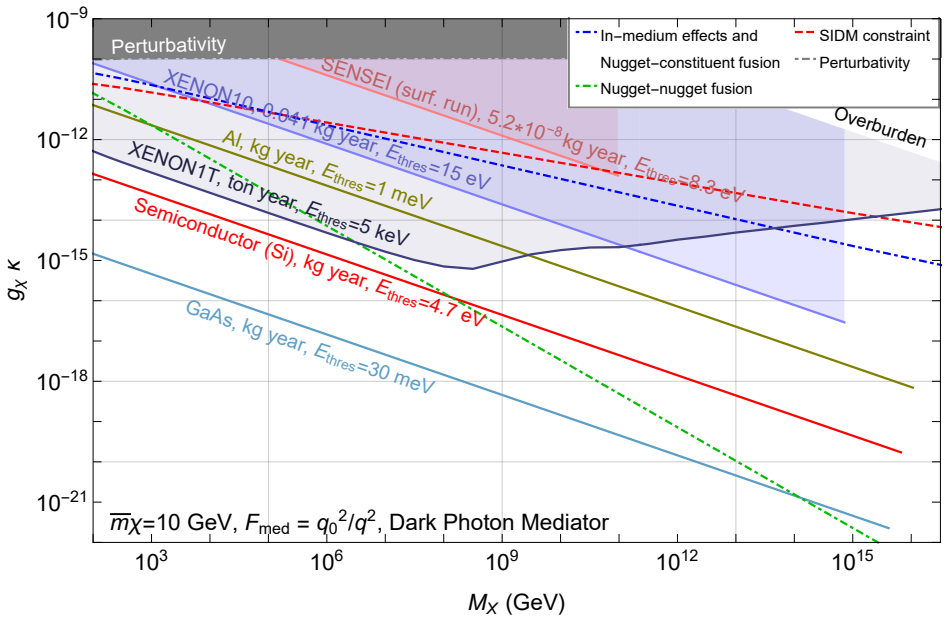

Figure 3.9: Reach curves for experiments listed in Table 3.2 for dark photon mediators. All non-direct detection constraints, denoted by dot-dashed lines, are drawn assuming $\kappa = 10^{-10}$, consistent with stellar cooling bounds for $m_{A'} = 10^{-2}$ eV. Early universe nugget formation constraints how large g_χ can be, marked with blue and green dot dashed curves.

3.5 Conclusions

We have considered the detection of nuggets of Asymmetric Dark Matter, comparing and contrasting low threshold but low exposure proposed experiments (such as superconductors, superfluid helium, polar materials and semi-conductors) with higher threshold but larger exposure experiments (notably the traditional noble liquid xenon experiments). We found that both types of experiments have a role to play:

- Larger experiments are more successful at accessing compact and lighter nuggets that interact with the Standard Model via a heavy mediator;
- Smaller, but lower threshold, experiments can dominate for less dense nuggets and for nuggets which interact with the Standard Model via a longer range mediator.

It has been shown that large bound states of Asymmetric Dark Matter arise quite generically in the presence of a sufficiently strong attractive force, and their astrophysical and cosmological evolution can be quite distinct from other known DM candidates. It is therefore important to pursue complimentary search strategies for constraining these intriguing dark matter candidates.

There are number of possible future directions: Firstly, in our analysis we have not considered the likely possibility that the ADM nuggets follow a non-trivial mass distribution, which can be bimodal in the case of a bottleneck in the formation history [69]. In such a scenario, there could be a signal from larger nuggets in one or more low threshold experiments, simultaneously with a signal from the smaller nuggets in the traditional large noble liquid detectors. Moreover it could be interesting to revisit some of the prior studies of the differential energy spectrum [73, 74] by including low threshold detectors, as well as correlating the spectrum with the formation history of the ADM nuggets.

Chapter 4

Directional Dark Matter Detection in Anisotropic Dirac Materials

4.1 Introduction

The direct detection of dark matter has seen a dramatic broadening of scope beyond the traditional domains of the search for the Weakly Interacting Massive Particle (WIMP) and the axion. Both are highly motivated by solving other problems in the SM sector, such as the hierarchy problem (WIMP) and the strong CP problem (axion). However, the WIMP has been increasingly constrained by highly sensitive experiments that have searched for new physics at the weak scale for decades.

At the same time, visible and dark matter may originate from two separate sectors, independent of any problems in the SM [56]. The development of the hidden sector paradigm has opened a fruitful direction in building models of dark matter. Similar to the SM, the lightest particle of the dark sector may be stable thanks to a gauge or global symmetry. The interactions with the SM may be only gravitational, or mediated by new forces that interact only very feebly with the dark and/or visible sectors. However, these feeble interactions with the SM may be crucial in setting the dark matter abundance, as is typical, for example, in models of MeV dark matter [55, 133, 134], WIMPless miracle DM [135], Asymmetric DM [61, 136], GeV hidden sector dark matter [137–139], freeze-in DM [140], and Strongly Interacting Massive Particles [60]. In this case, well-motivated and clear benchmarks exist to search for dark matter in hidden sectors. Two classic examples are Asymmetric Dark Matter annihilating its symmetric abundance through the dark photon [62], as well as dark-photon mediated dark matter produced through a freeze-in process [141, 142].

While there are many well-motivated models, if the mass of the dark matter in the hidden sector is below approximately a GeV, existing technologies to search for the WIMP through nuclear recoils are not sensitive to it. However, recent years have seen the development of many new ideas to detect sub-GeV dark matter (see Ref. [25] for an extensive review). When the dark matter carries more energy than electronic excitation energies–typically in the 1-10

eV range, corresponding to the kinetic energy of 1-10 MeV dark matter–semiconductor [83, 84, 143] or noble liquid [123] targets developed to search for the WIMP through nuclear recoils with keV energy deposition can be extended to search instead for valence-to-conduction-band transitions or ionization. The challenge is to reduce dark counts and increase sensitivity to energy depositions three orders of magnitude below that needed for WIMPs. This program is well under way in noble liquid [124] and silicon targets, and is actively being pursued in collaborations such as SENSEI [126, 144, 145], DAMIC [146, 147] and SuperCDMS [127, 148–151].

When the DM mass drops below an MeV, new ideas and targets must be found. This has been the focus of intense efforts on small gap materials, such as superconductors [87, 118], graphene [85], and Dirac Materials [88] in the case of electronic excitations, and superfluid helium [79, 80] and polar materials [81] when the DM couples to nuclei or ions.

In this chapter, we will focus on electronic excitations, and in particular dark photon mediated couplings to electrons in Dirac semimetals. These materials have a small band gap of order $\mathcal{O}(1-10\ \text{meV})$, allowing to probe keV-MeV mass DM through scattering. Superconductors are another small gap material that can probe sub-MeV dark matter interacting with the electromagnetic current via a kinetically mixed dark photon, but in-medium effects have been shown to have a dramatic effect on the dark matter interaction rate [118]. The large in-medium effects (or, equivalently, optical response) are a result of the large electron density of states near the Fermi surface of a metal. Dirac materials were proposed in Ref. [88] as an antidote to this problem: the optical response of Dirac materials is much smaller than superconductors and more similar to a semiconductor. At the same time, the presence of states within $\mathcal{O}(1-10\ \text{meV})$ of the Fermi surface gives sensitivity to similarly light DM as for superconductors. An additional desirable feature is that Dirac materials feature anisotropic Fermi velocities and permittivity tensor, suggesting that dark matter interaction rates should be dependent on the orientation of the material with respect to the dark matter wind, inducing a daily modulation. Such a modulation is a smoking gun signature for dark matter interactions, distinguishing signal from background.

The goal of this chapter is to explore in detail how direct detection signals are affected by Dirac materials anisotropies: both the electron Fermi velocities, which dominate the kinematics of the DM-electron scattering, and the permittivity tensor, which characterizes the strength of the electron interactions with the dark photon. We find that daily modulation is $O(1)$ for DM scatterings, while no modulation is present for DM absorption. Since the scattering rate modulation turns out to be dominated by anisotropies in the crystal dielectric, it can be maximized by orienting the crystal in such a way that the DM wind is completely aligned with the smallest and largest component of the dielectric tensor at two different times of the day.

In deriving these results, we also identify and correct a critical fallacy in the formalism previously used to analytically derive the dielectric tensor of Dirac materials [118, 152]. Specifically, we point out that the contribution of electronic states far from the Fermi surface, while previously ignored, dominates the dielectric. The inclusion of these states drastically changes the amount of in-medium screening and therefore the projected reach for Dirac

Materials.

Strong anisotropy and daily modulation in sub-MeV dark matter interaction rates are also a feature of polar materials, as proposed in Ref. [82], though in Dirac Materials the interaction is with electrons rather than ions. Other proposals for directional detection of DM candidates include using two-dimensional materials like graphene [85] in the case of DM coupling to electrons; defect production in crystals [78, 153], and nuclear recoils in semiconductors [154].

The outline of this chapter is as follows. In the next Section we lay out the formalism for calculating dark matter interactions with in-medium effects. In Sec. 4.3, we define our conventions for the orientation of the crystal with respect to the DM wind. Then in Secs. 4.4 and 4.5, we compute the anisotropic absorption and scattering rates. Finally we conclude.

4.2 Dark Matter Interactions with In-Medium Effects

As a benchmark model we consider a dark sector coupled to the Standard Model through a kinetically mixed dark photon, [1]

$$\mathscr{L} \supset -\frac{1}{4}F_{\mu\nu}F^{\mu\nu} - \frac{1}{4}F'_{\mu\nu}F'^{\mu\nu} + \frac{\varepsilon}{2}F_{\mu\nu}F'^{\mu\nu} + eJ^{\mu}_{\rm EM}A_{\mu} + g_{\rm D}J^{\mu}_{\rm DM}A'_{\mu} + \frac{m^2_{A'}}{2}A'^{\mu}A'_{\mu}\,, \tag{4.1}$$

where $F_{\mu\nu}$ ($F'_{\mu\nu}$) is the electromagnetic (dark) field strength, ε the kinetic mixing parameter and $J^{\mu}_{\rm EM\ (DM)}$ the electromagnetic (dark) current that couples to (dark) photons with a coupling e (g_D). The dark photon has a mass $m_{A'}$ which can be generated either by a dark Higgs or through the Stueckelberg mechanism [155] (though astrophysical constraints are weakest for the case of a Stueckelberg dark photon [156]). In the vacuum, the propagating photon (found by diagonalizing the kinetic term in Eq. 4.1) is $\tilde{A}_{\mu} = A_{\mu} - \varepsilon A'_{\mu}$. In this basis the dark photon mass eigenstate A' couples to the electromagnetic current with a strength $e\varepsilon$.

Because of this coupling, the propagation of a dark photon in optically responsive media is modified. Specifically, including in-medium effects and dropping $\mathcal{O}(\varepsilon^2)$ terms, we can write down the effective Lagrangian (in the $\tilde{A}$, A' basis)

$$\mathscr{L} \supset -\frac{1}{4}\tilde{F}_{\mu\nu}\tilde{F}^{\mu\nu} - \frac{1}{4}F'_{\mu\nu}F'^{\mu\nu} + eJ^{\mu}_{\rm EM}\left(\tilde{A}_{\mu} + \varepsilon A'_{\mu}\right) + g_{\rm D}J^{\mu}_{\rm DM}A'_{\mu} + \frac{m^2_{A'}}{2}A'^{\mu}A'_{\mu} \tag{4.2}$$

$$+\frac{1}{2}\tilde{A}^{\mu}\Pi_{\mu\nu}\tilde{A}^{\nu} + \varepsilon\tilde{A}^{\mu}\Pi_{\mu\nu}A'^{\nu} \tag{4.3}$$

where the in-medium polarization tensor is defined as $\Pi_{\mu\nu} \equiv ie^2\langle J^{\mu}_{\rm EM}J^{\nu}_{\rm EM}\rangle$, and the equation of motion has been used to derive the last line. In the familiar case of isotropic materials, the polarization tensor can be written as $\Pi^{\mu\nu} = \Pi_T(\epsilon^{\mu}_{+}\epsilon^{\nu}_{+} + \epsilon^{\mu}_{-}\epsilon^{\nu}_{-}) + \Pi_L\epsilon^{\mu}_{L}\epsilon^{\nu}_{L}$, with ϵ_L and $\epsilon_{+,-}$

[1] Notice that reference [88] uses a different conventions for the sign of the mixing term.

the longitudinal and transverse polarization vectors. For $q \parallel \hat{z}$, they can be written as:

$$\epsilon_L = \frac{1}{\sqrt{q^2}}\Big(|\mathbf{q}|, \omega\,\hat{q}\Big) \qquad \epsilon_\pm = \frac{1}{\sqrt{2}}\Big(0, 1, \pm i, 0\Big)\,. \tag{4.4}$$

where $q = (\omega, \mathbf{q})$ is the four-momentum transfer. One then finds that transverse and longitudinal dark photons remain decoupled during their propagation in a isotropic medium and interact with the electromagnetic current with reduced couplings [118]:

$$\mathscr{L} \supset \varepsilon e \frac{q^2}{q^2 - \Pi_{L,T}} A'^{T,L}_\mu J^\mu_{\rm EM}\,. \tag{4.5}$$

In the case of anisotropic materials, the polarization tensor cannot be decomposed into a longitudinal and a transverse component. This induces a mixing between longitudinal and transverse polarizations that can be parametrized in terms of a symmetric 3×3 mixing matrix, $\mathcal{K}$, defined as

$$\mathcal{K}_{AB} \equiv (\epsilon^\mu_A)^\star \Pi_{\mu\nu} \epsilon^\nu_B, \tag{4.6}$$

with A and B running over longitudinal and transverse polarizations. It is therefore useful to choose a basis, $\epsilon^\mu_{i=1,2,3}$, for the physical polarizations that is not mixed by in-medium propagation. This basis is found using the 3×3 unitary matrix, $\mathcal{S}$, that diagonalizes the mixing matrix:

$$(\epsilon^\mu_1, \epsilon^\mu_2, \epsilon^\mu_3) = \mathcal{S} \begin{pmatrix} \epsilon^\mu_L \\ \epsilon^\mu_+ \\ \epsilon^\mu_- \end{pmatrix} \qquad \text{with} \qquad \mathcal{S}^{-1}\mathcal{K}\mathcal{S} = \text{diag}\Big(\pi_1(q), \pi_2(q), \pi_3(q)\Big)\,. \tag{4.7}$$

In this new basis, the Lagrangian of Eq. 4.2 takes the form

$$\mathscr{L} \supset -\frac{1}{4}\tilde{F}^i_{\mu\nu}\tilde{F}^{\mu\nu}_i - \frac{1}{4}F'^i_{\mu\nu}F'^{\mu\nu}_i + eJ^\mu_{\rm EM}\left(\tilde{A}^i_\mu + \varepsilon A'^i_\mu\right) + g_{\rm D}J^\mu_{\rm DM}A'^i_\mu - \frac{m^2_{A'}}{2}A'^\mu_i A'^i_\mu \tag{4.8}$$

$$- \frac{\pi_i}{2}\tilde{A}^i_\mu\tilde{A}^\mu_i - \varepsilon\pi_i\tilde{A}^i_\mu A'^\mu_i \tag{4.9}$$

and can be diagonalized making the following field redefinition:

$$\tilde{A}^i_\mu = \bar{A}^i_\mu + \frac{\varepsilon\pi_i(q)}{m^2_{A'} - \pi_i(q)}\bar{A}'^i_\mu \qquad A'^i_\mu = \bar{A}'^i_\mu - \frac{\varepsilon\pi_i(q)}{m^2_{A'} - \pi_i(q)}\bar{A}^i_\mu\,. \tag{4.10}$$

One then finds that the propagating dark photons $\bar{A}'_i$ couple to the electromagnetic current as:

$$\mathscr{L} \supset \varepsilon e \frac{q^2}{q^2 - \pi_i}\bar{A}'^i_\mu J^\mu_{\rm EM}\,. \tag{4.11}$$

Thus we see that in the anisotropic case the role of $\Pi_{L,T}$ is played by the mixing matrix eigenvalues π_i.

Working in Lorentz gauge, the in-medium photon propagator takes the form

$$G^{\mu\nu}_{\rm med}(q) = \sum_i \frac{P_i^{\mu\nu}}{\pi_i - q^2} \tag{4.12}$$

where P_i is the projector operator on the direction of the i-th polarization. In order to compute the eigenvalues of the mixing matrix, we relate its components to the optical properties of the medium (see appendix C for details):

$$\mathcal{K}_{LL} = q^2\,(1 - \hat{\mathbf{q}}\cdot\boldsymbol{\epsilon}\cdot\hat{\mathbf{q}}) \qquad \mathcal{K}_{L\pm} = -\omega q\,\hat{q}\cdot\boldsymbol{\epsilon}\cdot\hat{\epsilon}_\pm \qquad \mathcal{K}_{\pm\pm} = \omega^2\,(1 - \hat{\epsilon}_\mp\cdot\boldsymbol{\epsilon}\cdot\hat{\epsilon}_\pm) \tag{4.13}$$

where $\boldsymbol{\epsilon}$ is the dielectric tensor.[2]

From Eq. 4.13, it is clear that in the scattering limit ($|q^2| \sim \mathbf{q}^2 \gg \omega^2$) the mixing matrix is dominated by the $\mathcal{K}_{LL}$ component. Therefore, for DM scattering there is a negligible mixing between longitudinal and transverse polarizations, and the rate is dominated by the longitudinal degrees of freedom whose in-medium propagator is given by

$$G^{\mu\nu} = \frac{P_L^{\mu\nu}}{q^2(\hat{\mathbf{q}}\cdot\boldsymbol{\epsilon}\cdot\hat{\mathbf{q}})}. \tag{4.14}$$

Conversely, in the absorption limit, all components of the mixing matrix are of the same order. Hence in-medium propagation gives rise to a sizable mixing. Therefore, to study DM absorption we need to work in the basis defined in Eq. 4.7 and use the general in-medium propagator given in Eq. 4.12.

4.3 Preliminaries: Dark Matter Wind

The effects we are considering arise because the DM velocity with respect to the detector changes as the Earth rotates around its axis, see Fig. 4.1. There are two kinds of effects. The first is kinematic, where the flux of DM particles in the kinematic configuration that can excite a response in the target changes on a daily basis. This effect is dominated by the anisotropy of the Fermi velocity in the material. The second is due to the size of the matrix element, as shown for example in Eq. 4.14, where the direction of the momentum transfer (typically oriented along the DM wind) changes with respect to the anisotropic dielectric tensor $\boldsymbol{\epsilon}$. We will detail these effects separately for both absorption and scattering below.

But before moving to the results we summarize here our conventions for the DM velocity distribution and the orientation of the DM wind in the crystal rest frame, using a set-up similar to Ref. [82]. For the velocity distribution in the galactic rest frame, $f_{\rm gal}(\mathbf{v})$, we assume a Maxwellian form, with velocity dispersion $v_0 = 220\,\mathrm{Km/\,s}$, truncated at $v_{esc} = 500\,\mathrm{Km/\,s}$.

[2] We will neglect the ion contribution to the dielectric tensor since it is expected to be sub-leading compared to the electronic one.

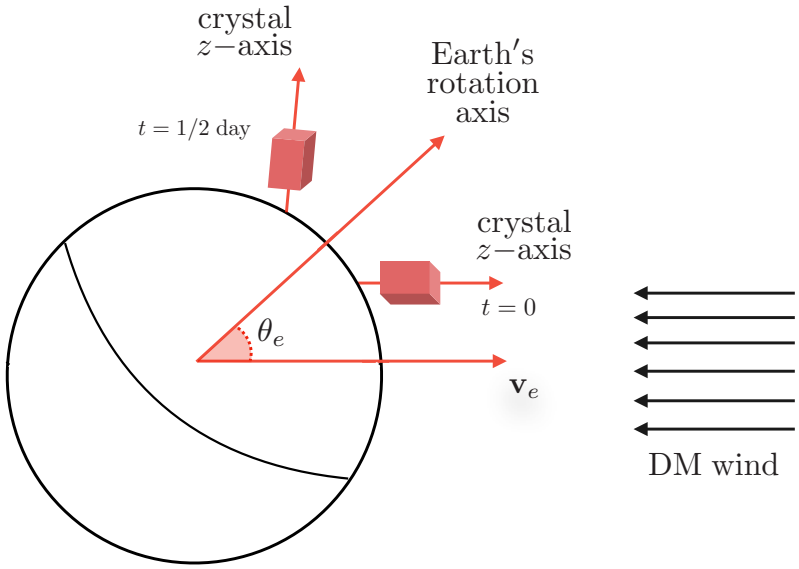

Figure 4.1: Orientation setup of the experimental apparatus. At $t = 0$ the z-axis of the crystal is aligned with the Earth's velocity (which is approximately in the direction of Cygnus). With this choice for the crystal orientation, the modulation of the signal is independent of the position of the laboratory.

The velocity distribution in the laboratory frame is related to the one in the galactic frame by $f_{\rm lab}(\mathbf{v}, t) = f_{\rm gal}(\mathbf{v} + \mathbf{v}_e(t))$:

$$f_{\rm lab}(\mathbf{v}, t) = \frac{1}{N_0} \exp\left[-\frac{(\mathbf{v} + \mathbf{v}_e)^2}{v_0^2}\right] \quad \Theta(v_{\rm esc} - |\mathbf{v} + \mathbf{v}_e|)\,, \tag{4.15}$$

where $\mathbf{v}_e(t)$ is the Earth's velocity with respect to the DM rest frame due to its revolution around the Sun and N_0 is a normalization constant given by

$$N_0 = \pi^{3/2} v_0^3 \left[\mathrm{erf}\left(\frac{v_{\rm esc}}{v_0}\right) - \frac{2}{\sqrt{\pi}} \frac{v_{\rm esc}}{v_0} \exp\left(-\frac{v_{\rm esc}^2}{v_0^2}\right)\right]. \tag{4.16}$$

The net effect of the Earth's revolution is to induce a DM wind oriented in the opposite direction of $\mathbf{v}_e$ in the laboratory reference frame. The orientation of $\mathbf{v}_e$, and therefore of the DM wind, relative to the crystal changes due to the rotation of the Earth. Choosing the crystal orientation such that at $t = 0$ the z-axis in the crystal frame is aligned with the Earth's velocity the explicit form of $\mathbf{v}_e$ is:

$$\mathbf{v}_e = |\mathbf{v}_e| \begin{pmatrix} \sin\theta_e \sin\phi \\ \sin\theta_e \cos\theta_e \,(\cos\phi - 1) \\ \cos^2\theta_e + \sin^2\theta_e \cos\phi \end{pmatrix} \tag{4.17}$$

Parameter	Value for $ZrTe_5$ (th.)	Value for $ZrTe_5$ (exp.)
$\mathrm{Re}(\boldsymbol{\epsilon}_{xx},\, \boldsymbol{\epsilon}_{yy},\, \boldsymbol{\epsilon}_{zz})$	(187.5, 9.8, 90.9)	
$(v_{F,x},\, v_{F,y},\, v_{F,z})$	$(2.9,\, 0.5,\, 2.1)\cdot 10^{-3}$	$(1.3,\, 0.65,\, 1.6)\cdot 10^{-3}$
Δ	2.5 meV	11.75 meV
Λ	0.14 keV	
g	4	
V_{uc}	795Å^3	
ρ_T	$6.1\,\mathrm{g/\,cm^3}$	
n_e	$8.3\times 10^{23}\ e^-/\mathrm{kg}$	

Table 4.1: Theoretical and experimental values of the material parameters for $ZrTe_5$ [88]. Specifically, we report the values of the dielectric tensor components, $\boldsymbol{\epsilon}_{ii}$, the Fermi velocity components, $v_{F,i}$, the band gap, Δ, the momentum cut-off, Λ, the product of Dirac cone and spin degeneracies, g, the volume of the unit cell, V_{uc}, the target density, ρ_T, and the valence electron density, n_e. Theoretical (experimental) values are used for the curves labeled "th" ("exp") in plots throughout this chapter. Some of the parameters are very sensitive to material engineering [157], for those we do not repot an experimental value and use the theoretical value instead.

where $|\mathbf{v}_e| \approx 240\,\mathrm{Km/\,s}$, $\phi = 2\pi \times t/24\,\mathrm{h}$ is the angle parametrizing the rotation of the Earth around its axis and $\theta_e \approx 42^\circ$ is the angle between the Earth's rotation axis and the direction of its velocity (see Fig. 4.1 for an illustration of the orientation setup).

4.4 Absorption in Anisotropic Dirac Materials

The DM absorption rate per unit time and detector mass is given by:

$$R_{abs} = \int d^3\mathbf{v}\, f_{\mathrm{lab}}(\mathbf{v}, t) R_{abs}(\omega, \mathbf{q}) \tag{4.18}$$

where $f_{\mathrm{lab}}(\mathbf{v}, t)$ is the DM velocity distribution in the laboratory frame, as defined in the previous section, and $R_{abs}(\omega, \mathbf{q})$ is the DM absorption rate at fixed energy and momentum transfer:

$$R_{abs}(\omega, \mathbf{q}) = \frac{1}{\rho_T}\frac{\rho_\chi}{m_\chi}\langle n_T \sigma_{\mathrm{abs}} v_{\mathrm{rel}}\rangle_{\mathrm{DM}}\,, \tag{4.19}$$

where ρ_T is the mass density of the target, n_T the number of target particles, $\sigma_{\mathrm{abs}}(\omega, \mathbf{q})$ the cross section for DM absorption by the target and v_{rel} the relative velocity between the target and the DM. For DM absorption, the energy transfer is uniquely fixed by the DM mass ($\omega = m_\chi$) and the momentum transfer is equal to the DM momentum ($\mathbf{q} = m_\chi \mathbf{v}$).

To derive the absorption rate of dark photons we start by considering the one of ordinary photons. This is related to the optical properties of the medium through the optical theorem:

$$\langle n_T \sigma_{\rm abs} v_{\rm rel} \rangle_{\gamma_i} = \frac{1}{\omega} {\rm Im}\Big[(\epsilon_i^\mu)^* \, \Pi_{\mu\nu} \, \epsilon_i^\nu \Big] = -\frac{1}{\omega} {\rm Im}\Big[\pi_i(q)\Big] \tag{4.20}$$

where ϵ_i^μ are the polarization vectors that diagonalize the polarization tensor and $\pi_i(q)$ the corresponding eigenvalues (as discussed in Sec. 4.2). From Eq. 4.11, we see that the effective mixing between ordinary and dark photons is given by

$$\varepsilon_{{\rm eff},i}^2 = \frac{\varepsilon^2 m_{A'}^4}{\left[m_{A'}^2 - {\rm Re}\,\pi_i(q)\right]^2 + \left[{\rm Im}\,\pi_i(q)\right]^2} \tag{4.21}$$

and so the dark photon absorption rate at fixed energy and momentum transfer reads

$$R_{\rm abs}^{A'}(\omega, \mathbf{q}) = -\frac{1}{3}\frac{\rho_\chi}{\rho_T} \sum_{i=1}^{3} \varepsilon_{{\rm eff},i}^2 \frac{{\rm Im}\,\pi_i(q)}{\omega^2} \,, \tag{4.22}$$

where the 1/3 comes from the average over the three dark photon polarizations that are assumed to be equally populated. The functional form of π_i, for the absorption limit ($\omega \gg |\mathbf{q}|$), can be computed for a specific orientation of $\mathbf{q}$. This is possible because the mixing matrices, $\mathcal{K}$ and $\mathcal{K}'$, for two different orientations of the momentum transfer, $\mathbf{q}$ and $\mathbf{q}'$, are related by a similarity transformation (*i.e.* $\mathcal{K}' = R^T \mathcal{K} R$ where R is a 3-by-3 matrix such that $\mathbf{q}' = R\mathbf{q}$) and therefore have the same eigenvalues. Hence, choosing for example $\mathbf{q} \parallel \hat{z}$, we find that the functional form of the three π_i for the absorption case is given by:

$$\pi_i = \omega^2 (1 - \boldsymbol{\epsilon}_{ii}) \,, \tag{4.23}$$

which allows us to write the absorption rate as

$$R_{\rm abs}^{A'}(\omega, \mathbf{q}) = \frac{\varepsilon^2}{3}\frac{\rho_\chi}{\rho_T} \sum_{i=1}^{3} \frac{{\rm Im}[\boldsymbol{\epsilon}_{ii}]}{{\rm Re}[\boldsymbol{\epsilon}_{ii}]^2 + {\rm Im}[\boldsymbol{\epsilon}_{ii}]^2} \,. \tag{4.24}$$

As discussed in Appendix D, since for $\omega \lesssim \Lambda v_F$ the imaginary part of the dielectric receives contributions only from excitations close to the Dirac point, ${\rm Im}[\boldsymbol{\epsilon}]$ can be computed using the analytic electron wave functions provided in [88]. For what concerns the real part, we need to resort to a DFT calculation whose results are shown in Table 4.1. Note this is in contrast to Refs. [88] and [152] which used an analytic calculation of the real part of $\boldsymbol{\epsilon}$ to determine the rate. This underestimates $\boldsymbol{\epsilon}$ because the analytic calculation, including only states near the Dirac point, does not give the contribution of the full electronic response. In Fig. 4.2 we show the projected reach for a $ZrTe_5$ target with a gap of 2.5 meV and 7.5 meV, and we compare it with the reach of polar materials [82], superconducting [118] and semiconducting targets [158]. The Dirac material reach shown here is almost one order of magnitude smaller than previously claimed in references [88] and [152] because of their underestimate of $\boldsymbol{\epsilon}$. We summarize in more detail in Appendix D.1 the differences between the present calculation and those that appeared previously.

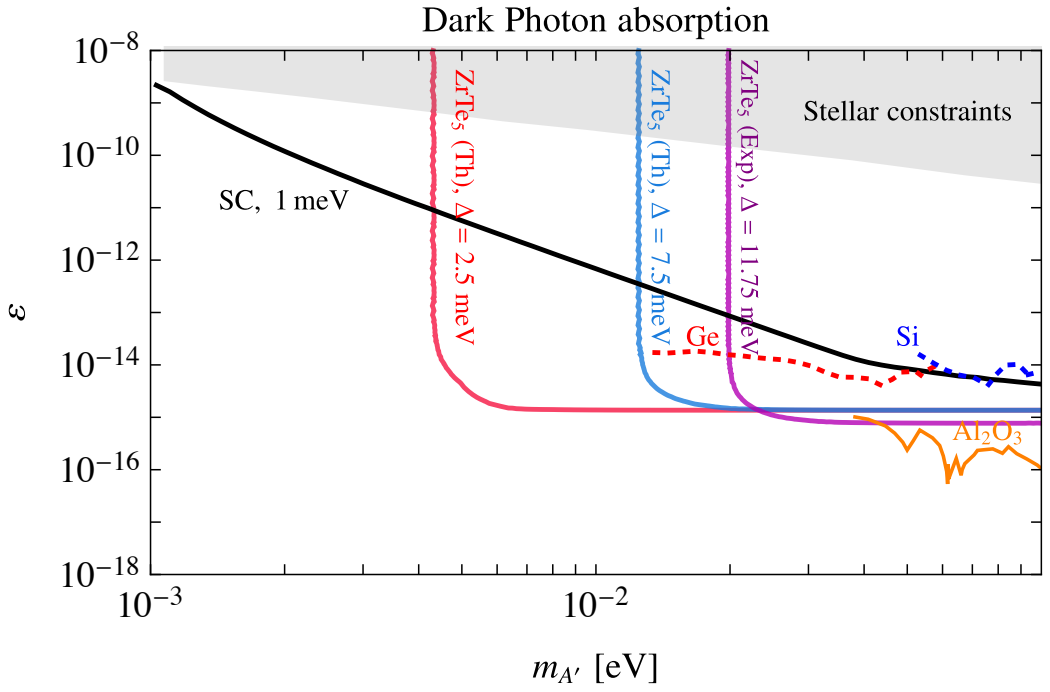

Figure 4.2: Projected reach for the absorption of a kinetically mixed dark photon with a kinetic mixing parameter ε and a mass $m_{A'}$. We show the 95% C.L. sensitivity (3 events) that can be obtained with 1 kg-year exposure of a Dirac material with the properties of $ZrTe_5$ shown in Table 4.1 but with a band gap of 2.5 meV (solid red), 7.5 meV (solid blue), or 11.75 meV (solid purple). For comparison we also show the sensitivity of a superconductor (SC) with a 1 meV threshold (black line) [118], sapphire (Al_2O_3) with a 1 meV threshold (orange) representative for polar materials [82], and two-phonon excitations in germanium (dotted red) and silicon (dotted blue) semiconductors [158]. The gray shaded region is excluded by stellar emission constraints [159, 160]. The plot is cut at $m_{A'} = 10^{-1}$ eV, which is the largest energy deposit consistent with the linear energy dispersion relation.

4.5 Scattering in Anisotropic Dirac Materials

We will characterize the dark matter interaction rate in terms of the target response (the so-called dynamic structure factor $S(q,\omega)$), the dark matter velocity phase space characterized by the DM velocity distribution $f_{\rm gal}(\vec{v})$, and the nature of the mediator (massless or massive). Then we have the rate to scatter from the valence band of the crystal ($-$, momentum $\mathbf{k}$) to the conduction band ($+$, momentum $\mathbf{k}'$) given by [84]

$$R_{\mathbf{k},\mathbf{k}'} = \frac{1}{\rho_T}\frac{\rho_\chi}{m_\chi}\frac{\pi\bar{\sigma}_e}{\mu_{\chi e}^2}\int\frac{d^3\mathbf{q}}{(2\pi)^3}\int d^3\mathbf{v}\, f_{\rm lab}(\mathbf{v})\; F_{\rm med}(q)^2 S(\mathbf{q},\omega), \tag{4.25}$$

where $\mu_{\chi e}$ is the DM-electron reduced mass,

$$\omega = \frac{1}{2}m_\chi v^2 - \frac{(m_\chi \mathbf{v} - \mathbf{q})^2}{2m_\chi} = \mathbf{q}\cdot\mathbf{v} - \frac{\mathbf{q}^2}{2m_\chi} \tag{4.26}$$

is the energy deposition, and the dynamic structure factor $S(\mathbf{q},\omega)$ is

$$S(\mathbf{q},\omega) = 2\pi\left(\frac{\mathbf{q}^2}{|\mathbf{q}\cdot\boldsymbol{\epsilon}\cdot\mathbf{q}|}\right)^2 \frac{1}{2}\frac{(2\pi)^3}{V}\left(1 - \frac{\tilde{\mathbf{k}}\cdot\tilde{\mathbf{k}}'}{|\tilde{\mathbf{k}}||\tilde{\mathbf{k}}'|}\right)\delta^3(\mathbf{q} - (\mathbf{k}' - \mathbf{k}))\delta(\Delta E_{\mathbf{k},\mathbf{k}'} - \omega)\,, \tag{4.27}$$

where V is the volume of the crystal. The energy splitting from valence to conduction band near the Dirac point is

$$\Delta E_{\mathbf{k},\mathbf{k}'} = \sqrt{\tilde{\mathbf{k}}^2 + \Delta^2} + \sqrt{\tilde{\mathbf{k}}'^2 + \Delta^2} = \sqrt{\tilde{\mathbf{k}}^2 + \Delta^2} + \sqrt{(\tilde{\mathbf{k}} + \tilde{\mathbf{q}})^2 + \Delta^2}\,, \tag{4.28}$$

with $\tilde{\mathbf{k}} = (v_{Fx}k_x, v_{Fy}k_y, v_{Fz}k_z)$.

We utilize a convention where $\bar{\sigma}_e$ is the fiducial cross-section

$$\bar{\sigma}_e = \frac{16\pi\mu_{\chi e}^2\varepsilon^2\alpha_{\rm EM}\alpha_{\rm D}}{q_0^4}, \tag{4.29}$$

and $F_{\rm med}(|\mathbf{q}|)$ incorporates the momentum dependence in the scattering cross-section,

$$F_{\rm med}(|\mathbf{q}|) = q_0^2/|\mathbf{q}|^2, \quad q_0 = \alpha m_e. \tag{4.30}$$

Because ω depends on $\mathbf{q}\cdot\mathbf{v}$, the energy conserving delta function can be used to evaluate the velocity integral as proposed in Ref. [82]:

$$\int d^3v f_{\rm lab}(\mathbf{v})\delta(\Delta E - \omega) = \frac{\pi v_0^2}{N_0|\mathbf{q}|}\left[\exp(-v_-^2/v_0^2) - \exp(-v_{\rm esc}^2/v_0^2)\right] \equiv g(\mathbf{q},\Delta E_{\mathbf{k},\mathbf{k}'}), \tag{4.31}$$

where N_0 is a normalization constant defined in Eq. 4.16, and

$$v_- = \min\left\{\left|\frac{\mathbf{q}\cdot\mathbf{v}_e + \mathbf{q}^2/2m_\chi + \Delta E}{|\mathbf{q}|}\right|, v_{\rm esc}\right\} \tag{4.32}$$

is the minimum velocity (in the galactic reference frame) that a DM particle should have to induce a scattering with energy deposition ΔE and momentum transfer $\mathbf{q}$. To obtain the total rate, $R_{-,\mathbf{k}\to+,\mathbf{k}'}$ is summed over initial and final state BZ momenta, over a region of size Λ near the Dirac point

$$R_{\rm crystal} = g_s V^2\int_{\rm BZ}\frac{d^3\mathbf{k}d^3\mathbf{k}'}{(2\pi)^6}R_{-,\mathbf{k}\to+,\mathbf{k}'} = g_s g_C V^2\int_{\rm cone}\frac{d^3\mathbf{k}d^3\mathbf{k}'}{(2\pi)^6}R_{\mathbf{k},\mathbf{k}'}\,. \tag{4.33}$$

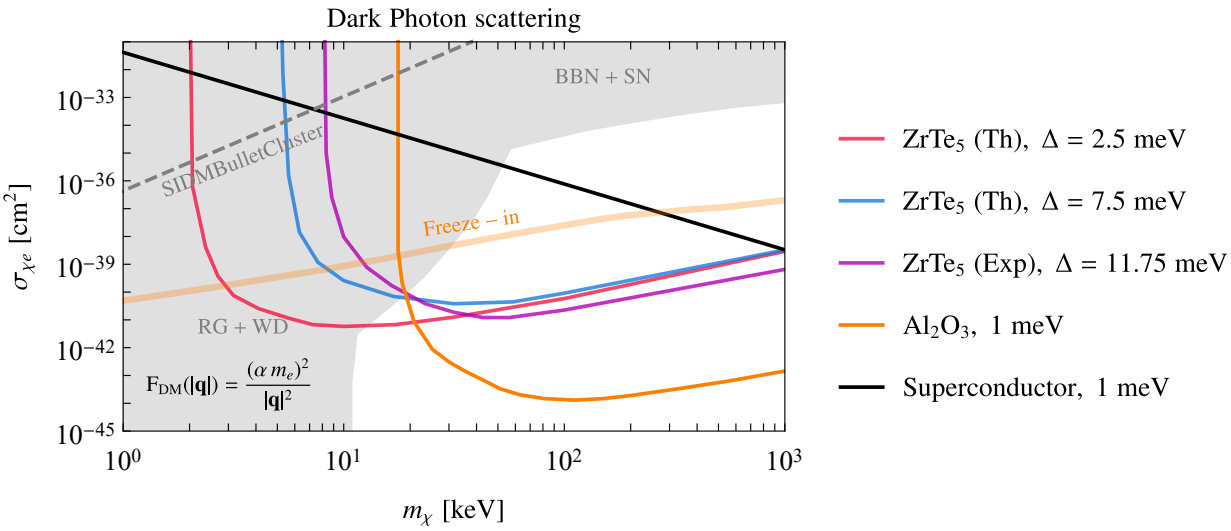

Figure 4.3: Projected reach of dark matter scattering in Dirac material for a background-free 95% C.L. sensitivity (3 events) assuming a 1 kg-year exposure of $ZrTe_5$ with band gaps of 2.5 meV (red line), 7.5 meV (blue line) and 11.75 meV (purple line). For $ZrTe_5$ curves, "Th" indicates the use of theoretical parameters, and "Exp" indicates the use of experimental parameters (See Table 4.1). For comparison, we show the respective reaches of superconductors with a 1 meV threshold (black line) [118] and sapphire (Al_2O_3) with a 1 meV threshold (orange line) [81]. The thick orange line indicates the region of parameter space where the freeze-in production results in the correct dark matter relic abundance, as computed in Ref. [142]. Shaded regions are bounds from red giants (RG), white dwarfs (WD), big bang nucleosynthesis (BBN) and supernovae (SN), and are derived from millicharged particle limits [84, 161]. The dashed line is the self interacting dark matter bound derived from observations of the Bullet Cluster [162].

The scattering rate per unit time per unit detector mass is then given by

$$R = \frac{\rho_\chi}{m_\chi}\frac{\pi\overline{\sigma_e}}{\mu_{\chi e}^2}\int\frac{d^3\mathbf{q}}{(2\pi)^3}\int\frac{d^3\mathbf{k}}{(2\pi)^3}F_{\rm med}(\mathbf{q})^2\,|\langle f|F_T|i\rangle|^2\,g(\mathbf{q},\Delta E_{\mathbf{k},\mathbf{k}'}) \tag{4.34}$$

with

$$|\langle f|F_T|i\rangle|^2 = \pi g\; n_e V_{\rm uc}\underbrace{\left(\frac{\mathbf{q}^2}{|\mathbf{q}\cdot\boldsymbol{\epsilon}\cdot\mathbf{q}|}\right)^2}_{\epsilon\text{-factor}}\times\underbrace{\left(1-\frac{\tilde{\mathbf{k}}\cdot(\tilde{\mathbf{k}}+\tilde{\mathbf{q}})}{|\tilde{\mathbf{k}}||\tilde{\mathbf{k}}+\tilde{\mathbf{q}}|}\right)}_{\text{WF-factor}}, \tag{4.35}$$

where $V_{\rm uc}$ is the volume of the unit cell, n_e is the electron density, and $g = g_s g_C$ is the

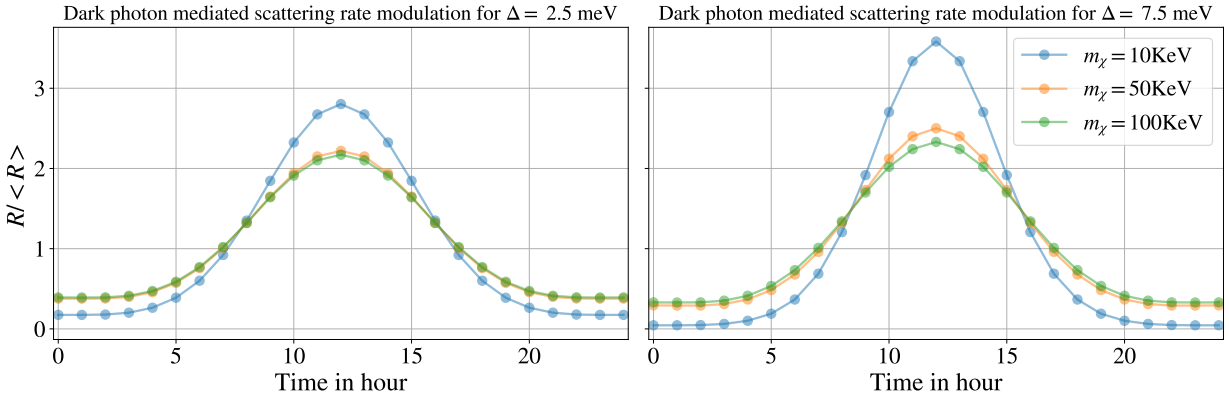

Figure 4.4: Daily modulation of the dark photon mediated scattering rate for $ZrTe_5$ (using theoretical parameters, see Table 4.1) with a band gap of 2.5 meV (left panel) and 7.5 meV (right panel) for three different dark matter masses.

product of Dirac cone and spin degeneracies. For future convenience, we labeled two factors in the Matrix Element $\sum_f |\langle f|F_T|i\rangle|^2$ as ϵ and WF factors respectively.

In Fig. 4.3 we show the projected reach for a $ZrTe_5$ target with gap values of 2.5 meV, 7.5 meV and 11.75 meV, and we compare it with the one of a superconducting target with 1 meV threshold [163]. Because of the large in medium screening of superconductors [87, 118] compared to the Dirac Materials, Dirac Materials are far superior in reach. By contrast, polar materials [81] have a better reach. Note that our results again differ from those presented in [88] and [152], where the dielectric constant was underestimated by an order of magnitude leading to an $\mathcal{O}(10^2)$ larger rate; a more detailed discussion of the differences between the present calculation and previous works is given in Appendix D.1.

In Fig. 4.4 we report the daily modulation of the scattering rate for $ZrTe_5$ for different mass and threshold values. We observe that daily modulation increases for higher masses and thresholds. Also, the rate is maximized around $t = 1/2$ day when the DM wind point along the smallest component of the dielectric tensor. The reason for these behaviors is discussed in detail next.

Origin of the daily modulation

The crystal anisotropies and the Earth's motion single out two preferred directions for the momentum transfer. The relative orientation of these directions changes during the day because of Earth's rotation giving rise to a daily modulation. Specifically, when these two directions coincide we have a maximum of the scattering rate and vice versa.

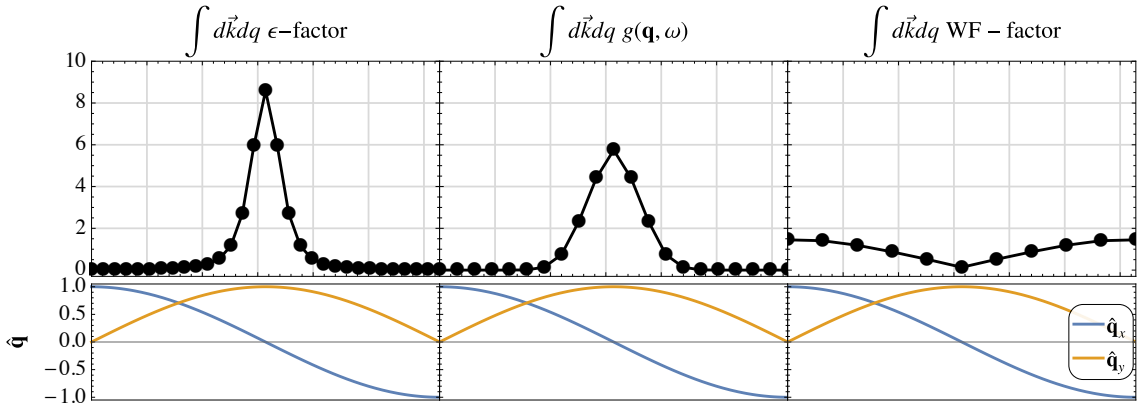

Figure 4.5: Modulation of the the different terms appearing in (4.34). Specifically, we show the integrated values of the ϵ-factor (left panel), kinematic term (central panel), and WF-factor (right panel) for different orientation of $\mathbf{q}$ in the x-y plane (which is the one presenting the largest anisotropies). The reported values (which are normalized to its average value) are obtained by taking $m_\chi = 50\,\text{keV}$, $\Delta = 2.5\,\text{meV}$, and integrating over the magnitude of $\mathbf{q}$. To disentangle the effect of crystal anisotropies and Earth motion in the kinematic term, we have varied the orientation of $\mathbf{q}$ while keeping the angle between $\mathbf{q}$ and the Earth velocity fixed.

Crystal anisotropies affect the rate in two ways. First, they appear through the anisotropy in the Fermi velocity; the kinematics prefers the momentum transfer to be anti-aligned with the direction of the smallest Fermi velocity in order to increase the available phase space. We refer to this as a kinematic effect. And second they affect the magnitude of the scattering matrix element, $|\langle f|F_T|i\rangle|$, through the so-called ϵ and "WF" factors labeled in Eq. 4.35. We now discuss the preferred direction singled out by each one of these two elements together with the Earth motion.

Anisotropies in Kinematics

The kinematics of the scattering is sensitive to anisotropies in the Fermi velocity due to the rescaled momenta $\tilde{\mathbf{k}}$ and $\tilde{\mathbf{q}}$ that appear in $\Delta E_{\mathbf{k},\mathbf{k}'}$. From Eq. 4.28 we can see that, for a given $\mathbf{k}$, the energy transfer is minimized when $\mathbf{q}$ is aligned with the smallest component of the Fermi velocity. Therefore, when $\mathbf{q}$ points in this direction, a larger fraction of momenta in the BZ is kinematically allowed, so that the rate is maximized (as shown in the central panel of Fig. 4.5).

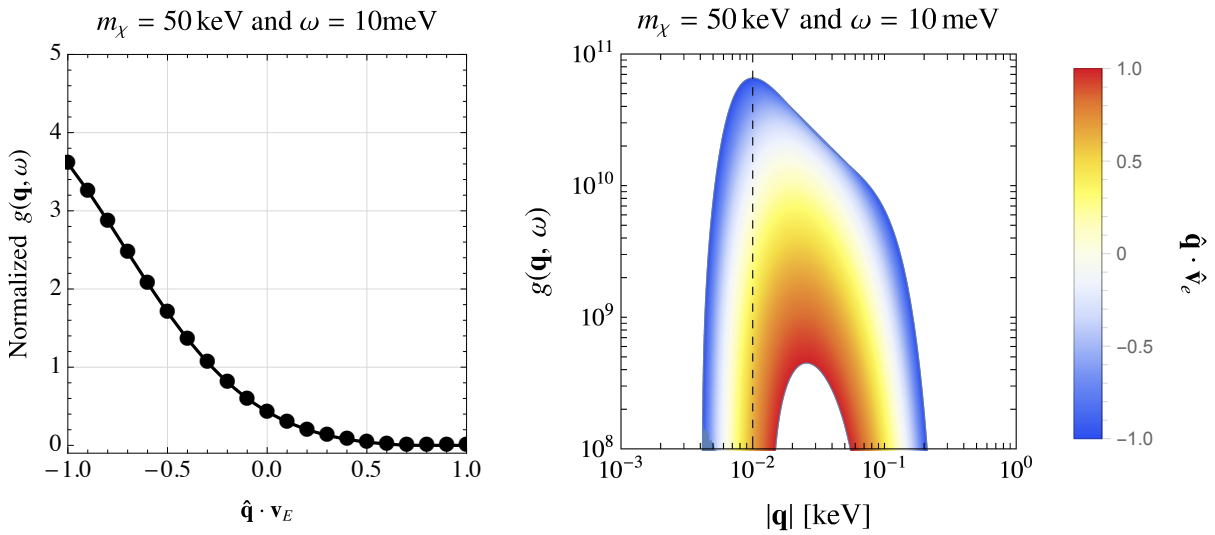

Figure 4.6: **Left**: Value of the kinematic factor $g(\mathbf{q}, \Delta E)$ (normalized to its average value) for different values of $\mathbf{q}\cdot\mathbf{v}_e$ and a fixed value of $|\mathbf{q}|$. **Right**: kinematic factor $g(\mathbf{q}, \Delta E)$ for different values of $|\mathbf{q}|$ and $\mathbf{q}\cdot\mathbf{v}_e$. The dashed line indicates the value of $|\mathbf{q}|$ assumed in the left panel.

Anisotropies in the Matrix Element

The scattering matrix element is sensitive to anisotropies in both the band structure and the dielectric tensor. To understand the modulation induced by the matrix element it is useful to deconstruct the impact on the matrix element in terms of the ϵ and WF factors defined in Eq. 4.35.

Crystal anisotropies enter in the ϵ-factor thorough the tensorial structure of $\boldsymbol{\epsilon}$. Namely, the ϵ-factor is maximized when $\mathbf{q}$ points in the direction of the smallest component of the dielectric tensor (as shown in the left panel of Fig. 4.5).

The WF-factor is sensitive to anisotropies in the band structure of the crystal through the rescaled momentum transfer $\tilde{\mathbf{q}}$. The WF-factor grows by increasing the angle between $\tilde{\mathbf{q}}$ and $\tilde{\mathbf{q}} + \tilde{\mathbf{k}}$. This angle is non-zero when $\tilde{\mathbf{q}}$ gives a sizable contribution to the sum $\tilde{\mathbf{q}} + \tilde{\mathbf{k}}$. The fraction of the kinematically allowed $\mathbf{q}$ that satisfies this requirement grows when the momentum transfer is aligned with the largest component of the Fermi velocity, given that this maximized the rescaled momenta $\tilde{\mathbf{q}}$. The WF-factor is maximized (minimized) when the momentum transfer points along the direction with the highest (smallest) Fermi velocity, as shown in the right panel of Fig. 4.5.

Earth motion

The Earth's motion picks out a preferred direction for $\mathbf{q}$ through the minimum velocity, v_-, appearing in the velocity phase space integral Eq. 4.32. A smaller minimum velocity corresponds to a larger available phase space, and hence a larger $g(\mathbf{q}, \Delta E_{\mathbf{k},\mathbf{k}'})$ and a larger rate. As shown in Fig. 4.6, this function is maximized when $\mathbf{q}$ is antiparallel to $\mathbf{v}_e(t)$.

We now have all the ingredients to understand the daily modulation shown in Fig. 4.4. Because of the large anisotropies in the ϵ-factor (see Fig. 4.5), the rate is dominated by momentum transfers along the y-direction, corresponding to the smallest component of the dielectric tensor. Therefore, the average value of the scattering rate is approximately given by fixing $\mathbf{q} \parallel \hat{y}$ in the integrand of Eq. (4.34). A daily modulation around this average value is induced by the rotation of the Earth via the kinetic term. This term reaches is maximum when the Earth velocity is antiparallel to $\mathbf{q}$ (see Fig. 4.6). Because of this, the scattering rate is maximized at $t = 1/2$ day, when the Earth velocity is aligned with the y-axes.

4.6 Conclusions

Dirac materials, due to their small band gap, are promising targets to look for scatterings and absorption of light dark matter. In this work we discussed how crystal anisotropies can give rise to a daily modulation of the DM interaction rate with a Dirac material.

To this end, we generalized the discussion of Ref. [88] to accurately take into account anisotropies of the crystal structure, which induce a mixing of the longitudinal and transverse dark photon polarizations during their propagation in the media. We then applied these results to the specific case of the Dirac material $ZrTe_5$ finding no modulation for the absorption signal and a daily modulation of $\mathcal{O}(1)$ for the scattering signal (see Fig. 4.4). In Fig. 4.2 (Fig. 4.3) we also provide new projected reach for the absorption (scattering) signal, which is one (two) orders of magnitude weaker in comparison to Refs. [88] and [152]. This discrepancy, as discussed in Appendix D.1, is due to an incorrect prescription for incorporating the dielectric tensor, which underestimated the impact of in-medium screening.

Since, for the scattering signal, the shape of the modulation depends on the orientation of the crystal with respect to the dark matter wind, modulation effects can be used to validate any putative dark matter signal simply by changing the orientation of the crystal and observing a change in the shape of the modulation. Finally, we notice that the modulation amplitude seems to depend on the DM mass. However, further studies are needed to establish whether or not this feature can be used to infer the value of the DM mass in the case of a definitive observation of the modulation signal.

Chapter 5

Directional Detectability of Dark Matter With Single Phonon Excitations: Target Comparison

5.1 Introduction

If the cold dark matter (DM) in the universe consists of new particles, they must interact very weakly with the Standard Model. Directly detecting these feeble interactions in a laboratory requires extraordinarily sensitive devices. Traditional direct detection experiments (*e.g.* ANAIS [164], CRESST [165–167], DAMA/LIBRA [168], DAMIC [169], DarkSide-50 [170], DM-Ice [171], KIMS [172], LUX [173, 174], SABRE [175], SuperCDMS [151, 176], and Xenon1T [177]), based on nuclear recoil, are gradually improving their sensitivity and closing the open parameter space before reaching the irreducible solar and atmospheric neutrino background. However, these experiments are fundamentally limited in the DM mass, m_χ, they can probe. When the DM scatters off a nucleus at rest, the energy deposited, ω, is limited by $\omega \lesssim m_\chi^2 v^2/m_N$, with $v \sim 10^{-3}$, and vanishes quickly as the DM mass decreases below the nucleus mass m_N.

This limitation in DM mass is typically not problematic in the search for the prototypical weakly interacting massive particle (WIMP) which produces the DM abundance through freeze-out, as $m_\chi \lesssim$ GeV would both be overabundant and be in tension with indirect detection bounds on DM annihilation rates. However, many other theoretically motivated explanations of the origin of DM such as freeze-in [140, 178], hidden sector DM [56, 137–139], asymmetric DM [59, 61, 136, 179], and strong self interactions [60, 180], allow for DM ligher than a GeV and therefore should be searched for by means other than nuclear recoil.

In the pursuit of sub-GeV DM, several new experimental concepts have been proposed. These include electron excitations in a variety of target systems [83–86, 124, 130, 143, 181–186] for DM with mass above an MeV, while single (primary) phonon excitations [79–82, 187–197], with energies up to $\mathcal{O}(100)$ meV, have been shown to be especially sensitive to

a wide range of DM models with masses down to a keV. This coupled with the fact that detector energy thresholds are approaching the $\mathcal{O}(100)$ meV range [198–202] makes single phonon excitations an exciting avenue for DM direct detection. Phonons are quasiparticle vibration quanta which can exist in multiple states of matter, *e.g.* as sound waves in liquids or superfluids and lattice vibrations in crystalline solids. Superfluid helium has been proposed [79] and studied as a light DM detector [80, 187–190] and an experiment is currently in the R&D phase [203]. Crystal targets have also been proposed [81] and studied extensively. Initial studies focused on GaAs and Al_2O_3 (sapphire) targets [82], and more recently this analysis has been extended to account for more general DM interactions [191, 195] and applied to a broader set of target materials [192]. Other targets have also been proposed individually, *e.g.* SiC [194], and there has been work on understanding the signal from multi-phonon excitations [193, 196, 197]. Similar to superfluid helium, a DM detector using a crystal target with single phonon readout is also in the R&D phase of development [203].

Most of the previous work has focused on calculating the theoretically predicted DM-phonon interaction strength. Equally important is to minimize the experimental background [5]. This becomes easier when the DM scattering signal has unique properties which can distinguish it from backgrounds. For example, in experiments sensitive to nuclear recoil or electron excitations, the rate modulates annually due to the change in the DM velocity distribution in the Earth frame, as the Earth orbits around the Sun [84, 130, 204].

In an experiment based on primary phonon readout, the DM scattering rate can have a larger and more unique signature: *daily* modulation. As the Earth rotates about its own axis, the orientation of the detector relative to the DM wind changes. In a nuclear recoil experiment this does not have an effect since the interaction matrix element is independent of the direction of the DM velocity relative to the detector orientation — an (unpolarized) nucleus is isotropic in its response. However, crystal targets can be highly anisotropic, which means that the amplitude of the response depends not only on the magnitude of the momentum transfer but also on its direction. This can lead to a significant daily modulation. Moreover, since the modulation pattern depends on the crystal orientation, running an experiment with multiple detectors simultaneously with different orientations can further enhance the signal-to-noise ratio. This effect was studied for sapphire in Ref. [82] (see also Refs. [7, 85, 152, 191] for discussions of daily modulation in electron excitations). In this work, we expand the understanding of the daily modulation effect in single phonon excitations to a broader range of materials, including those targeted in Ref. [192].

In particular, we highlight the following targets in the main text: Al_2O_3 (sapphire) and $CaWO_4$, already utilized for DM detection and have a significant daily modulation; SiO_2, shown to have a strong reach to several benchmark models; SiC, proposed in Ref. [194] (for which we choose the commercially available 4H polytype); and h-BN (hexagonal boron nitride), a highly anisotropic material. Among them, Al_2O_3 and $CaWO_4$ have the best prospects overall in terms of daily modulation reach and experimental feasibility.

Of the additional materials considered in Ref. [192], results for those with daily modulation larger than 1% (for at least some DM masses) are presented in an appendix. We

make available our code for the phonon rate calculation [205], and also publish an interactive webpage [206] where results for all the materials presented Ref. [192] and in this chapter, including reach curves, differential rates and daily modulation patterns, can be generated from our calculations. Twenty-six materials are initially included on the interactive webpage [206]: Al_2O_3, AlN, h-BN, CaF_2, $CaWO_4$, CsI, C (diamond), GaAs, Ge, GaN, GaSb, InSb, LiF, MgF_2, MgO, NaCl, NaF, NaI, PbS, PbSe, PbTe, Si, 4H-SiC, SiO_2, ZnO, and ZnS. This diverse set of materials (with some currently in use in nuclear recoil experiments, some proposed for light dark matter detection, and some others being promising polar crystals from theoretical considerations) aims to explore a wide range of possibilities with the hope of identifying broad theoretical features that could be implemented in a more practical experimental setup. Materials shown in-text (Al_2O_3, SiO_2, SiC, $CaWO_4$ and h-BN) are the ones with the highest daily modulation in this list.

5.2 Directional Detection With Single Phonon Excitations

Excitation Rate

We begin by summarizing the formulae for single phonon excitation rates; see Refs. [81, 82, 191] for more details. For the scattering of a DM particle χ with mass m_χ and general spin-independent interactions, the rate per unit target mass takes the form

$$R(t) = \frac{1}{\rho_T}\frac{\rho_\chi}{m_\chi} \quad \frac{\pi\overline{\sigma}_\psi}{\mu_{\chi\psi}^2}\int d^3v\, f_\chi(\boldsymbol{v},t) \times \int \frac{d^3q}{(2\pi)^3}\, F_{\rm med}^2(q)\, S\big(\boldsymbol{q},\omega_{\boldsymbol{q}}\big)\,, \tag{5.1}$$

where $\boldsymbol{v}$ is the incoming DM's velocity, $\boldsymbol{q}$ is the momentum transferred to the target, ρ_T is the target's mass density, and $\rho_\chi = 0.4\,\mathrm{GeV/cm^3}$ is the local DM density. $\overline{\sigma}_\psi$, with $\psi = n$ or e (neutron or electron), is a reference cross section defined as

$$\overline{\sigma}_\psi \equiv \frac{\mu_{\chi\psi}^2}{\pi}\overline{|\mathcal{M}_{\chi\psi}(q=q_0)|^2}\,, \tag{5.2}$$

where $\mu_{\chi\psi}$ is the reduced mass, $\mathcal{M}_{\chi\psi}$ is the vacuum matrix element for $\chi\psi\to\chi\psi$ scattering, and q_0 is a reference momentum transfer. We present the reach in terms of $\overline{\sigma}_\psi$, with $q_0 = m_\chi v_0$ (where $v_0 = 230\,\mathrm{km/s}$, the dispersion of DM's velocity distribution) for $\psi = n$ and $q_0 = \alpha m_e$ for $\psi = e$. $f_\chi(\boldsymbol{v},t)$ is the DM's velocity distribution in the lab frame, taken to be a truncated Maxwell-Boltzmann distribution, boosted by the time-dependent Earth velocity $\boldsymbol{v}_{\rm e}(t)$, as will be discussed in more detail in the next subsection. $F_{\rm med}(q)$ is the mediator form factor, which captures the q dependence of the mediator propagator:

$$F_{\rm med}(q) = \begin{cases} 1 & (\text{heavy mediator})\,, \\ (q_0/q)^2 & (\text{light mediator})\,. \end{cases} \tag{5.3}$$

Finally, $S(\boldsymbol{q},\omega)$ is the dynamic structure factor that encodes target response to DM scattering with momentum transfer $\boldsymbol{q}$ and energy transfer ω, constrained by energy-momentum conservation to be

$$\omega_{\boldsymbol{q}} = \boldsymbol{q}\cdot\boldsymbol{v} - \frac{q^2}{2m_\chi}\,. \tag{5.4}$$

Generally, one sums over a set of final states f with energies ω_f, and $S(\boldsymbol{q},\omega)$ takes the form

$$S(\boldsymbol{q},\omega) = \sum_f 2\pi\,\delta(\omega-\omega_f)\,S'_f(\boldsymbol{q})\,. \tag{5.5}$$

For single phonon excitations, we assume the target system is initially prepared in the ground state at zero temperature with no phonons, and sum over single phonon states labeled by branch ν and momentum $\boldsymbol{k}$ inside the first Brillouin zone (1BZ). Lattice momentum conservation dictates that $\boldsymbol{q} = \boldsymbol{k}+\boldsymbol{G}$, with $\boldsymbol{G}$ a reciprocal lattice vector. To find $\boldsymbol{k}$ and $\boldsymbol{G}$ from a given $\boldsymbol{q}$, we first find the reduced coordinates (q_1,q_2,q_3) (*i.e.* $\boldsymbol{q} = \sum_{i=1}^3 q_i\boldsymbol{b}_i$ with $\boldsymbol{b}_i$ the basis vectors of the reciprocal lattice), and then find the nearest point (G_1,G_2,G_3) with $G_i\in\mathbb{Z}$. In this way, any $\boldsymbol{q}$ outside of the 1BZ is mapped to a $\boldsymbol{k}$ inside the 1BZ and a $\boldsymbol{G}$ vector. The sum over final states therefore only runs over ν,

$$S(\boldsymbol{q},\omega) = \sum_\nu 2\pi\delta(\omega-\omega_{\nu,\boldsymbol{k}})\,S'_\nu(\boldsymbol{q})\,. \tag{5.6}$$

As was shown in Refs. [81, 82, 191], S'_ν can be written in terms of the phonon energies $\omega_{\nu\boldsymbol{k}}$, eigenvectors $\boldsymbol{\epsilon}_{\nu\boldsymbol{k}j}$ and an effective DM-ion couplings $\boldsymbol{Y}_j$ (with j labeling the ions in the primitive cell):

$$S'_\nu(\boldsymbol{q}) = \frac{1}{2\Omega\,\omega_{\nu,\boldsymbol{k}}}\left|\sum_j \frac{e^{-W_j(\boldsymbol{q})}}{\sqrt{m_j}}\,e^{i\boldsymbol{G}\cdot\boldsymbol{x}_j^0}\left(\boldsymbol{Y}_j\cdot\boldsymbol{\epsilon}^*_{\nu,\boldsymbol{k},j}\right)\right|^2, \tag{5.7}$$

where Ω is the volume of the primitive cell, and $m_j, \boldsymbol{x}_j^0$, and $W_j(\boldsymbol{q}) \equiv \frac{\Omega}{4m_j}\sum_\nu\int\frac{d^3k}{(2\pi)^3}\frac{|\boldsymbol{q}\cdot\boldsymbol{\epsilon}_{\nu,\boldsymbol{k},j}|^2}{\omega_{\nu,\boldsymbol{k}}}$ are the masses, equilibrium positions, and Debye-Waller factors of the ions, respectively. We obtain the material-specific force constants in the quadratic crystal potential and the equilibrium positions from density functional theory (DFT) calculations [82, 192, 207], and use the open-source phonon eigensystem solver `phonopy` [208] to derive the values of $\omega_{\nu,\boldsymbol{k}}$, $\boldsymbol{\epsilon}_{\nu,\boldsymbol{k},j}$ for each material.

The DM-ion coupling vectors $\boldsymbol{Y}_j$ are DM model dependent. In our target comparison study in Sec. 5.3, we will focus on two sets of benchmark models, with a light dark photon mediator and a heavy or light hadrophilic scalar mediator, respectively. These are the same models considered in Ref. [192], for which $\boldsymbol{Y}_j$ are given by

$$\boldsymbol{Y}_j = \begin{cases} -\dfrac{\boldsymbol{q}\cdot\boldsymbol{Z}_j^\star}{\hat{\boldsymbol{q}}\cdot\boldsymbol{\varepsilon}_\infty\cdot\hat{\boldsymbol{q}}} & \text{(dark photon med.)},\\[2ex] \boldsymbol{q}\,A_j\,F_{N_j}(q) & \text{(hadrophilic scalar med.)}. \end{cases} \tag{5.8}$$

Here $\boldsymbol{Z}_j^\star$ is the Born effective charge tensor of the j^{th} ion, $\boldsymbol{\varepsilon}_\infty$ is the high-frequency dielectric tensor that captures the electronic contribution to in-medium screening, A_j is the atomic mass number, and $F_{N_j}(q) = \frac{3\,j_1(qr_j)}{qr_j}\, e^{-(qs)^2/2}$ (with $r_j = 1.14\, A_j^{1/3}\,\text{fm}$, $s = 0.9\,\text{fm}$) is the Helm nuclear form factor [39] (which is close to unity for the DM masses considered in this work).

These benchmark models have highly complementary features. In a polar crystal, the dark photon couples to the Born effective charges of the ions, which have opposite signs within the primitive cell, and therefore dominantly induces out-of-phase oscillations corresponding to gapped optical phonon modes in the long-wavelength limit. By contrast, the hadrophilic scalar mediator couples to all ions with the same sign, and therefore dominantly excites gapless acoustic phonons that correspond to in-phase oscillations in the long-wavelength limit. There is also a difference between a light and heavy mediator due to the mediator form factor in Eq. (5.3). Noting that $\boldsymbol{Y}_j$ scales with q and the energy conserving delta function contributes a factor of q^{-1} (see Eq. (5.11) below), we see that for a heavy mediator, the integral scales as $\int dq\, q^3\omega^{-1}$ and so is always dominated by large q. For a light mediator, on the other hand, the integral scales as $\int dq\, q^{-1}\omega^{-1}$. So for optical phonons with $\omega \sim q^0$, it receives similar contributions from all q, whereas for acoustic phonons, it is dominated by small q where $\omega \sim q$.

Daily Modulation

In the rate formula Eq. (5.1), the time dependence comes from the DM's velocity distribution $f_\chi(\boldsymbol{v}, t)$, specifically via the Earth's velocity $\boldsymbol{v}_\text{e}(t)$ that boosts the distribution. Concretely, we take

$$f_\chi(\boldsymbol{v}, t) = \tfrac{1}{N_0} \exp\left[-\tfrac{(\boldsymbol{v}+\boldsymbol{v}_\text{e}(t))^2}{v_0^2}\right] \Theta\big(v_\text{esc} - |\boldsymbol{v} + \boldsymbol{v}_\text{e}(t)|\big)\,, \tag{5.9}$$

where N_0 is a normalization constant such that $\int d^3v\, f_\chi(\boldsymbol{v}) = 1$, $v_\text{esc} = 600$ km/s is the galactic escape velocity, and $v_0 = 230\,\text{km/s}$ as mentioned above. Assuming the detector is fixed on the Earth, in the lab frame $\boldsymbol{v}_\text{e}$ becomes a function of time that is approximately periodic over a sidereal day as a result of the Earth's rotation. As a default setup, we adopt the detector orientation in Refs. [7, 82, 191], for which, independent of the detector's location,

$$\boldsymbol{v}_\text{e}(t) = v_\text{e} \begin{pmatrix} \sin\theta_\text{e} \sin\phi(t) \\ \sin\theta_\text{e} \cos\theta_\text{e}\,(\cos\phi(t) - 1) \\ \cos^2\theta_\text{e} + \sin^2\theta_\text{e} \cos\phi(t) \end{pmatrix}\,, \tag{5.10}$$

where $v_\text{e} = 240\,\text{km/s}$, $\theta = 42^\circ$, and $\phi(t) = 2\pi\big(\frac{t}{24\,\text{hr}}\big)$. It is this periodicity of the *direction* of $\boldsymbol{v}_\text{e}(t)$ that induces the daily modulation in $R(t)$ we study in this work.[1]

[1] Annual modulation is also present, due to the change of the *magnitude* of $\boldsymbol{v}_\text{e}$, as in any terrestrial direct detection experiment. Here we fix $v_\text{e} = 240\,\text{km/s}$ and focus on the daily modulation signal, which is unique to anisotropic (crystal) targets.

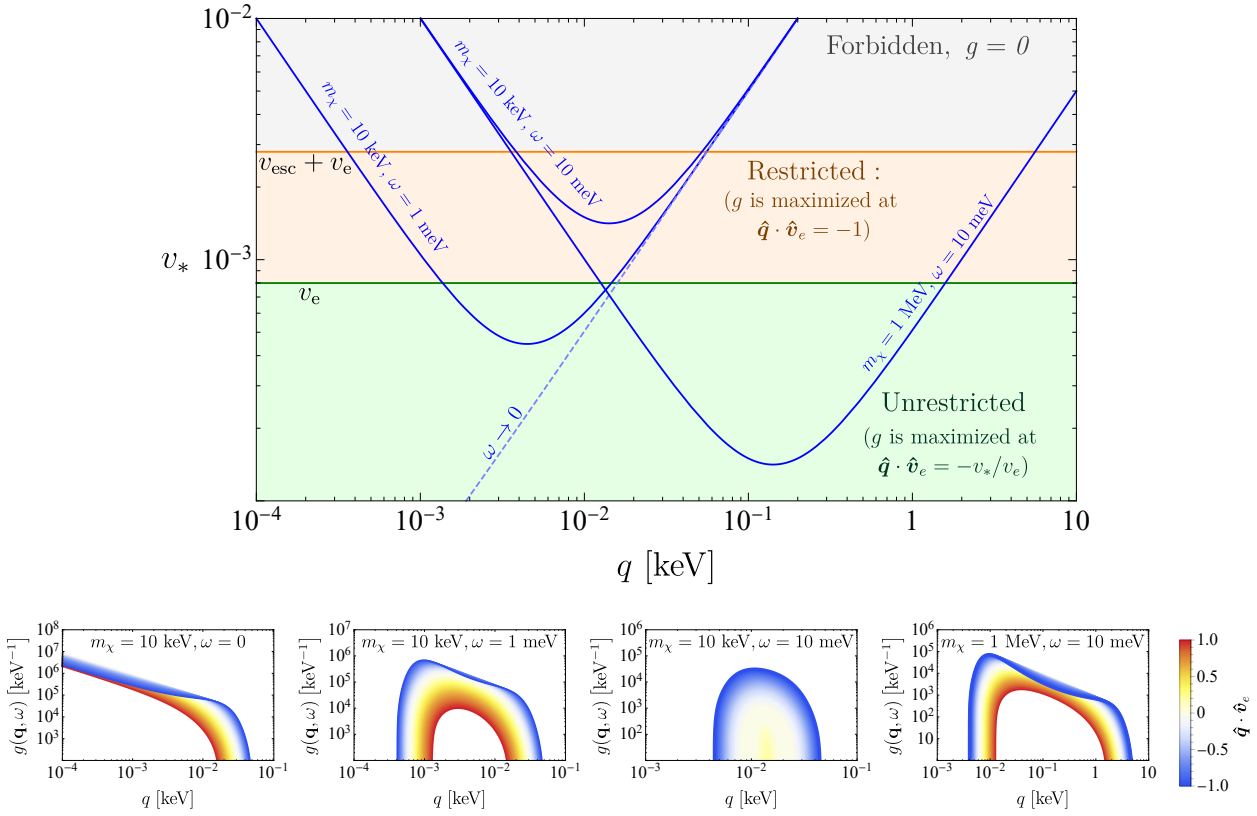

Figure 5.1: **Top:** To understand the kinematic function, $g(\boldsymbol{q}, \omega)$, defined in Eq. (5.11), we plot $v_* \equiv \frac{q}{2m_\chi} + \frac{\omega}{q}$ as a function of q (blue) for various m_χ and ω values. Comparing v_* to $v_{\rm e}$ and $v_{\rm e} + v_{\rm esc}$ we can qualitatively reconstruct the shape of $g(\boldsymbol{q}, \omega)$, as discussed in the text. **Bottom:** $g(\boldsymbol{q}, \omega)$ vs. q for several fixed m_χ, ω values, with varying $\hat{\boldsymbol{q}} \cdot \hat{\boldsymbol{v}}_{\rm e}$. The kinematic function weights different $\hat{\boldsymbol{q}}$ directions according to their angle with respect to $\boldsymbol{v}_{\rm e}(t)$, which ultimately leads to a daily modulating rate.

With the specific form of f_χ in Eq. (5.9), the velocity integral in Eq. (5.1) can be done analytically [7, 82, 191]. We define

$$\begin{aligned} g(\boldsymbol{q}, \omega, t) &\equiv \int d^3v \, f_\chi(\boldsymbol{v}, t) \, 2\pi\delta(\omega - \omega_{\boldsymbol{q}}) \\ &= \frac{2\pi^2 v_0^2}{N_0 q} \left\{ \exp\left[-\frac{(v_-(\boldsymbol{q}, \omega, t))^2}{v_0^2} \right] - \exp\left[-\frac{v_{\rm esc}^2}{v_0^2} \right] \right\}, \end{aligned} \tag{5.11}$$

where

$$v_-(\boldsymbol{q}, \omega, t) = \min\left(\left| \hat{\boldsymbol{q}} \cdot \boldsymbol{v}_{\rm e}(t) + \frac{q}{2m_\chi} + \frac{\omega}{q} \right|, \; v_{\rm esc} \right). \tag{5.12}$$

We will refer to $g(\boldsymbol{q}, \omega, t)$ as the *kinematic function*. The rate formula Eq. (5.1) then becomes

$$R(t) = \frac{1}{\rho_T} \frac{\rho_\chi}{m_\chi} \frac{\pi \overline{\sigma}_\psi}{\mu_{\chi\psi}^2} \int \frac{d^3q}{(2\pi)^3} F_{\rm med}^2(q) \sum_\nu S'_\nu(\boldsymbol{q})\, g(\boldsymbol{q}, \omega_{\nu,\boldsymbol{k}}, t)\,. \tag{5.13}$$

With the rate written in this form, the time dependence now comes from the v_- function contained in $g(\boldsymbol{q}, \omega, t)$. As we will discuss in detail in the rest of this subsection, the origin of daily modulation is as follows. First, the kinematic function $g(\boldsymbol{q}, \omega, t)$ selects a region of $\boldsymbol{q}$ space at each time of the day that is strongly correlated with $\boldsymbol{v}_{\rm e}(t)$. For anisotropic targets, this then results in a modulating rate after the $\boldsymbol{q}$ integral in Eq. (5.13). Intuitively, the DM wind hits the target from different directions throughout the day, some of which may induce a stronger response than others.

Kinematic Function

The kinematic function $g(\boldsymbol{q}, \omega_{\nu,\boldsymbol{k}}, t)$ can be viewed as a weight function: for each phonon branch ν, the integrand in Eq. (5.13), $F_{\rm med}^2(q)\, S'_\nu(\boldsymbol{q})$, is weighted toward momentum transfers $\boldsymbol{q}$ that maximize the g function or, equivalently, minimize v_- defined in Eq. (5.12). To visualize this minimization, we plot

$$v_* \equiv \frac{q}{2m_\chi} + \frac{\omega}{q} \tag{5.14}$$

as a function of q in the top panel of Fig. 5.1. Setting ω to a constant approximates the case of optical phonons, which have relatively flat dispersions, whereas $\omega \to 0$ corresponds to the case of acoustic phonons, for which ω/q is bounded by the sound speed, which is typically much smaller than the DM's velocity. We can identify three distinct regions (as shown with different colors in the plot):

- For $v_* \geq v_{\rm esc} + v_{\rm e}$, we have $v_- = v_{\rm esc}$ and therefore $g = 0$ for all $\hat{\boldsymbol{q}}$ directions. This is the kinematically forbidden region.
- For $v_{\rm e} \leq v_* < v_{\rm esc} + v_{\rm e}$, the g function is maximized at $\hat{\boldsymbol{q}} \cdot \hat{\boldsymbol{v}}_{\rm e} = -1$.
- For $v_* \leq v_{\rm e}$, the g function is nonzero for all $\hat{\boldsymbol{q}}$ directions, and is maximized at $\hat{\boldsymbol{q}} \cdot \hat{\boldsymbol{v}}_{\rm e} = -v_*/v_e$. In the large m_χ, small ω limit, $v_* \to 0$, and therefore the g function is maximized when $\hat{\boldsymbol{q}} \cdot \hat{\boldsymbol{v}}_{\rm e} = 0$.

These behaviors are seen in the lower panels of Fig. 5.1 (see also Ref. [7]), where we plot $g(\boldsymbol{q}, \omega)$ as a function of q for fixed m_χ, ω, and with varying $\hat{\boldsymbol{q}} \cdot \hat{\boldsymbol{v}}_{\rm e}$. Note that in the $\omega \to 0$ case, the g function has support down to $q = 0$, but the phase space integral for acoustic phonons is cut off at $q_{\rm min} \simeq \frac{\omega_{\rm min}}{c_s} = 2 \times 10^{-2}\,\text{keV} \left(\frac{\omega_{\rm min}}{1\,\text{meV}}\right)\left(\frac{5\times10^{-5}}{c_s}\right)$, where $\omega_{\rm min}$ is the detector's energy threshold, and c_s is the sound speed (slope of the linear dispersion). From these plots we see

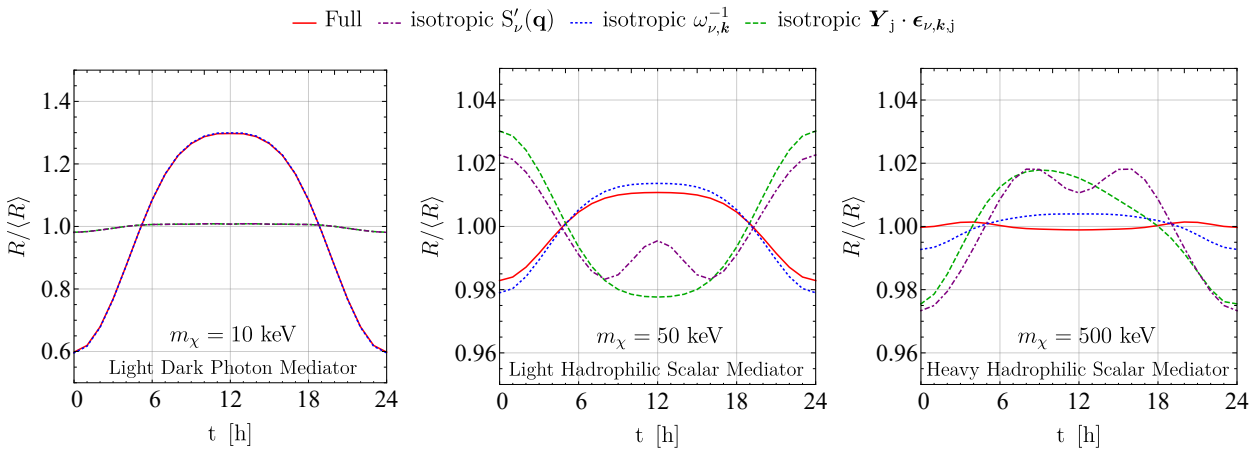

Figure 5.2: Comparison between the various sources of anisotropy a in SiO_2 target, for an example DM mass for each benchmark model. A 1 meV energy threshold is assumed in all cases. As discussed in the text, anisotropy in the $\boldsymbol{Y}_j \cdot \boldsymbol{\epsilon}_{\nu,\boldsymbol{k},j}$ factor in Eq. (5.7) is the dominant factor in determining the daily modulation pattern.

that the kinematically favored region of $\boldsymbol{q}$ is strongly correlated with $\hat{\boldsymbol{v}}_e(t)$ and, therefore, rotates with it throughout the day. This rotation then translates any target anisotropy into a detection rate that modulates daily.

Sources of Anisotropy

There are a number of possible sources of anisotropy, as we can infer from Eq. (5.13) and Eq. (5.7). First of all, the phonon energies $\omega_{\nu,\boldsymbol{k}}$ generically depend on the direction of $\boldsymbol{q} = \boldsymbol{k} + \boldsymbol{G}$. This means that the region selected by the kinematic function, as discussed above, does not preserve its shape as it rotates in $\boldsymbol{q}$ space. Also, the $\omega^{-1}_{\nu,\boldsymbol{k}}$ factor in Eq. (5.7) is different in the dominating kinematic region at different times of the day, which adds to the daily modulation signal.

The anisotropy in $\omega_{\nu,\boldsymbol{k}}$ has two contributing factors. First, phonon dispersions can be anisotropic as a result of crystal structures. For example, in h-BN, the sound speed of the longitudinal acoustic phonons differs by more than a factor of two between different $\boldsymbol{k}$ directions. Second, by the prescription explained above Eq. (5.6), a sphere of constant q outside the 1BZ does not map to a sphere of constant k inside the 1BZ. Since the size of the 1BZ is typically $O(\text{keV})$, and the DM velocity is $O(10^{-3})$, this is relevant for $m_\chi \gtrsim$ MeV. Another related source of anisotropy is the $e^{i\boldsymbol{G}\cdot\boldsymbol{x}^0_j}$ factor in Eq. (5.7): a constant-q sphere outside the 1BZ does not map onto a unique $\boldsymbol{G}$ vector.

In addition to $\omega_{\nu,\boldsymbol{k}}$ and $e^{i\boldsymbol{G}\cdot\boldsymbol{x}^0_j}$ discussed above, the scalar product of the DM-ion coupling

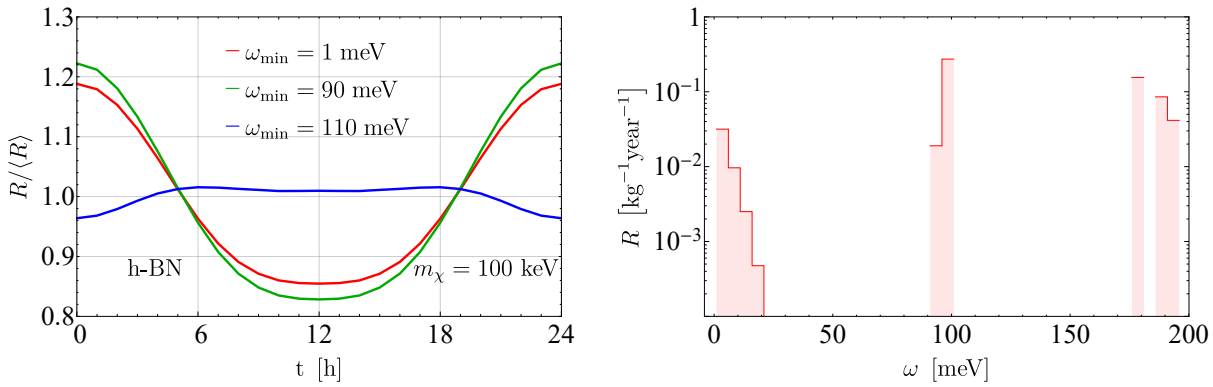

Figure 5.3: **Left:** Daily modulation for a h-BN target with various experimental thresholds, $\omega_{\rm min}$, assuming dark photon mediated scattering and $m_\chi = 100$ keV. **Right:** Differential rate at $t = 0$ for the same process assuming $\overline{\sigma}_e = 10^{-43}$ cm^2. The daily modulation pattern is drastically different depending on whether the optical phonon modes just below 100 meV are included or excluded.

and phonon eigenvectors, $\boldsymbol{Y}_j \cdot \boldsymbol{\epsilon}_{\nu,\boldsymbol{k},j}$, can also be anisotropic for a variety of reasons, depending on the DM model. For the hadrophilic scalar mediator model, $\boldsymbol{Y}_j \cdot \boldsymbol{\epsilon}_{\nu,\boldsymbol{k},j}$ are simply proportional to the longitudinal components of phonon eigenvectors $\hat{\boldsymbol{q}} \cdot \boldsymbol{\epsilon}_{\nu,\boldsymbol{k},j}$, so the anisotropy is determined by the extent to which the phonon eigenvectors deviate from transverse and longitudinal in different $\hat{\boldsymbol{q}}$ directions. For the dark photon mediator model, $\boldsymbol{Y}_j \cdot \boldsymbol{\epsilon}_{\nu,\boldsymbol{k},j}$ are instead proportional to $\frac{\hat{\boldsymbol{q}} \cdot \boldsymbol{Z}_j^\star \cdot \boldsymbol{\epsilon}_{\nu,\boldsymbol{k},j}}{\hat{\boldsymbol{q}} \cdot \boldsymbol{\varepsilon}_\infty \cdot \hat{\boldsymbol{q}}}$, so there are additional anisotropies if the Born effective charges $\boldsymbol{Z}_j^\star$ and dielectric tensor $\boldsymbol{\varepsilon}_\infty$ are not proportional to the identity. All these anisotropies are ultimately determined by the crystal structure.

We can carry out a simple exercise to see how the various sources of anisotropy discussed above contribute to the full daily modulation signal. As an example, we consider a SiO_2 target, and pick one m_χ value for each benchmark model, as shown in the three panels of Fig. 5.2. We obtain the full rate normalized to its daily average, $R/\langle R \rangle$, as a function of time, as shown by the solid red curves labeled by "full." We then artificially make the various factors in the rate formula isotropic and see how the modulation pattern changes.

First, we make $S'_\nu(\boldsymbol{q})$ isotropic by setting $\omega_{\nu,\boldsymbol{k}}$ and $\boldsymbol{Y}_j \cdot \boldsymbol{\epsilon}_{\nu,\boldsymbol{k},j}$ to their values at a specific direction ($\hat{\boldsymbol{q}} = \hat{\boldsymbol{z}}$), and setting $e^{i\boldsymbol{G}\cdot\boldsymbol{x}_j^0} \to 1$. This isolates the effect of the kinematic function $g(\boldsymbol{q}, \omega_{\nu,\boldsymbol{k}}, t)$ on daily modulation. The results are shown by the dot-dashed purple curves in Fig. 5.2, labeled "isotropic $S'_\nu(\boldsymbol{q})$." In all three panels, we see that the "isotropic $S'_\nu(\boldsymbol{q})$" curves are far from the full results (solid red curves), meaning that the anisotropy in $S'_\nu(\boldsymbol{q})$ plays an important role in determining the total modulation pattern. We find the same

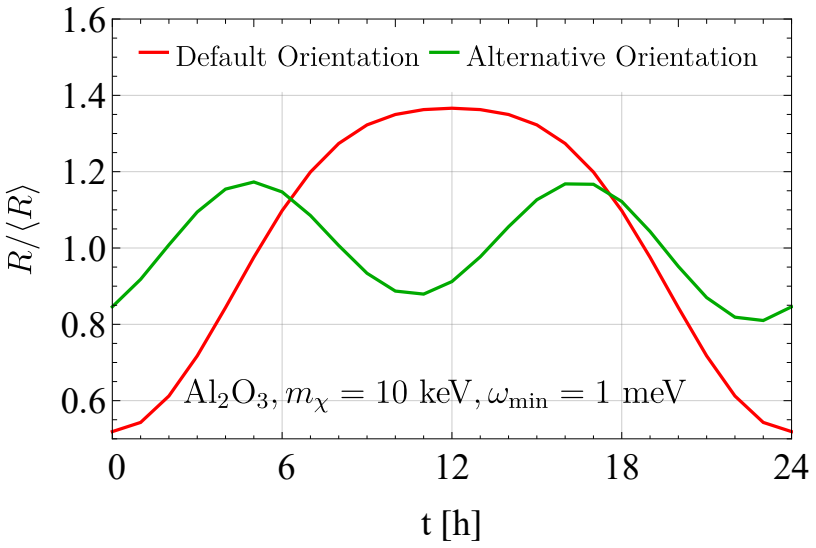

Figure 5.4: Effect of the crystal target orientation on the daily modulation pattern, for a sapphire target and the light dark photon mediator model as an example. The default orientation is the one adopted in Refs. [7, 82, 191] for which $\boldsymbol{v}_{\rm e}(t)$ is given by Eq. (5.10), and the alternative orientation is achieved by rotating the crystal z axis by 60° clockwise around $\hat{\boldsymbol{n}} = (\hat{\boldsymbol{x}} + \hat{\boldsymbol{y}} + \hat{\boldsymbol{z}})/\sqrt{3}$.

conclusion for the other materials and for other m_χ, $\omega_{\rm min}$ values.

We can further dissect the anisotropy in $S'_\nu(\boldsymbol{q})$ by computing the daily modulation with $\omega^{-1}_{\nu,\boldsymbol{k}}$ or $\boldsymbol{Y}_j \cdot \boldsymbol{\epsilon}_{\nu,\boldsymbol{k},j}$ made isotropic by the same prescription as above; these are labeled "isotropic $\omega^{-1}_{\nu,\boldsymbol{k}}$" (dotted blue curves) and "isotropic $\boldsymbol{Y}_j \cdot \boldsymbol{\epsilon}_{\nu,\boldsymbol{k},j}$" (dashed green curves) in Fig. 5.2, respectively. We see that the anisotropy in the $\boldsymbol{Y}_j \cdot \boldsymbol{\epsilon}_{\nu,\boldsymbol{k},j}$ factor contributes the most to daily modulation, as making it isotropic leads to the most significant deviations from the full results. We find the same is true for other materials.

We have also examined the effect of setting $e^{i\boldsymbol{G}\cdot\boldsymbol{x}^0_j} \to 1$ in $S'_\nu(\boldsymbol{q})$ while leaving both $\omega^{-1}_{\nu,\boldsymbol{k}}$ and $\boldsymbol{Y}_j \cdot \boldsymbol{\epsilon}_{\nu,\boldsymbol{k},j}$ intact. This has a visible impact only when the region of $\boldsymbol{q}$ space just outside the 1BZ has a significant contribution to the rate; as $\boldsymbol{q}$ moves farther away from the 1BZ, summing over contributions from many different $\boldsymbol{G}$ vectors mitigates the effect. For the dark photon mediator model, this explains the enhanced daily modulation at $m_\chi \gtrsim$ MeV (see Fig. 5.5 below). For the light hadrophilic scalar mediator model, there is no significant effect since the $\boldsymbol{q}$ integral is dominated by small q. For the heavy hadrophilic scalar mediator model, in contrast, the $\boldsymbol{q}$ integral is dominated by large q, so the enhancement happens in a window around $m_\chi \sim$ MeV (see Fig. 5.7 below).

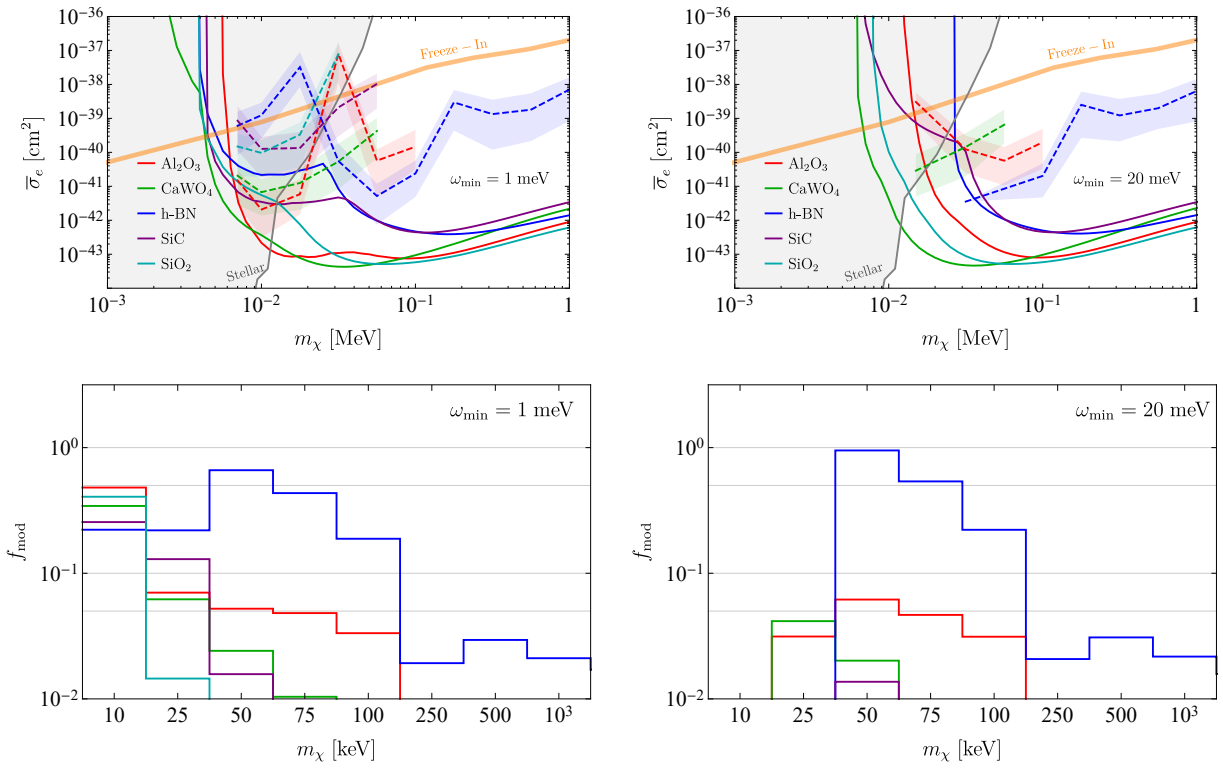

Figure 5.5: **Top:** Projected reach for the dark photon mediator model assuming 1 meV and 20 meV energy thresholds and one kg-year exposure. Solid curves show the 95% confidence level (CL) exclusion limits in the case of zero observed events, assuming no background. Dashed curves and the associated $\pm 1\sigma$ bands show the modulation reach for DM masses with more than 1% daily modulation, *i.e.* cross sections for which we can reject the non-modulating hypothesis and establish the statistical significance of a modulating signal, as explained in App. E.1. **Bottom:** Daily modulation amplitudes $f_{\rm mod}$, defined in Eq. (5.15), for the same energy thresholds for selected DM masses. Results are shown only for m_χ values where a material has substantial reach and $f_{\rm mod} > 10^{-2}$.

Effects of Experimental Setup

The daily modulation pattern can also be significantly affected by experimental factors, including in particular the detector's energy threshold and the orientation of the target crystal. The energy threshold $\omega_{\rm min}$ can be important if phonon modes at different energies have different modulation patterns. As an example, we show in the left panel of Fig. 5.3 the daily modulation in h-BN for several different values of $\omega_{\rm min}$, for the dark photon mediator model with $m_\chi = 100\,$keV. The distinct daily modulation curves can be understood from

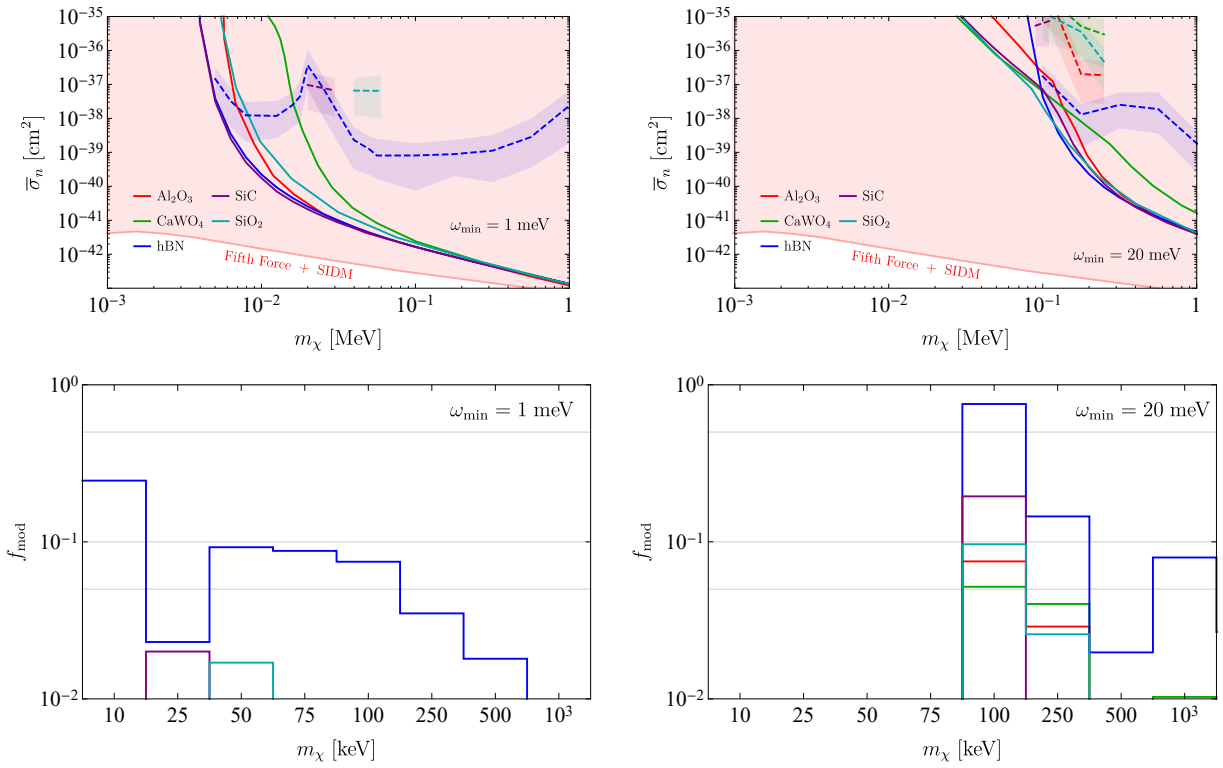

Figure 5.6: Same as Fig. 5.5, for the light hadrophilic scalar mediator model.

the differential rate plot in the right panel of Fig. 5.3. We see that the phonon modes just below 100 meV dominate the total rate, so long as $\omega_{\rm min}$ is below this, and they drive the daily modulation pattern. On the other hand, if $\omega_{\rm min} > 100$ meV, these modes are no longer accessible, and the daily modulation is instead induced by phonon modes at energies higher than about 175 meV, for which the rate has a very different time dependence.

Meanwhile, the orientation of the crystal determines the function $\boldsymbol{v}_{\rm e}(t)$, and hence the daily modulation pattern. As an example, Fig. 5.4 compares the daily modulation patterns between our default setup, given in Eq. (5.10), and an (arbitrarily chosen) alternative orientation where the crystal z axis is rotated by 60° clockwise around $\hat{\boldsymbol{n}} = (\hat{\boldsymbol{x}} + \hat{\boldsymbol{y}} + \hat{\boldsymbol{z}})/\sqrt{3}$.

5.3 Target Comparison

Having discussed the physics underlying daily modulation, we now consider concrete target materials. Among the 26 materials studied [206], 19 are observed to have more than 1% daily modulation for some DM masses in at least one of the benchmark models considered.

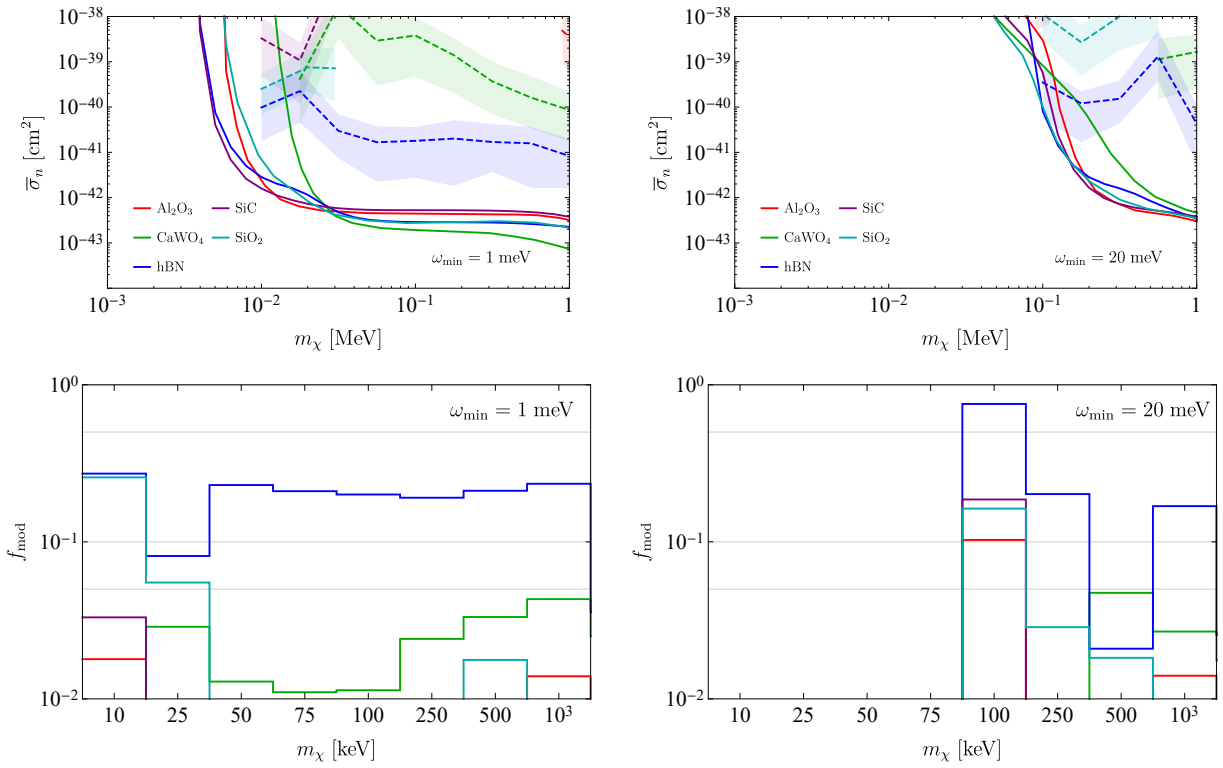

Figure 5.7: Same as Fig. 5.5, for the heavy hadrophilic scalar mediator model.

In this section, we focus on the following five which are observed to have the highest daily modulation amplitudes: Al_2O_3, SiO_2, SiC, $CaWO_4$ and h-BN. Among them, Al_2O_3, SiO_2 and SiC have been proposed and recommended for near-future phonon-based experiments, while Al_2O_3 and $CaWO_4$ are in use in the CRESST experiment. Meanwhile, h-BN is a highly anisotropic target with layered crystal structure that we have found to have exceptionally large daily modulation; while its experimental prospects have not been assessed, it serve as a useful benchmark for our theoretical study. We supplement this analysis with the remaining 14 materials with more than 1% daily modulation (AlN, CaF_2, GaN, GaSb, InSb, LiF, MgF_2, MgO, NaF, PbS, PbSe, PbTe, ZnO, ZnS) in App. E.

Our main results are shown in Figs. 5.5, 5.6 and 5.7, for the dark photon mediator model and the light and heavy hadrophilic scalar mediator models, respectively. In the top panels of each figure, we show both the projected exclusion limits (solid) and the cross sections needed to distinguish the modulating signal and a non-modulating hypothesis in the event of discovery (dashed and shaded $\pm 1\sigma$ bands), assuming 1 and 20 meV energy thresholds. For the solid curves, we set $t = 0$ when computing the rates for concreteness, and assume

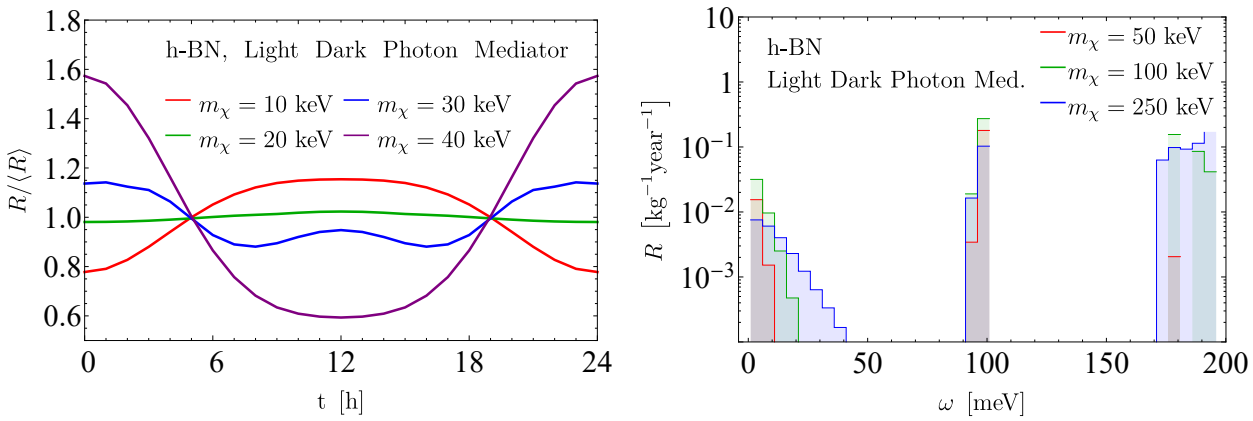

Figure 5.8: **Left:** Daily modulation for an h-BN target with various DM masses, assuming dark photon mediated scattering and $\omega_{\rm min} = 1\,$meV. The change in modulation pattern is a result of the kinematically favored $\hat{\boldsymbol{q}} \cdot \hat{\boldsymbol{v}}_{\rm e}$ increasing from -1 toward 0 as m_χ increases. During the transition between different modulation patterns, an intermediate mass value around 20 keV features a reduced modulation amplitude, which explains the peak in the modulation reach curve in the top-left panel of Fig. 5.5. A similar effect is also observed for the hadrophilic scalar mediator models in Figs. 5.6 and 5.7. **Right:** Differential rates at $t = 0$ for several higher m_χ assuming $\overline{\sigma}_e = 10^{-43}$ cm^2. Another transition between modulation patterns occurs when new phonon modes become dominant as m_χ increases, resulting in a second reduced modulation mass point, around 200 keV, in Fig. 5.5.

3 events per kilogram-year exposure, corresponding to 95 % confidence level (CL) exclusion in a background-free experiment. The results for Al_2O_3, $CaWO_4$ and SiO_2 were computed previously in Ref. [192] (numerical errors in some of the materials in early versions of that reference have been corrected here and on the interactive webpage [206]), and here we perform the calculation also for SiC and h-BN. For the dashed curves and the shaded bands for the modulation reach, we compute the number of events needed to reject the constant rate hypothesis at the 95 % confidence level by a prescription discussed in App. E.1; they are truncated where the daily modulation falls below 1%.

In the lower panels of Figs. 5.5, 5.6 and 5.7, we quantify the amount of daily modulation for several representative DM masses by

$$f_{\rm mod} \equiv \frac{\max\big(|R - \langle R\rangle|\big)}{\langle R\rangle}\,, \tag{5.15}$$

which characterizes the maximum deviation of detection rate throughout the day from the daily average $\langle R\rangle$. We shall refer to $f_{\rm mod}$ as the daily modulation amplitude. The $f_{\rm mod}$ plots give us an overview of the amount of daily modulation to expect. More detailed information

on the daily modulation signal can be gained by plotting $R(t)/\langle R\rangle$, as in Figs. 5.2, 5.3 and 5.4, for each DM mass and energy threshold; we provide these plots on the interactive webpage [206].

We have considered detector energy thresholds $\omega_{\rm min} = 1\,\text{meV}$ and 20 meV. For the dark photon mediator model (Fig. 5.5), the energy threshold does not have a significant impact on either the reach or the daily modulation amplitude, except at the lowest m_χ values. This is because gapped optical phonons dominate the rate as long as they are above $\omega_{\rm min}$ and the DM is heavy enough to excite them. For the hadrophilic scalar mediator models (Figs. 5.6 and 5.7), on the other hand, gapless acoustic phonons dominate and, as a result, both the reach and the daily modulation amplitude are sensitive to $\omega_{\rm min}$. Generally, a higher energy threshold tends to amplify the daily modulation since the kinematically accessible phase space becomes limited, as discussed in detail in Sec. 5.2. Similarly, the daily modulation amplitude tends to increase at the lowest m_χ considered because of phase space restrictions. The enhanced daily modulation in these cases comes at the price of a lower total rate, so there is a trade-off between better overall sensitivity and a higher daily modulation signal. This is reflected by the dashed modulation reach curves in the top panels of each figure, which ascend at lower masses since the rate also vanishes.

From Figs. 5.5, 5.6 and 5.7, we see that h-BN consistently outperforms all other materials in terms of the daily modulation amplitude, which reaches $O(1)$ for some m_χ and $\omega_{\rm min}$ values. This is due to the layered crystal structure which means that the momentum transfers perpendicular and parallel to the layers lead to very different target responses. Among the other materials, Al_2O_3, $CaWO_4$ and SiC are also competitive targets for the dark photon mediator model at $m_\chi \lesssim 100\,\text{keV}$, and $CaWO_4$ shows percent level daily modulation across a wide range of DM masses for the heavy scalar mediator model.

It is also worth noting that the modulation reach curves and $f_{\rm mod}$ often exhibit a nontrivial dependence on m_χ. In particular, for given target material and $\omega_{\rm min}$, there can be m_χ values where the modulation signal diminishes. For example, for dark photon mediated scattering, h-BN with $\omega_{\rm min} = 1\,\text{meV}$ has two such low-$f_{\rm mod}$ mass points at around 20 keV and 200 keV, corresponding to the peaks of the modulation reach curve in the top-left panel of Fig. 5.5.

Generally, low-$f_{\rm mod}$ points at low m_χ result from the change in $\hat{\boldsymbol{q}}\cdot\hat{\boldsymbol{v}}_{\rm e}$ favored by the kinematic function. As discussed in Sec. 5.2, as m_χ increases, the favored $\hat{\boldsymbol{q}}\cdot\hat{\boldsymbol{v}}_{\rm e}$ increases from -1 toward 0. As $\hat{\boldsymbol{v}}_{\rm e}$ changes with time (*e.g.* as in Eq. (5.10)), a given $\hat{\boldsymbol{q}}\cdot\hat{\boldsymbol{v}}_{\rm e}$ probes the crystal's $S'_\nu(\boldsymbol{q})$ along a set of $\hat{\boldsymbol{q}}$ directions that modulates, and the modulation pattern depends on the kinematically favored $\hat{\boldsymbol{q}}\cdot\hat{\boldsymbol{v}}_{\rm e}$ value. We verify this expectation in the left panel of Fig. 5.8 for h-BN. In this case, the modulation pattern flips as m_χ increases from 10 keV to 40 keV, and an approximate cancelation occurs around 20 keV. Note, however, that the daily modulation sensitivity may be recovered by analyzing the differential rates $\frac{dR(t)}{d\omega}$.

The low-$f_{\rm mod}$ points at higher m_χ, on the other hand, are explained by new phonon modes with different modulation patterns becoming kinematically accessible as m_χ increases. Again focusing on h-BN as an example, we see from the right panel of Fig. 5.8 that while the dominant phonon modes are the $\sim 100\,\text{meV}$ modes for $m_\chi = 50\,\text{keV}$ and 100 keV, the modes above 150 meV take over as m_χ increases to 250 keV. The reduced modulation sensitivity at

$m_\chi \simeq 200\,\mathrm{keV}$ results from the transition between the two regimes.

5.4 Conclusions

As new experiments focused on light DM detection with single optical and acoustic phonons begin an R&D phase [203], it is important and timely to understand which target crystals have the optimal sensitivity to well-motivated DM models. This includes not only the sensitivity to the smallest interaction cross section for a given DM model, but also the ability to extract a smoking gun signature for DM that can be distinguished from background. Daily modulation provides such a unique fingerprint. In this work, we have carried out a comparative study of daily modulation signals for several benchmark models, where DM scattering is mediated by a dark photon or hadrophilic scalar mediator. Our results supplement the information on the cross section reach obtained previously in Ref. [192], and provide further theoretical guidance to the optimization of near future phonon-based experiments.

Our analysis shows that there is often a trade-off between detection rate, modulation amplitude, and experimental feasibility. For example, for dark photon mediated scattering, Al_2O_3 (sapphire), $CaWO_4$ and SiO_2 (α-quartz) outperform h-BN in terms of their sensitivities to the total rate; h-BN's daily modulation signal, however, is significantly stronger. Still, despite having the largest daily modulation amplitude, h-BN will likely be difficult to fabricate as a large ultra-pure single crystal target. Overall, Al_2O_3 and $CaWO_4$ provide perhaps the optimal balance between the overall reach and the daily modulation signal, and have both already been used in direct detection experiments.

Beyond the results presented in this chapter, we also publish an interactive webpage [206], where additional results can be generated from our calculations of single phonon excitation rates and their daily modulation.

Appendix A

Asymmetric Dark Matter Nuggets: Material Overburden

In this appendix we calculate the material overburden due to the rock above the experiments. The relevant quantity is the energy lost per unit of distance that was traveled through the material in question. For an ADM nugget coupling to hadronic matter and with velocity v, the average energy loss per collision is

$$\langle \Delta E \rangle_{v_0} = \frac{1}{\overline{\sigma}_{XN}} \int dE\, dq\; E\, |F_X(q)|^2 |F_{\rm med}(q)|^2 \frac{d\bar{\sigma}_{XN}}{dE\, dq} \tag{A.1}$$

$$= \frac{1}{\overline{\sigma}_{XN}} \frac{A^2}{4 m_N m_n^2 v_0^2} \int dq\; q^3\, |F_X(q)|^2 |F_{\rm med}(q)|^2 \tag{A.2}$$

with

$$\overline{\sigma}_{XN} = \int dE\, dq\; |F_X(q)|^2 |F_{\rm med}(q)|^2 \frac{d\bar{\sigma}_{XN}}{dE\, dq} \tag{A.3}$$

$$= \frac{A^2}{2 m_n^2 v_0^2} \int dq\; q\, |F_X(q)|^2 |F_{\rm med}(q)|^2, \tag{A.4}$$

where we took the $M_X \gg m_N$ limit. The average energy loss per unit of length is thus

$$\left\langle \frac{dE}{dx} \right\rangle_{v_0} \approx \mathrm{Min}\left[\, n_T \overline{\sigma}_{XN}, n_T^{1/3} \,\right] \times \langle \Delta E \rangle_{v_0}\,, \tag{A.5}$$

with n_T the number density of the material. The second term in Min accounts for the possibility that the nugget scatters off every nucleus it meets, which occurs if the cross section is sufficiently large [122]. The presence of the form factor implies that the overburden depends on the nugget radius. For large nuggets, the probability of transferring a sizable amount of momentum is suppressed, these nuggets are much less likely to get stopped, as compared to a point-like DM with a comparable mass and cross section.

For ADM nuggets coupling to electrons through a light mediator, we estimate the energy loss with the Lindhard-Scharff formula for electronic energy loss [209]. For a singly ionized atom with speed v and atomic number Z_1, traveling the through medium with atomic number Z_2, the average energy loss per unit distance is

$$\left\langle \frac{dE}{dx} \right\rangle \approx 8\pi n_2 e^2 a_0 \frac{Z_1 Z_2}{(Z_1^{2/3} + Z_2^{2/3})^{3/2}} \frac{v}{v_0}. \tag{A.6}$$

Here n_2 the number density of the target, e the electron charge, a_0 the Bohr radius and $v_0 \approx \alpha$ the typical velocity of a bound electron. This prescription has shown to be in reasonably good agreement with the data for a variety of projectile and target ions [210]. At low velocity the elastic atomic recoil can be of comparable importance [209], but since we only attempt an order of magnitude estimate here, we neglect this contribution. To estimate the overburden effect, we take the earth's crust to consist primarily of silicon $Z_2 = 14$ with a mean density of $n_2 = 2.7\,\mathrm{g/cm^3}$. We take $Z_1 = 1$, since the nugget does not have an electron cloud as long as its total effective electric charge is $\lesssim 1$. Because of the stringent stellar cooling bounds on g_e, this is always satisfied in our parameter space. For the light mediator case, we then estimate the energy loss per unit distance as

$$\left\langle \frac{dE}{dx} \right\rangle \approx 8\pi n_2 e^2 a_0 N_X g_\chi g_e \frac{v}{v_0} \approx 120 \times \frac{\mathrm{MeV}}{\mathrm{cm}} \times (N_X g_\chi g_e)^2 \times \frac{v}{10^{-3}}. \tag{A.7}$$

where we identified the dimensionless parameter $N_X g_\chi g_e$ with the electric charge in the Lindhard formula. (The energy loss in a dielectric is proportional to the square of the electric charge, see e.g. [211].) Requiring that the total energy loss remains smaller than the kinetic energy implies

$$\sigma_{Xe} \ll 10^{-24}\,\mathrm{cm}^2 \times \left(\frac{M_X}{\mathrm{GeV}}\right), \tag{A.8}$$

which is always satisfied for a scalar mediator in the parameter space we consider. For a vector mediator, there is a sliver of parameter space where this is not satisfied; however, this region is constrained by the SENSEI surface run. Finally, for a heavy mediator, the typical energy loss per collision is estimated to be $\langle \Delta E \rangle_0 \approx \frac{1}{2}\alpha^2 m_e \approx 10$ eV. Using Eq. (A.5), the ADM nugget would only get stopped in the earth's crust if

$$\sigma_{Xe} > 10^{-26}\,\mathrm{cm}^2 \times \left(\frac{M_X}{\mathrm{GeV}}\right) \qquad \text{and} \qquad M_X \lesssim 10^{11}\,\mathrm{GeV} \tag{A.9}$$

which is always satisfied for nuggets with 10 GeV constituents, but not for nuggets with 10 MeV constituents; however, the region where overburden is important is always constrained by the SENSEI surface run. Note that for both the heavy and light mediators with electron couplings we have implicitly treated the ADM nuggets as point particles, which is a good approximation for low mass ADM nuggets, which is where the overburden effect is relevant.

Appendix B

Zero Temperature Limit for Superconductors

From [212], $S(E_D, q)$ can be calculated by

$$S(E_D, q) = \frac{m_e v}{\pi q n_T} \int_{p_-}^{\infty} dp_2 \; p_2 f(E_2)(1 - f(E_4)), \tag{B.1}$$

where n_T is the number density of target, p_2 is the momentum of incoming electron, p_4 is the momentum of the outgoing electron and $f(E)$ is the Fermi-Dirac distribution:

$$\begin{gathered} p_- = \frac{m_e}{q}\left(E_D - \frac{q^2}{2m_e}\right) \qquad\qquad E_4 = E_2 + E_D \\ f(E) = \left[1 + \exp\left(\frac{E-\mu}{T}\right)\right]^{-1}, \end{gathered} \tag{B.2}$$

where at zero temperature, the chemical potential μ is simply the Fermi energy. In the zero temperature limit, the Fermi-Dirac distribution functions correspond to Heaviside theta functions and so the dynamics structure function becomes

$$S(E_D, q) = \frac{m_e v}{\pi q n_T} \int_{p_-}^{\infty} dp_2 \; p_2 \, \theta(\mu - E_2)\theta(E_4 - \mu). \tag{B.3}$$

Writing everything in terms of p_2, the two Heaviside theta functions simply become integration limits, so that

$$\begin{aligned} S(E_D, q) &= \frac{m_e v}{\pi q n_T} \int_{\xi}^{\sqrt{2m_e\mu}} dp_2 \; p_2 \theta(\sqrt{2m_e\mu} - \xi) \\ &= \frac{m_e v}{2\pi q n_T}(2m_e\mu - \xi^2)\theta(\sqrt{2m_e\mu} - \xi), \end{aligned} \tag{B.4}$$

where

$$\xi = \mathrm{Max}[p_-, \sqrt{2m_e(\mu - E_D)}]. \tag{B.5}$$

Appendix C

In Medium Polarization Tensor

The in-medium vacuum polarization tensor can be related to the optical response of the medium by using the two following relations [213]:

$$J_\mu = -\Pi_{\mu\nu} A^\nu \tag{C.1}$$

$$J^i = \sigma^i{}_j E^j \tag{C.2}$$

where $\sigma_{ij} = i\omega(\delta_{ij} - \boldsymbol{\epsilon}_{ij})$ is the conductivity tensor. Specifically, using eq.(C.2) and taking the spatial component of eq.(C.1) we get:

$$\begin{cases} J_i = -\Pi_{ij} A^j - \Pi_{i0} A^0 \\ \\ J_i = \sigma_{ij} E^j = \sigma_{ij} \left(i\omega A^j - i q^j A_0 \right) \end{cases} \tag{C.3}$$

where in the second equation we have used the Maxwell equation $E^j = i\omega A^j - i q^j A_0$. From this we see that

$$\Pi_{ij} = -i\omega\sigma_{ij} \tag{C.4}$$

$$\Pi_{i0} = i\sigma_{ij} q^j \,. \tag{C.5}$$

While from Eq. (C.2) and (C.1), together with current conservation $\partial_\mu J^\mu = 0$ and Maxwell equation $E^j = i\omega A^j - i q^j A_0$, we get

$$\Pi_{00} = \frac{1}{i\omega} \vec{q} \cdot \sigma \cdot \vec{q} . \tag{C.6}$$

Appendix D

Dielectric Tensor

Following [214], the imaginary part of the macroscopic dielectric tensor is given by the Lindhard formula

$$\mathrm{Im}[\boldsymbol{\epsilon}_{ii}(\omega)] = \frac{ge^2}{\mathbf{q}^2} \lim_{q\to 0} \sum_{nn'} \int \frac{d^3\mathbf{k}}{(2\pi)^3} 2\pi\, \delta(E_{n'\mathbf{k}} - E_{n\mathbf{k}} - \omega) |f_{[n\mathbf{k}\to n'\mathbf{k}+q\,\hat{\mathbf{e}}_i]}|^2 \,, \tag{D.1}$$

where $\hat{\mathbf{e}}_i$ are the unit vectors for the three cartesian components, and the sum runs over the energy levels. The energy conserving delta ensures that for small ω (*i.e.*, $\omega \lesssim v_F\Lambda \sim$ eV) only transition between the valence ($n = -$) and conduction ($n' = +$) band near the Dirac point will contribute. The form factor $|f_{[n\mathbf{k}\to n'\mathbf{k}']}|^2$ for these low energy transitions can be computed analytically in Dirac materials [88]:

$$|f_{[-\mathbf{k}\to+\mathbf{k}']}|^2 = \frac{1}{2}\left(1 - \frac{\tilde{\mathbf{k}}\cdot\tilde{\mathbf{k}}' + \Delta^2}{\sqrt{\tilde{\mathbf{k}}^2+\Delta^2}\sqrt{\tilde{\mathbf{k}}'^2+\Delta^2}}\right) . \tag{D.2}$$

where, as in the main text, $\tilde{\mathbf{k}} = (v_{Fx}k_x, v_{Fy}k_y, v_{Fz}k_z)$. Plugging this expression in Eq. (D.1) we are able to compute the imaginary part of the dielectric tensor for low energy deposition (*i.e.*, $\omega \lesssim v_F\Lambda \sim$ eV).

The real and imaginary part of the dielectric are related by the Kramers-Kronig relation:

$$\mathrm{Re}[\boldsymbol{\epsilon}_{ij}(\omega)] = 1 + \frac{2}{\pi}\mathcal{P}\int_0^\infty \frac{\mathrm{Im}[\boldsymbol{\epsilon}_{ij}(\omega')]\omega'}{\omega'^2-\omega^2} d\omega' \tag{D.3}$$

where $\mathcal{P}$ denotes the principal part value. From this relation it is clear that the real part of the dielectric, even for small values of ω, receives contributions also from transitions between states far away from the Dirac point. For these transitions the analytic expression of the form factor given in Eq. (D.2) is no longer accurate and we have to resort to a density functional perturbation theory calculation. The result, that we will use as an input for our calculations, is shown in Table 4.1.

D.1 Comparison with previous results

In this appendix we highlight the reasons behind the discrepancy between our results and the ones presented in references [88] and [152].

In these two works the dielectric was computed analytically exploiting the analogy between QED and low energy electronic excitations of Dirac materials (see Eq. (B.3) in [88], and Eq. (3.5) and (3.6) in [152]).[1] The analytic expression for the dielectric obtained is

$$\boldsymbol{\epsilon} = \mathbb{I} + \begin{pmatrix} \frac{v_{F,x}^2}{\kappa_{xx}} & 0 & 0 \\ 0 & \frac{v_{F,y}^2}{\kappa_{yy}} & 0 \\ 0 & 0 & \frac{v_{F,z}^2}{\kappa_{zz}} \end{pmatrix} \Pi(\tilde{q}^2)\,, \tag{D.4}$$

where κ_{ij} is the background dielectric and $\Pi(\tilde{q}^2)$ is computed analytically via the expression

$$\begin{aligned} \Pi(\tilde{q}^2) = = \frac{e^2 g}{4\pi^2\, v_{F,x} v_{F,y} v_{F,z}} \Bigg[\int_0^1 dx \left\{ x(1-x) \ln \left| \frac{(2\tilde{\Lambda})^2}{\Delta^2 - x(1-x)\tilde{q}^2)} \right| \right\} \\ + i\,\frac{\pi}{6} \sqrt{1 - \frac{4\Delta^2}{\tilde{q}^2}} \left(1 + \frac{2\Delta^2}{\tilde{q}^2}\right) \Theta(\tilde{q}^2 - 4\Delta^2) \Bigg]\,, \end{aligned} \tag{D.5}$$

with $\tilde{\Lambda} \equiv \Lambda \times \max\left(v_{F,x}, v_{F,y}, v_{F,z}\right)$ and $\tilde{\mathbf{q}} = (v_{Fx} q_x, v_{Fy} q_y, v_{Fz} q_z)$.

This analytic expression fails to reproduce the needed form of the real and imaginary parts of the dielectric that enters into both scattering and absorption rates. First, we note that Eq. (D.5) only includes the contribution from states near the Dirac point. This does not encompass most of the contribution to photon screening, which is dominated by electron states far from the Dirac cone. Thus for the real part of the dielectric used in calculating both absorption and scattering rates, we must employ instead the values computed from Density Functional Theory (DFT), shown in Table I. Second, the Lindhard formula Eq. (D.1) encodes the relevant information of the imaginary part of the dielectric needed, in particular, for absorption rates; the imaginary part of Eq. (D.4), however, reproduces the Lindhard formula only in the limit that $\kappa_{ii} \to 1$. We verified this prescription by comparison with DFT results.[2] These two important differences summarize the changes in comparison to Refs. [88] and [152], where the absorption and scattering rates computed here differ by at least an order of magnitude in comparison to previous results.

A procedure, akin to a renormalization and matching scheme, that manages to encapsulate the contribution of the high energy excitations in Eq. (D.4) with $\kappa_{ii} \to 1$, and gives qualitatively the same results of the procedure used in the main text is the following. The difference between the polarization tensor measured at two different energy scales (within

[1] The polarization tensor computed in Eq. (3.5) and (3.6) of [152] can be related to the dielectric tensor by using Eq. (C.4)

[2] We thank Hsiao-Yi Chen and Marco Bernardi for this comparison and for collaboration on future work.

the region of validity of the low energy effective theory) is finite and given by

$$\Pi(\tilde{q}^2) - \Pi(\tilde{q}_0^2) = \frac{e^2 g}{4\pi^2 v_{F,x} v_{F,y} v_{F,z}} \int_0^1 dx\, x(1-x) \left[\ln \left(\frac{\Delta^2 - \tilde{q}_0^2 x(1-x)}{\Delta^2 - \tilde{q}^2 x(1-x)} \right) \right] , \tag{D.6}$$

by computing $\boldsymbol{\epsilon}(0,0)$ from DFT we can extract the value of $\Pi(0) \simeq \boldsymbol{\epsilon}(0,0)/v_{\rm F}^2$ and write

$$\begin{aligned} \Pi(\tilde{q}^2) = \Pi(0) + \frac{\tilde{e}^2 g}{4\pi^2 v_{F,x} v_{F,y} v_{F,z}} \Bigg[\int_0^1 dx\, x(1-x) \ln \left| \frac{\Delta^2}{\Delta^2 - \tilde{q}^2 x(1-x)} \right| \\ + i \frac{\pi}{6} \sqrt{1 - \frac{4\Delta^2}{\tilde{q}^2}} \left(1 + \frac{2\Delta^2}{\tilde{q}^2} \right) \Theta(\tilde{q}^2 - 4\Delta^2) \Bigg] . \end{aligned} \tag{D.7}$$

The real part of $\Pi(\tilde{q}^2)$ turns out to be dominated by $\Pi(0)$, suggesting that the main contribution to the dielectric comes from electron states far from the Dirac cone. Moreover, this justifies the assumption made in the main text, *i.e.* $\boldsymbol{\epsilon}(\omega, \mathbf{q}) \simeq \boldsymbol{\epsilon}(0,0)$. By contrast, since $\Pi(0)$ is real, the imaginary part of Eq. (D.7) is the same of Eq. (D.5).

Finally, the anisotropic dielectric tensor derived in Appendix B of Ref. [88] carries a $\tilde{\mathbf{q}}^2$-dependence which would lead to a daily modulation for the absorption rate. As already pointed out by Ref. [152], the $\tilde{\mathbf{q}}^2$ dependence in Eq. (B.3) of Ref. [88] derives from an erroneous generalization of the isotropic dielectric; the correct expression replaces $\tilde{\mathbf{q}}^2 \to \mathbf{q}^2$ in Eq. (B.3) of Ref. [88] and implies no daily modulation rate for absorption.

Appendix E

Daily Modulation Amplitudes for Additional Materials

In addition to the materials discussed in the main text, we have also investigated the daily modulation of the full list of materials considered in Ref. [192]. Their projected reach curves were already computed in Ref. [192] and are included on the interactive webpage [206]. Here we only show the daily modulation amplitude $f_{\rm mod}$, defined in Eq. (5.15), as in the lower panels of Figs. 5.5, 5.6 and 5.7 in the main text. The results for the dark photon mediator model, the light hadrophilic scalar mediator model and the heavy hadrophilic scalar mediator model are shown in Figs. E.1, E.2 and E.3, respectively. Only materials with $f_{\rm mod} \geq 10^{-2}$ for at least one m_χ value are shown in each case.

E.1 Calculation of the Modulation Reach

To establish the statistical significance of a modulating signal, we find the expected number of events needed to reject the non-modulating hypothesis using the following procedure. For a given DM model, with the DM mass m_χ and experimental energy threshold $\omega_{\rm min}$ specified, we first obtain the modulating signal shape $r(t) \equiv R(t)/\langle R\rangle$ as explained in the main text. We divide a day into $N_{\rm bins} = 24$ equal-size bins, and denote the bin boundaries by $t_k = (k/N_{\rm bins})$ days. Given an expected number of events $N_{\rm exp}$, we simulate a DM signal sample and a non-modulating sample by generating events following a Poisson distribution in each bin, with mean $\langle N_k\rangle_{\rm sig} \equiv N_{\rm exp}\int_{t_{k-1}}^{t_k} r(t)\,dt/{\rm day}$ and $\langle N_k\rangle_{\text{non-mod}} \equiv N_{\rm exp}/N_{\rm bins}$ for the kth bin, respectively. We define our test statistic to be the difference between the Pearson's χ^2 values when fitting the simulated data to the non-modulating vs. modulating signal shapes. Concretely, suppose the number of events in the kth bin is N_k. The test statistic is given by

$$\text{TS} = \sum_k \frac{(N_k - \langle N_k\rangle_{\text{non-mod}})^2}{\langle N_k\rangle_{\text{non-mod}}} - \sum_k \frac{(N_k - \langle N_k\rangle_{\rm sig})^2}{\langle N_k\rangle_{\rm sig}}\,. \tag{E.1}$$

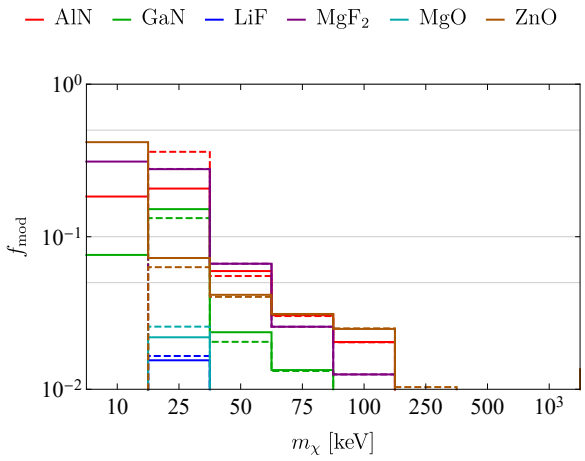

Figure E.1: Daily modulation amplitudes for the dark photon mediator model for selected DM masses. Solid and dashed lines assume energy thresholds of 1 meV and 20 meV, respectively. Among the materials studied, only those that have a modulation amplitude greater than 1% for at least one m_χ value are shown. As in the lower panels of Figs. 5.5, 5.6 and 5.7 in the main text, the low mass values where the rate diminishes are excluded for each material. Therefore the shown modulation amplitudes correspond to the mass values where the materials have reach.

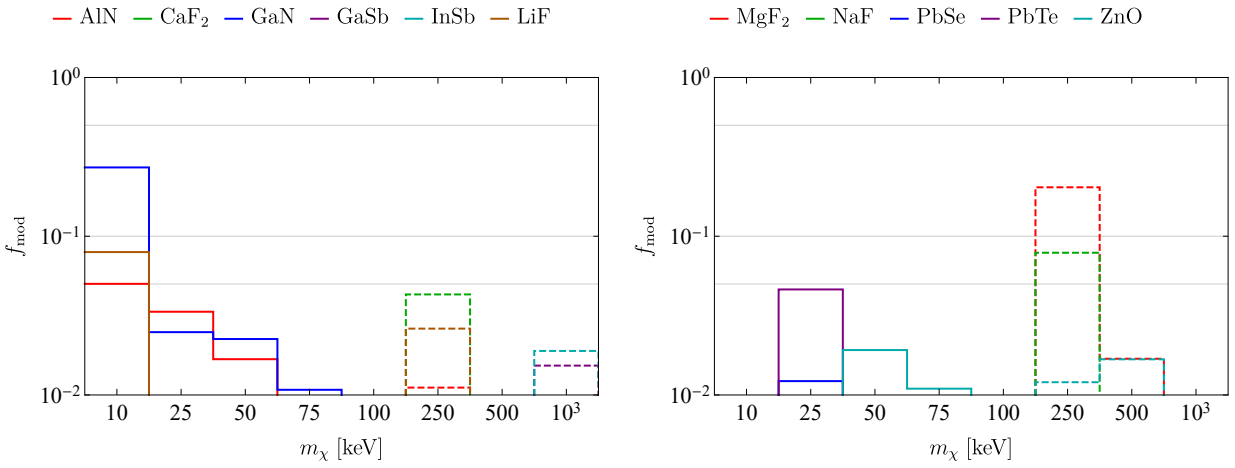

Figure E.2: Same as Fig. E.1, for the light hadrophilic scalar mediator model.

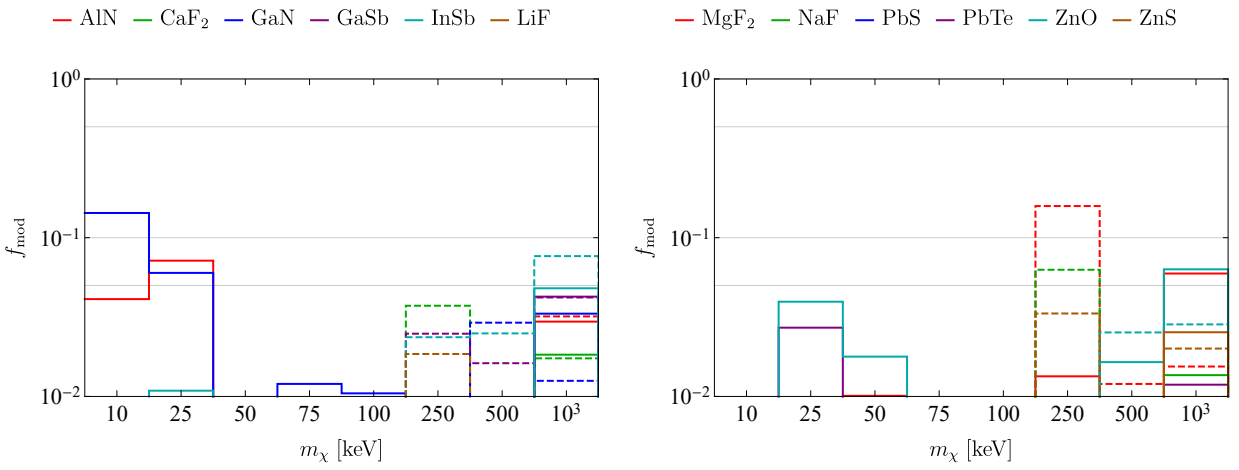

Figure E.3: Same as Fig. E.1, for the heavy hadrophilic scalar mediator model.

Given $N_{\rm exp}$, we simulate events according to the modulating (DM signal) and non-modulating hypotheses for $N_{\rm sample} = 10^4$ times each, and obtain the distribution of TS for the modulating and non-modulating samples. For the non-modulating sample, we compute the 95 percentile value $\mathrm{TS}_{\text{non-mod},\,95\%}$. For the modulating signal sample, we compute the mean $\mathrm{TS}_{\text{sig, mean}}$ and the (50 ± 34) percentiles $\mathrm{TS}_{\text{sig},\,\pm1\sigma}$. These numbers tell us to what extent we can reject the non-modulating hypothesis: $\mathrm{TS}_{\text{non-mod},\,95\%} < \mathrm{TS}_{\text{sig, mean}}$ means we can reject the non-modulating hypothesis at 95% CL on average, while $\mathrm{TS}_{\text{non-mod},\,95\%} < \mathrm{TS}_{\text{sig},\,\pm1\sigma}$ means we can reject the non-modulating hypothesis at 95% CL given a $\pm1\sigma$ statistical fluctuation of the signal. Repeating the calculation for many values of $N_{\rm exp}$, we obtain the interpolating functions $\mathrm{TS}_{\text{non-mod},\,95\%}(N_{\rm exp})$, $\mathrm{TS}_{\text{sig, mean}}(N_{\rm exp})$ and $\mathrm{TS}_{\text{sig},\,\pm1\sigma}(N_{\rm exp})$. These allow us to solve for the $N_{\rm exp}$ needed for $\mathrm{TS}_{\text{non-mod},\,95\%}$ to drop below $\mathrm{TS}_{\text{sig, mean}}$, and for it to go below $\mathrm{TS}_{\text{sig},\,\pm1\sigma}$. These then translate into cross sections assuming 1 kg-yr exposure, represented by the modulation reach curves in Figs. 5.5, 5.6 and 5.7. Note that the procedure here largely follows that in Ref. [82], but we have adopted a different test statistic that we find simpler to compute and interpret. We have checked that using instead the test statistic in Ref. [82] produces very similar results in most cases.

Bibliography

[1] Miao Li et al. "Dark Energy: A Brief Review". *Front. Phys. (Beijing)* 8 (2013), pp. 828–846. arXiv: 1209.0922 [astro-ph.CO].

[2] Edward W. Kolb and Michael S. Turner. *The Early Universe*. Vol. 69. 1990.

[3] Scott Dodelson. *Modern Cosmology*. San Diego, CA: Academic Press, 2003.

[4] H. Bethe and R. Peierls. "The "Neutrino"". *Nature* 133.3362 (Apr. 1934), pp. 532–532.

[5] Peizhi Du et al. "Sources of Low-Energy Events in Low-Threshold Dark Matter Detectors" (Nov. 2020). arXiv: 2011.13939 [hep-ph].

[6] Ahmet Coskuner et al. "Direct Detection of Bound States of Asymmetric Dark Matter". *Phys. Rev.* D100.3 (2019), p. 035025. arXiv: 1812.07573 [hep-ph].

[7] Ahmet Coskuner et al. "Directional dark matter detection in anisotropic Dirac materials". *Physical Review D* 103.1 (Jan. 2021). arXiv: 1909.09170 [hep-ph].

[8] Ahmet Coskuner et al. "Directional Detectability of Dark Matter With Single Phonon Excitations: Target Comparison" (2021). arXiv: 2102.09567 [hep-ph].

[9] F. Zwicky. "On the Masses of Nebulae and of Clusters of Nebulae". *ApJ* 86 (Oct. 1937), p. 217.

[10] Edwin Hubble and Milton L. Humason. "The Velocity-Distance Relation among Extra-Galactic Nebulae". *ApJ* 74 (July 1931), p. 43.

[11] Vera C. Rubin and Jr. Ford W. Kent. "Rotation of the Andromeda Nebula from a Spectroscopic Survey of Emission Regions". *ApJ* 159 (Feb. 1970), p. 379.

[12] M. S. Roberts and A. H. Rots. "Comparison of Rotation Curves of Different Galaxy Types". *Astronomy and Astrophysics* 26 (Aug. 1973), pp. 483–485.

[13] M. S. Roberts and R. N. Whitehurst. "The rotation curve and geometry of M31 at large galactocentric distances." *ApJ* 201 (Oct. 1975), pp. 327–346.

[14] V. C. Rubin, Jr. Ford W. K., and N. Thonnard. "Rotational properties of 21 SC galaxies with a large range of luminosities and radii, from NGC 4605 (R=4kpc) to UGC 2885 (R=122kpc)." *ApJ* 238 (June 1980), pp. 471–487.

[15] Yoshiaki Sofue and Vera Rubin. "Rotation Curves of Spiral Galaxies". *Annual Review of Astronomy and Astrophysics* 39.1 (2001), pp. 137–174. eprint: https://doi.org/10.1146/annurev.astro.39.1.137.

[16] Nitsan Bar et al. "Galactic rotation curves versus ultralight dark matter: Implications of the soliton-host halo relation". *Phys. Rev. D* 98 (8 Oct. 2018), p. 083027.

[17] Gianfranco Bertone, Dan Hooper, and Joseph Silk. "Particle dark matter: evidence, candidates and constraints". *Physics Reports* 405.5-6 (Jan. 2005), pp. 279–390.

[18] David J. Sand, Tommaso Treu, and Richard S. Ellis. "The Dark Matter Density Profile of the Lensing Cluster MS 213723: A Test of the Cold Dark Matter Paradigm". *The Astrophysical Journal* 574.2 (Aug. 2002), pp. L129–L133.

[19] Maxim Markevitch. "Chandra observation of the most interesting cluster in the universe". *ESA Spec. Publ.* 604 (2006), p. 723. arXiv: astro-ph/0511345.

[20] Douglas Clowe et al. "A Direct Empirical Proof of the Existence of Dark Matter". *The Astrophysical Journal* 648.2 (Aug. 2006), pp. L109–L113.

[21] Scott Dodelson. "The Real Problem With MOND". *International Journal of Modern Physics D* 20.14 (Dec. 2011), pp. 2749–2753.

[22] Katherine Garrett and Gintaras Duda. "Dark Matter: A Primer". *Advances in Astronomy* 2011 (2011), pp. 1–22.

[23] J.M. Overduin and P.S. Wesson. "Dark matter and background light". *Physics Reports* 402.5-6 (Nov. 2004), pp. 267–406.

[24] Timothy D. Brandt. "Constraints On Macho Dark Matter From Compact Stellar Systems In Ultra-Faint Dwarf Galaxies". *The Astrophysical Journal* 824.2 (June 2016), p. L31.

[25] Marco Battaglieri et al. "US Cosmic Visions: New Ideas in Dark Matter 2017: Community Report". *U.S. Cosmic Visions: New Ideas in Dark Matter College Park, MD, USA, March 23-25, 2017*. 2017. arXiv: 1707.04591 [hep-ph].

[26] Michael Kuhlen et al. "Dark matter direct detection with non-Maxwellian velocity structure". *Journal of Cosmology and Astroparticle Physics* 2010.02 (Feb. 2010), pp. 030–030.

[27] Jonathan L. Feng and Jason Kumar. "Dark-Matter Particles without Weak-Scale Masses or Weak Interactions". *Physical Review Letters* 101.23 (Dec. 2008).

[28] Eric D. Carlson, Marie E. Machacek, and Lawrence J. Hall. "Self-interacting dark matter". *Astrophys. J.* 398 (1992), pp. 43–52.

[29] Kathryn M. Zurek. "Asymmetric Dark Matter: Theories, signatures, and constraints". *Physics Reports* 537.3 (Apr. 2014), pp. 91–121.

[30] Marco Battaglieri et al. *US Cosmic Visions: New Ideas in Dark Matter 2017: Community Report*. 2017. arXiv: 1707.04591 [hep-ph].

[31] Jim Alexander et al. *Dark Sectors 2016 Workshop: Community Report*. 2016. arXiv: 1608.08632 [hep-ph].

[32] G. Barello, Spencer Chang, and Christopher A. Newby. "A model independent approach to inelastic dark matter scattering". *Physical Review D* 90.9 (Nov. 2014).

[33] Peizhi Du et al. *Sources of Low-Energy Events in Low-Threshold Dark Matter Detectors*. 2020. arXiv: 2011.13939 [hep-ph].

[34] Samuel K. Lee et al. "Effect of Gravitational Focusing on Annual Modulation in Dark-Matter Direct-Detection Experiments". *Physical Review Letters* 112.1 (Jan. 2014).

[35] J. I. Collar and F. T. Avignone. "Effect of elastic scattering in the Earth on cold dark matter experiments". *Phys. Rev. D* 47 (12 June 1993), pp. 5238–5246.

[36] A. Liam Fitzpatrick et al. "The effective field theory of dark matter direct detection". *Journal of Cosmology and Astroparticle Physics* 2013.02 (Feb. 2013), pp. 004–004.

[37] Gerard Jungman, Marc Kamionkowski, and Kim Griest. "Supersymmetric dark matter". *Physics Reports* 267.5-6 (Mar. 1996), pp. 195–373.

[38] Sorina Lazanu, Ionel Lazanu, and Gheorghe Ciobanu. "Modelling the transient processes produced under heavy particle irradiation". *Nuclear Instruments and Methods in Physics Research Section B: Beam Interactions with Materials and Atoms* 269.4 (Feb. 2011), pp. 498–503.

[39] Richard H. Helm. "Inelastic and Elastic Scattering of 187-Mev Electrons from Selected Even-Even Nuclei". *Phys. Rev.* 104 (1956), pp. 1466–1475.

[40] Eric Kuflik, Aaron Pierce, and Kathryn M. Zurek. "Light neutralinos with large scattering cross sections in the minimal supersymmetric standard model". *Physical Review D* 81.11 (June 2010).

[41] Stephen P. Martin. "A Supersymmetry Primer". *Advanced Series on Directions in High Energy Physics* (July 1998), pp. 1–98.

[42] G. B. Gelmini, P. Gondolo, and E. Roulet. "Neutralino Dark Matter Searches". *Nucl. Phys. B* 351 (1991), pp. 623–644.

[43] Yonit Hochberg et al. "Directional detection of dark matter with two-dimensional targets". *Physics Letters B* 772 (Sept. 2017), pp. 239–246.

[44] Tanner Trickle et al. "Multi-channel direct detection of light dark matter: theoretical framework". *Journal of High Energy Physics* 2020.3 (Mar. 2020).

[45] R. Matthias Geilhufe, Felix Kahlhoefer, and Martin Wolfgang Winkler. "Dirac materials for sub-MeV dark matter detection: New targets and improved formalism". *Physical Review D* 101.5 (Mar. 2020).

[46] R. D. Peccei and Helen R. Quinn. "CP Conservation in the Presence of Pseudoparticles". *Phys. Rev. Lett.* 38 (25 June 1977), pp. 1440–1443.

[47] R. D. Peccei and Helen R. Quinn. "Constraints imposed by CP conservation in the presence of pseudoparticles". *Phys. Rev. D* 16 (6 Sept. 1977), pp. 1791–1797.

[48] Steven Weinberg. "A New Light Boson?" *Phys. Rev. Lett.* 40 (4 Jan. 1978), pp. 223–226.

[49] A. Boyarsky et al. "Sterile neutrino Dark Matter". *Progress in Particle and Nuclear Physics* 104 (Jan. 2019), pp. 1–45.

[50] J. L. Feng et al. "Planning the Future of U.S. Particle Physics (Snowmass 2013): Chapter 4: Cosmic Frontier". *Community Summer Study 2013: Snowmass on the Mississippi*. Jan. 2014. arXiv: 1401.6085 [hep-ex].

[51] Moira I. Gresham, Hou Keong Lou, and Kathryn M. Zurek. "Early Universe synthesis of asymmetric dark matter nuggets". *Physical Review D* 97.3 (Feb. 2018).

[52] Moira I. Gresham, Hou Keong Lou, and Kathryn M. Zurek. "Nuclear structure of bound states of asymmetric dark matter". *Physical Review D* 96.9 (Nov. 2017).

[53] Mark B. Wise and Yue Zhang. "Stable bound states of asymmetric dark matter". *Physical Review D* 90.5 (Sept. 2014).

[54] Jim Alexander et al. "Dark Sectors 2016 Workshop: Community Report". 2016. arXiv: 1608.08632 [hep-ph].

[55] C. Boehm and Pierre Fayet. "Scalar dark matter candidates". *Nucl. Phys. B* 683 (2004), pp. 219–263. arXiv: hep-ph/0305261.

[56] Matthew J. Strassler and Kathryn M. Zurek. "Echoes of a hidden valley at hadron colliders". *Phys. Lett. B* 651 (2007), pp. 374–379. arXiv: hep-ph/0604261.

[57] Maxim Pospelov and Adam Ritz. "Astrophysical Signatures of Secluded Dark Matter". *Phys. Lett.* B671 (2009), pp. 391–397. arXiv: 0810.1502 [hep-ph].

[58] Jonathan L. Feng and Jason Kumar. "The WIMPless Miracle: Dark-Matter Particles without Weak-Scale Masses or Weak Interactions". *Phys. Rev. Lett.* 101 (2008), p. 231301. arXiv: 0803.4196 [hep-ph].

[59] Kathryn M. Zurek. "Asymmetric Dark Matter: Theories, Signatures, and Constraints". *Phys. Rept.* 537 (2014), pp. 91–121. arXiv: 1308.0338 [hep-ph].

[60] Yonit Hochberg et al. "Mechanism for Thermal Relic Dark Matter of Strongly Interacting Massive Particles". *Phys. Rev. Lett.* 113 (2014), p. 171301. arXiv: 1402.5143 [hep-ph].

[61] David E. Kaplan, Markus A. Luty, and Kathryn M. Zurek. "Asymmetric Dark Matter". *Phys. Rev.* D79 (2009), p. 115016. arXiv: 0901.4117 [hep-ph].

[62] Tongyan Lin, Hai-Bo Yu, and Kathryn M. Zurek. "On Symmetric and Asymmetric Light Dark Matter". *Phys. Rev.* D85 (2012), p. 063503. arXiv: 1111.0293 [hep-ph].

[63] Mark B. Wise and Yue Zhang. "Yukawa Bound States of a Large Number of Fermions". *JHEP* 02 (2015). [Erratum: JHEP10,165(2015)], p. 023. arXiv: 1411.1772 [hep-ph].

[64] Mark B. Wise and Yue Zhang. "Stable Bound States of Asymmetric Dark Matter". *Phys. Rev.* D90.5 (2014). [Erratum: Phys. Rev.D91,no.3,039907(2015)], p. 055030. arXiv: 1407.4121 [hep-ph].

[65] Gordan Krnjaic and Kris Sigurdson. "Big Bang Darkleosynthesis". *Phys. Lett.* B751 (2015), pp. 464–468. arXiv: 1406.1171 [hep-ph].

[66] Edward Hardy et al. "Big Bang Synthesis of Nuclear Dark Matter". *JHEP* 06 (2015), p. 011. arXiv: 1411.3739 [hep-ph].

[67] William Detmold, Matthew McCullough, and Andrew Pochinsky. "Dark Nuclei I: Cosmology and Indirect Detection". *Phys. Rev.* D90.11 (2014), p. 115013. arXiv: 1406.2276 [hep-ph].

[68] Moira I. Gresham, Hou Keong Lou, and Kathryn M. Zurek. "Nuclear Structure of Bound States of Asymmetric Dark Matter". *Phys. Rev.* D96.9 (2017), p. 096012. arXiv: 1707.02313 [hep-ph].

[69] Moira I. Gresham, Hou Keong Lou, and Kathryn M. Zurek. "Early Universe synthesis of asymmetric dark matter nuggets". *Phys. Rev.* D97.3 (2018), p. 036003. arXiv: 1707.02316 [hep-ph].

[70] Edward Witten. "Cosmic Separation of Phases". *Phys. Rev.* D30 (1984), pp. 272–285.

[71] Yang Bai, Andrew J. Long, and Sida Lu. "Dark Quark Nuggets" (2018). arXiv: 1810.04360 [hep-ph].

[72] Moira I. Gresham, Hou Keong Lou, and Kathryn M. Zurek. "Astrophysical Signatures of Asymmetric Dark Matter Bound States" (2018). arXiv: 1805.04512 [hep-ph].

[73] Edward Hardy et al. "Signatures of Large Composite Dark Matter States". *JHEP* 07 (2015), p. 133. arXiv: 1504.05419 [hep-ph].

[74] A. Butcher et al. "Can Tonne-Scale Direct Detection Experiments Discover Nuclear Dark Matter?" *JCAP* 1710.10 (2017), p. 035. arXiv: 1610.01840 [hep-ph].

[75] Dorota M. Grabowska, Tom Melia, and Surjeet Rajendran. "Detecting Dark Blobs". *Phys. Rev.* D98.11 (2018), p. 115020. arXiv: 1807.03788 [hep-ph].

[76] Rouven Essig et al. "Detection of sub-GeV Dark Matter and Solar Neutrinos via Chemical-Bond Breaking". *Phys. Rev.* D95.5 (2017), p. 056011. arXiv: 1608.02940 [hep-ph].

[77] Fedja Kadribasic et al. "Directional Sensitivity In Light-Mass Dark Matter Searches With Single-Electron Resolution Ionization Detectors". *Phys. Rev. Lett.* 120.11 (2018), p. 111301. arXiv: 1703.05371 [physics.ins-det].

[78] Ranny Budnik et al. "Direct Detection of Light Dark Matter and Solar Neutrinos via Color Center Production in Crystals". *Phys. Lett.* B782 (2018), pp. 242–250. arXiv: 1705.03016 [hep-ph].

[79] Katelin Schutz and Kathryn M. Zurek. "Detectability of Light Dark Matter with Superfluid Helium". *Phys. Rev. Lett.* 117.12 (2016), p. 121302. arXiv: 1604.08206 [hep-ph].

[80] Simon Knapen, Tongyan Lin, and Kathryn M. Zurek. "Light Dark Matter in Superfluid Helium: Detection with Multi-excitation Production". *Phys. Rev.* D95.5 (2017), p. 056019. arXiv: 1611.06228 [hep-ph].

[81] Simon Knapen et al. "Detection of Light Dark Matter With Optical Phonons in Polar Materials". *Phys. Lett.* B785 (2018), pp. 386–390. arXiv: 1712.06598 [hep-ph].

[82] Sinead Griffin et al. "Directional Detection of Light Dark Matter with Polar Materials". *Phys. Rev.* D98.11 (2018), p. 115034. arXiv: 1807.10291 [hep-ph].

[83] Rouven Essig, Jeremy Mardon, and Tomer Volansky. "Direct Detection of Sub-GeV Dark Matter". *Phys.Rev. D85 (2012) 076007* D85 (Aug. 26, 2011), p. 076007. arXiv: 1108.5383 [hep-ph].

[84] Rouven Essig et al. "Direct Detection of sub-GeV Dark Matter with Semiconductor Targets". *JHEP* 05 (2016), p. 046. arXiv: 1509.01598 [hep-ph].

[85] Yonit Hochberg et al. "Directional detection of dark matter with two-dimensional targets". *Phys. Lett.* B772 (2017), pp. 239–246. arXiv: 1606.08849 [hep-ph].

[86] Stephen Derenzo et al. "Direct Detection of sub-GeV Dark Matter with Scintillating Targets". *Phys. Rev.* D96.1 (2017), p. 016026. arXiv: 1607.01009 [hep-ph].

[87] Yonit Hochberg, Yue Zhao, and Kathryn M. Zurek. "Superconducting Detectors for Superlight Dark Matter". *Phys. Rev. Lett.* 116.1 (2016), p. 011301. arXiv: 1504.07237 [hep-ph].

[88] Yonit Hochberg et al. "Detection of sub-MeV Dark Matter with Three-Dimensional Dirac Materials". *Phys. Rev.* D97.1 (2018), p. 015004. arXiv: 1708.08929 [hep-ph].

[89] John F. Gunion et al. "The Higgs Hunter's Guide". *Front. Phys.* 80 (2000), pp. 1–404.

[90] Morad Aaboud et al. "Search for dark matter and other new phenomena in events with an energetic jet and large missing transverse momentum using the ATLAS detector". *JHEP* 01 (2018), p. 126. arXiv: 1711.03301 [hep-ex].

[91] Albert M Sirunyan et al. "Search for Low Mass Vector Resonances Decaying to Quark-Antiquark Pairs in Proton-Proton Collisions at $\sqrt{s} = 13$ TeV". *Phys. Rev. Lett.* 119.11 (2017), p. 111802. arXiv: 1705.10532 [hep-ex].

[92] Yu-Sheng Liu, David McKeen, and Gerald A. Miller. "Electrophobic Scalar Boson and Muonic Puzzles". *Phys. Rev. Lett.* 117.10 (2016), p. 101801. arXiv: 1605.04612 [hep-ph].

[93] J. P. Lees et al. "Search for a Dark Photon in e^+e^- Collisions at BaBar". *Phys. Rev. Lett.* 113.20 (2014), p. 201801. arXiv: 1406.2980 [hep-ex].

[94] Rouven Essig et al. "Constraining Light Dark Matter with Low-Energy e^+e^- Colliders". *JHEP* 11 (2013), p. 167. arXiv: 1309.5084 [hep-ph].

[95] E. Kou et al. "The Belle II Physics Book" (2018). arXiv: 1808.10567 [hep-ex].

[96] Patrick deNiverville, Maxim Pospelov, and Adam Ritz. "Observing a light dark matter beam with neutrino experiments". *Phys. Rev.* D84 (2011), p. 075020. arXiv: 1107.4580 [hep-ph].

[97] Simon Knapen, Tongyan Lin, and Kathryn M. Zurek. "Light Dark Matter: Models and Constraints". *Phys. Rev.* D96.11 (2017), p. 115021. arXiv: 1709.07882 [hep-ph].

[98] Edward Hardy and Robert Lasenby. "Stellar cooling bounds on new light particles: plasma mixing effects". *JHEP* 02 (2017), p. 033. arXiv: 1611.05852 [hep-ph].

[99] Haipeng An, Maxim Pospelov, and Josef Pradler. "New stellar constraints on dark photons". *Phys. Lett.* B725 (2013), pp. 190–195. arXiv: 1302.3884 [hep-ph].

[100] David N. Spergel and Paul J. Steinhardt. "Observational evidence for selfinteracting cold dark matter". *Phys. Rev. Lett.* 84 (2000), pp. 3760–3763. arXiv: astro-ph/9909386 [astro-ph].

[101] Felix Kahlhoefer et al. "Colliding clusters and dark matter self-interactions". *Mon. Not. Roy. Astron. Soc.* 437.3 (2014), pp. 2865–2881. arXiv: 1308.3419 [astro-ph.CO].

[102] Jonathan L. Feng et al. "Hidden Charged Dark Matter". *JCAP* 0907 (2009), p. 004. arXiv: 0905.3039 [hep-ph].

[103] Samuel D. McDermott, Hai-Bo Yu, and Kathryn M. Zurek. "Turning off the Lights: How Dark is Dark Matter?" *Phys. Rev.* D83 (2011), p. 063509. arXiv: 1011.2907 [hep-ph].

[104] E. Aprile et al. "Dark Matter Search Results from a One Ton-Year Exposure of XENON1T". *Phys. Rev. Lett.* 121.11 (2018), p. 111302. arXiv: 1805.12562 [astro-ph.CO].

[105] R. Agnese et al. "Low-mass dark matter search with CDMSlite". *Phys. Rev. D* 97.2 (2018), p. 022002. arXiv: 1707.01632 [astro-ph.CO].

[106] Chris Kouvaris and Josef Pradler. "Probing sub-GeV Dark Matter with conventional detectors". *Phys. Rev. Lett.* 118.3 (2017), p. 031803. arXiv: 1607.01789 [hep-ph].

[107] Masahiro Ibe et al. "Migdal Effect in Dark Matter Direct Detection Experiments". *JHEP* 03 (2018), p. 194. arXiv: 1707.07258 [hep-ph].

[108] D. S. Akerib et al. "Results of a Search for Sub-GeV Dark Matter Using 2013 LUX Data". *Phys. Rev. Lett.* 122.13 (2019), p. 131301. arXiv: 1811.11241 [astro-ph.CO].

[109] Xiangyi Cui et al. "Dark Matter Results From 54-Ton-Day Exposure of PandaX-II Experiment" (2017). arXiv: 1708.06917 [astro-ph.CO].

[110] D. S. Akerib et al. "Results from a search for dark matter in the complete LUX exposure". *Phys. Rev. Lett.* 118.2 (2017), p. 021303. arXiv: 1608.07648 [astro-ph.CO].

[111] E. Aprile et al. "First Dark Matter Search Results from the XENON1T Experiment" (2017). arXiv: 1705.06655 [astro-ph.CO].

[112] G. Angloher et al. "Results on light dark matter particles with a low-threshold CRESST-II detector". *Eur. Phys. J. C* 76.1 (2016), p. 25. arXiv: 1509.01515 [astro-ph.CO].

[113] Q. Arnaud et al. "First results from the NEWS-G direct dark matter search experiment at the LSM" (2017). arXiv: 1706.04934 [astro-ph.IM].

[114] D. S. Akerib et al. "Projected WIMP Sensitivity of the LUX-ZEPLIN (LZ) Dark Matter Experiment" (2018). arXiv: 1802.06039 [astro-ph.IM].

[115] R. Agnese et al. "Projected Sensitivity of the SuperCDMS SNOLAB experiment". *Phys. Rev.* D95.8 (2017), p. 082002. arXiv: 1610.00006 [physics.ins-det].

[116] Wei Guo and Daniel N. McKinsey. "Concept for a dark matter detector using liquid helium-4". *Phys. Rev.* D87.11 (2013), p. 115001. arXiv: 1302.0534 [astro-ph.IM].

[117] S. A. Hertel et al. "A Path to the Direct Detection of sub-GeV Dark Matter Using Calorimetric Readout of a Superfluid ^{4}He Target" (2018). arXiv: 1810.06283 [physics.ins-det].

[118] Yonit Hochberg et al. "Detecting Superlight Dark Matter with Fermi-Degenerate Materials". *JHEP* 08 (2016), p. 057. arXiv: 1512.04533 [hep-ph].

[119] Philip C. Bunting et al. "Magnetic Bubble Chambers and Sub-GeV Dark Matter Direct Detection". *Phys. Rev.* D95.9 (2017), p. 095001. arXiv: 1701.06566 [hep-ph].

[120] Rouven Essig et al. *Detecting Dark Matter-Nucleus Scattering through Molecular Excitations*. Talk at New Probes for Physics Beyond the Standard Model, KITP 2018. 2018.

[121] C. E. Campbell, E. Krotscheck, and T. Lichtenegger. "Dynamic many-body theory: Multiparticle fluctuations and the dynamic structure of ^{4}He". 91.18, 184510 (May 2015), p. 184510.

[122] Joseph Bramante et al. "Saturated Overburden Scattering and the Multiscatter Frontier: Discovering Dark Matter at the Planck Mass and Beyond" (2018). arXiv: 1803.08044 [hep-ph].

[123] Rouven Essig et al. "First Direct Detection Limits on sub-GeV Dark Matter from XENON10". *Phys. Rev. Lett.* 109 (2012), p. 021301. arXiv: 1206.2644 [astro-ph.CO].

[124] Rouven Essig, Tomer Volansky, and Tien-Tien Yu. "New Constraints and Prospects for sub-GeV Dark Matter Scattering off Electrons in Xenon". *Phys. Rev.* D96.4 (2017), p. 043017. arXiv: 1703.00910 [hep-ph].

[125] J. Angle et al. "A search for light dark matter in XENON10 data". *Phys. Rev. Lett.* 107 (2011). [Erratum: Phys. Rev. Lett.110,249901(2013)], p. 051301. arXiv: 1104.3088 [astro-ph.CO].

[126] Michael Crisler et al. "SENSEI: First Direct-Detection Constraints on sub-GeV Dark Matter from a Surface Run". *Phys. Rev. Lett.* 121.6 (2018), p. 061803. arXiv: 1804.00088 [hep-ex].

[127] R. Agnese et al. "First Dark Matter Constraints from a SuperCDMS Single-Charge Sensitive Detector". *Phys. Rev. Lett.* 121.5 (2018). [Erratum: Phys.Rev.Lett. 122, 069901 (2019)], p. 051301. arXiv: 1804.10697 [hep-ex].

[128] Mariangela Settimo. "The DAMIC experiment at SNOLAB". *53rd Rencontres de Moriond on QCD and High Energy Interactions (Moriond QCD 2018) La Thuile, Italy, March 17-24, 2018*. 2018. arXiv: 1805.10001 [astro-ph.IM].

[129] E. Baracchini et al. "PTOLEMY: A Proposal for Thermal Relic Detection of Massive Neutrinos and Directional Detection of MeV Dark Matter" (2018). arXiv: 1808.01892 [physics.ins-det].

[130] Samuel K. Lee et al. "Modulation Effects in Dark Matter-Electron Scattering Experiments". *Phys. Rev.* D92.8 (2015), p. 083517. arXiv: 1508.07361 [hep-ph].

[131] Paolo Giannozzi et al. "QUANTUM ESPRESSO: a modular and open-source software project for quantum simulations of materials". *Journal of Physics: Condensed Matter* 21.39 (2009), p. 395502.

[132] David Dunsky, Lawrence J. Hall, and Keisuke Harigaya. "CHAMP Cosmic Rays" (2018). arXiv: 1812.11116 [astro-ph.HE].

[133] Maxim Pospelov, Adam Ritz, and Mikhail B. Voloshin. "Secluded WIMP Dark Matter". *Phys. Lett.* B662 (2008), pp. 53–61. arXiv: 0711.4866 [hep-ph].

[134] Dan Hooper and Kathryn M. Zurek. "A Natural Supersymmetric Model with MeV Dark Matter". *Phys. Rev.* D77 (2008), p. 087302. arXiv: 0801.3686 [hep-ph].

[135] Jason Kumar and Jonathan L. Feng. "WIMPless Dark Matter". *AIP Conf. Proc.* 1200.1 (2010), pp. 1059–1062. arXiv: 0909.2877 [hep-ph].

[136] Timothy Cohen et al. "Asymmetric Dark Matter from a GeV Hidden Sector". *Phys. Rev.* D82 (2010), p. 056001. arXiv: 1005.1655 [hep-ph].

[137] Nima Arkani-Hamed and Neal Weiner. "LHC Signals for a SuperUnified Theory of Dark Matter". *JHEP* 12 (2008), p. 104. arXiv: 0810.0714 [hep-ph].

[138] Clifford Cheung et al. "Kinetic Mixing as the Origin of Light Dark Scales". *Phys. Rev.* D80 (2009), p. 035008. arXiv: 0902.3246 [hep-ph].

[139] David E. Morrissey, David Poland, and Kathryn M. Zurek. "Abelian Hidden Sectors at a GeV". *JHEP* 07 (2009), p. 050. arXiv: 0904.2567 [hep-ph].

[140] Lawrence J. Hall et al. "Freeze-In Production of FIMP Dark Matter". *JHEP* 03 (2010), p. 080. arXiv: 0911.1120 [hep-ph].

[141] Xiaoyong Chu, Thomas Hambye, and Michel H. G. Tytgat. "The Four Basic Ways of Creating Dark Matter Through a Portal". *JCAP* 1205 (2012), p. 034. arXiv: 1112.0493 [hep-ph].

[142] Cora Dvorkin, Tongyan Lin, and Katelin Schutz. "Making dark matter out of light: freeze-in from plasma effects". *Phys. Rev.* D99.11 (2019), p. 115009. arXiv: 1902.08623 [hep-ph].

[143] Peter W. Graham et al. "Semiconductor Probes of Light Dark Matter". *Phys. Dark Univ.* 1 (2012), pp. 32–49. arXiv: 1203.2531 [hep-ph].

[144] Javier Tiffenberg et al. "Single-electron and single-photon sensitivity with a silicon Skipper CCD". *Phys. Rev. Lett.* 119.13 (2017), p. 131802. arXiv: 1706.00028 [physics.ins-det].

[145] Orr Abramoff et al. "SENSEI: Direct-Detection Constraints on Sub-GeV Dark Matter from a Shallow Underground Run Using a Prototype Skipper-CCD". *Phys. Rev. Lett.* 122.16 (2019), p. 161801. arXiv: 1901.10478 [hep-ex].

[146] A. Aguilar-Arevalo et al. "Search for low-mass WIMPs in a 0.6 kg day exposure of the DAMIC experiment at SNOLAB". *Phys. Rev.* D94.8 (2016), p. 082006. arXiv: 1607.07410 [astro-ph.CO].

[147] A. Aguilar-Arevalo et al. "Constraints on Light Dark Matter Particles Interacting with Electrons from DAMIC at SNOLAB". *Phys. Rev. Lett.* 123.18 (2019), p. 181802. arXiv: 1907.12628 [astro-ph.CO].

[148] R. Agnese et al. "Search for Low-Mass Weakly Interacting Massive Particles with SuperCDMS". *Phys. Rev. Lett.* 112.24 (2014), p. 241302. arXiv: 1402.7137 [hep-ex].

[149] R. Agnese et al. "New Results from the Search for Low-Mass Weakly Interacting Massive Particles with the CDMS Low Ionization Threshold Experiment". *Phys. Rev. Lett. 116, 071301 (2016)* 116.7 (Sept. 8, 2015), p. 071301. arXiv: 1509.02448 [astro-ph.CO].

[150] R. K. Romani et al. "Thermal detection of single e-h pairs in a biased silicon crystal detector". *Appl. Phys. Lett.* 112.4 (2018), p. 043501. arXiv: 1710.09335 [physics.ins-det].

[151] R. Agnese et al. "Search for Low-Mass Dark Matter with CDMSlite Using a Profile Likelihood Fit". *Phys. Rev. D* 99.6 (2019), p. 062001. arXiv: 1808.09098 [astro-ph.CO].

[152] R. Matthias Geilhufe, Felix Kahlhoefer, and Martin Wolfgang Winkler. "Dirac Materials for Sub-MeV Dark Matter Detection: New Targets and Improved Formalism" (2019). arXiv: 1910.02091 [hep-ph].

[153] Surjeet Rajendran et al. "A method for directional detection of dark matter using spectroscopy of crystal defects". *Phys. Rev.* D96.3 (2017), p. 035009. arXiv: 1705.09760 [hep-ph].

[154] Fedja Kadribasic et al. "Directional Sensitivity in Light-Mass Dark Matter Searches with Single-Electron-Resolution Ionization Detectors". *Phys. Rev. Lett.* 120 (11 Mar. 2018), p. 111301.

[155] Daniel Feldman, Zuowei Liu, and Pran Nath. "The Stueckelberg Z-prime Extension with Kinetic Mixing and Milli-Charged Dark Matter From the Hidden Sector". *Phys. Rev. D* 75 (2007), p. 115001. arXiv: hep-ph/0702123.

[156] Haipeng An, Maxim Pospelov, and Josef Pradler. "Dark Matter Detectors as Dark Photon Helioscopes". *Phys. Rev. Lett.* 111 (2013), p. 041302. arXiv: 1304.3461 [hep-ph].

[157] Fangdong Tang et al. "Three-dimensional quantum Hall effect and metal–insulator transition in ZrTe5". *Nature* 569.7757 (May 2019), pp. 537–541.

[158] Yonit Hochberg, Tongyan Lin, and Kathryn M. Zurek. "Absorption of light dark matter in semiconductors". *Phys. Rev.* D95.2 (2017), p. 023013. arXiv: 1608.01994 [hep-ph].

[159] Haipeng An et al. "Direct Detection Constraints on Dark Photon Dark Matter". *Phys. Lett.* B747 (2015), pp. 331–338. arXiv: 1412.8378 [hep-ph].

[160] Haipeng An, Maxim Pospelov, and Josef Pradler. "Dark Matter Detectors as Dark Photon Helioscopes". *Phys. Rev. Lett.* 111 (2013), p. 041302. arXiv: 1304.3461 [hep-ph].

[161] Sacha Davidson, Steen Hannestad, and Georg Raffelt. "Updated bounds on millicharged particles". *JHEP* 05 (2000), p. 003. arXiv: hep-ph/0001179 [hep-ph].

[162] Jonathan L. Feng, Manoj Kaplinghat, and Hai-Bo Yu. "Halo Shape and Relic Density Exclusions of Sommerfeld-Enhanced Dark Matter Explanations of Cosmic Ray Excesses". *Phys. Rev. Lett.* 104 (2010), p. 151301. arXiv: 0911.0422 [hep-ph].

[163] Yonit Hochberg, Tongyan Lin, and Kathryn M. Zurek. "Detecting Ultralight Bosonic Dark Matter via Absorption in Superconductors". *Phys. Rev.* D94.1 (2016), p. 015019. arXiv: 1604.06800 [hep-ph].

[164] J. Amaré et al. "ANAIS-112 status: two years results on annual modulation". *J. Phys. Conf. Ser.* 1468.1 (2020). Ed. by Masayuki Nakahata, p. 012014. arXiv: 1910.13365 [astro-ph.IM].

[165] F. Pröbst et al. "Results of CRESST Phase I". *Nucl. Phys. Proc. Suppl.* 110 (2002), pp. 67–69.

[166] G. Angloher et al. "Limits on Dark Matter Effective Field Theory Parameters with CRESST-II". *Eur. Phys. J. C* 79.1 (2019), p. 43. arXiv: 1809.03753 [hep-ph].

[167] H. Kluck et al. "Latest results of CRESST-III's search for sub-GeV/c^2 dark matter". *J. Phys. Conf. Ser.* 1468.1 (2020). Ed. by Masayuki Nakahata, p. 012038.

[168] R. Bernabei et al. "The DAMA project: Achievements, implications and perspectives". *Prog. Part. Nucl. Phys.* 114 (2020), p. 103810.

[169] A. Aguilar-Arevalo et al. "Results on low-mass weakly interacting massive particles from a 11 kg-day target exposure of DAMIC at SNOLAB". *Phys. Rev. Lett.* 125 (2020), p. 241803. arXiv: 2007.15622 [astro-ph.CO].

[170] P. Agnes et al. "Low-Mass Dark Matter Search with the DarkSide-50 Experiment". *Phys. Rev. Lett.* 121.8 (2018), p. 081307. arXiv: 1802.06994 [astro-ph.HE].

[171] Jay Hyun Jo. "Results from the DM-Ice17 Dark Matter Experiment at the South Pole". *PoS* ICHEP2016 (2017), p. 1223. arXiv: 1612.07426 [physics.ins-det].

[172] Kyungwon Kim. "Status of the KIMS-NaI experiment". *Proceedings, Meeting of the APS Division of Particles and Fields (DPF 2015): Ann Arbor, Michigan, USA, 4-8 Aug 2015*. 2015. arXiv: 1511.00023 [physics.ins-det].

[173] D. S. Akerib et al. "Extending light WIMP searches to single scintillation photons in LUX". *Phys. Rev. D* 101.4 (2020), p. 042001. arXiv: 1907.06272 [astro-ph.CO].

[174] D. S. Akerib et al. "An Effective Field Theory Analysis of the First LUX Dark Matter Search" (Mar. 2020). arXiv: 2003.11141 [astro-ph.CO].

[175] M. Antonello et al. "The SABRE project and the SABRE Proof-of-Principle". *Eur. Phys. J. C* 79.4 (2019), p. 363. arXiv: 1806.09340 [physics.ins-det].

[176] I. Alkhatib et al. "Light Dark Matter Search with a High-Resolution Athermal Phonon Detector Operated Above Ground" (July 2020). arXiv: 2007.14289 [hep-ex].

[177] E. Aprile et al. "Light Dark Matter Search with Ionization Signals in XENON1T". *Phys. Rev. Lett.* 123.25 (2019), p. 251801. arXiv: 1907.11485 [hep-ex].

[178] Nicolás Bernal et al. "The Dawn of FIMP Dark Matter: A Review of Models and Constraints". *Int. J. Mod. Phys. A* 32.27 (2017), p. 1730023. arXiv: 1706.07442 [hep-ph].

[179] Kalliopi Petraki and Raymond R. Volkas. "Review of asymmetric dark matter". *Int. J. Mod. Phys. A* 28 (2013), p. 1330028. arXiv: 1305.4939 [hep-ph].

[180] Yonit Hochberg et al. "Model for Thermal Relic Dark Matter of Strongly Interacting Massive Particles". *Phys. Rev. Lett.* 115.2 (2015), p. 021301. arXiv: 1411.3727 [hep-ph].

[181] Noah Alexander Kurinsky et al. "Diamond Detectors for Direct Detection of Sub-GeV Dark Matter". *Phys. Rev.* D99.12 (2019), p. 123005. arXiv: 1901.07569 [hep-ex].

[182] Carlos Blanco et al. "Dark Matter-Electron Scattering from Aromatic Organic Targets". *Phys. Rev. D* 101.5 (2020), p. 056001. arXiv: 1912.02822 [hep-ph].

[183] Riccardo Catena et al. "Atomic responses to general dark matter-electron interactions". *Phys. Rev. Res.* 2.3 (2020), p. 033195. arXiv: 1912.08204 [hep-ph].

[184] Mariangela Settimo. "Search for low-mass dark matter with the DAMIC experiment". *16th Rencontres du Vietnam: Theory meeting experiment: Particle Astrophysics and Cosmology*. Apr. 2020. arXiv: 2003.09497 [hep-ex].

[185] Liron Barak et al. "SENSEI: Direct-Detection Results on sub-GeV Dark Matter from a New Skipper-CCD". *Phys. Rev. Lett.* 125.17 (2020), p. 171802. arXiv: 2004.11378 [astro-ph.CO].

[186] D. W. Amaral et al. "Constraints on low-mass, relic dark matter candidates from a surface-operated SuperCDMS single-charge sensitive detector". *Phys. Rev. D* 102.9 (2020), p. 091101. arXiv: 2005.14067 [hep-ex].

[187] Francesca Acanfora, Angelo Esposito, and Antonio D. Polosa. "Sub-GeV Dark Matter in Superfluid He-4: an Effective Theory Approach". *Eur. Phys. J.* C79.7 (2019), p. 549. arXiv: 1902.02361 [hep-ph].

[188] Andrea Caputo, Angelo Esposito, and Antonio D. Polosa. "Sub-MeV Dark Matter and the Goldstone Modes of Superfluid Helium". *Phys. Rev. D* 100.11 (2019), p. 116007. arXiv: 1907.10635 [hep-ph].

[189] Gordon Baym et al. "Searching for low mass dark matter via phonon creation in superfluid 4He". *Phys. Rev. D* 102.3 (2020), p. 035014. arXiv: 2005.08824 [hep-ph].

[190] Andrea Caputo et al. "Directional detection of light dark matter from three-phonon events in superfluid ^{4}He" (Dec. 2020). arXiv: 2012.01432 [hep-ph].

[191] Tanner Trickle et al. "Multi-Channel Direct Detection of Light Dark Matter: Theoretical Framework". *JHEP* 03 (2020), p. 036. arXiv: 1910.08092 [hep-ph].

[192] Sinéad M. Griffin et al. "Multichannel direct detection of light dark matter: Target comparison". *Phys. Rev. D* 101.5 (2020), p. 055004. arXiv: 1910.10716 [hep-ph].

[193] Brian Campbell-Deem et al. "Multiphonon excitations from dark matter scattering in crystals". *Phys. Rev. D* 101.3 (2020). [Erratum: Phys.Rev.D 102, 019904 (2020)], p. 036006. arXiv: 1911.03482 [hep-ph].

[194] Sinéad M. Griffin et al. "SiC Detectors for Sub-GeV Dark Matter" (Aug. 2020). arXiv: 2008.08560 [hep-ph].

[195] Tanner Trickle, Zhengkang Zhang, and Kathryn M. Zurek. "Effective Field Theory of Dark Matter Direct Detection With Collective Excitations" (Sept. 2020). arXiv: 2009.13534 [hep-ph].

[196] Yonatan Kahn, Gordan Krnjaic, and Bashi Mandava. "Dark Matter Detection With Bound Nuclear Targets: The Poisson Phonon Tail" (Nov. 2020). arXiv: 2011.09477 [hep-ph].

[197] Simon Knapen, Jonathan Kozaczuk, and Tongyan Lin. "The Migdal effect in semiconductors" (Nov. 2020). arXiv: 2011.09496 [hep-ph].

[198] Matt Pyle, Enectali Feliciano-Figueroa, and Bernard Sadoulet. "Optimized Designs for Very Low Temperature Massive Calorimeters" (Mar. 2015). arXiv: 1503.01200 [astro-ph.IM].

[199] Humphrey J. Maris, George M. Seidel, and Derek Stein. "Dark Matter Detection Using Helium Evaporation and Field Ionization". *Phys. Rev. Lett.* 119.18 (2017), p. 181303. arXiv: 1706.00117 [astro-ph.IM].

[200] J. Rothe et al. "TES-Based Light Detectors for the CRESST Direct Dark Matter Search". *J. Low Temp. Phys.* 193.5-6 (2018), pp. 1160–1166.

[201] I. Colantoni et al. "BULLKID: BULky and Low-Threshold Kinetic Inductance Detectors". *J. Low Temp. Phys.* 199.3-4 (2020), pp. 593–597.

[202] C.W. Fink et al. "Characterizing TES Power Noise for Future Single Optical-Phonon and Infrared-Photon Detectors". *AIP Adv.* 10.8 (2020), p. 085221. arXiv: 2004.10257 [physics.ins-det].

[203] C. Chang et al. "Snowmass 2021 Letter of Interest: The TESSARACT Dark Matter Project". 2020.

[204] A. K. Drukier, Katherine Freese, and D. N. Spergel. "Detecting Cold Dark Matter Candidates". *Phys. Rev. D* 33 (1986), pp. 3495–3508.

[205] https://github.com/tanner-trickle/dm-phonon-scatter.

[206] https://demo-phonon-web-app.herokuapp.com.

[207] Atsushi Togo. *Phonon Database at Kyoto University*. http://phonondb.mtl.kyoto-u.ac.jp.

[208] Atsushi Togo and Isao Tanaka. "First principles phonon calculations in materials science". *Scripta Materialia* 108 (Nov. 2015), pp. 1–5.

[209] J. Lindhard and M. Scharff. "Energy Dissipation by Ions in the kev Region". *Phys. Rev.* 124 (1961), pp. 128–130.

[210] David J. Land and James G. Brennan. "Electronic stopping power of low-velocity ions: Ions: C-Xe Targets: H-Xe". *Atomic Data and Nuclear Data Tables* 22.3 (1978), pp. 235–247.

[211] J. Lindhard. "On the properties of a gas of charged particles". *Matematisk-fysiske Meddeleser* 28.8 (1954).

[212] Sanjay Reddy, Madappa Prakash, and James M Lattimer. "Neutrino interactions in hot and dense matter". *Phys. Rev.* D58 (1998), p. 013009. arXiv: astro-ph/9710115 [astro-ph].

[213] J.R. Schrieffer. *Theory Of Superconductivity*. Advanced Books Classics. Avalon Publishing, 1999.

[214] M. Gajdo š et al. "Linear optical properties in the projector-augmented wave methodology". *Phys. Rev. B* 73 (4 Jan. 2006), p. 045112.